The Effects of Current and Rotation on Tokamak Edge Plasma Stability

Xinliang Xu

A thesis presented for the degree of
Doctor of Philosophy

York Plasma Institute
Department of Physics

November 2018

Abstract

Edge Localized Modes (ELMs) are repetitive eruptions of particles and energy which occur in many high confinement mode plasmas. The mitigation of ELMs is one of the important topics in achieving high performance operating mode in tokamak devices. However, the physical mechanism by which mitigation and suppression is achieved is still not well understood. In the theories of ELMs, the plasma current and flow shear (include Zonal flow, shear flow and rotation) have been suggested to have significant influence on ELMs.

In this thesis, the possibility of influencing ELMs by radio wave (ECRH) means is investigated, by studying the underlying flow generation mechanisms, and the influence of flows, toroidal rotation and edge current on ELMs. The kink-ballooning mode is addressed, which can drive ELMs in some peeling-ballooning stable regions in our analytic and numerical work . Then novel 2-fluid cold-ion equations are developed from the collisional Vlasov equation in a non-inertial rotating frame for the first time. Implementing these equations into the Hermes cold ion code, the numerical results revealed that the Zonal flow rate and Geodesic acoustic mode frequency grows with the increase of toroidal rotation rate. Non-inertial effects are proven to be important in generation and propagation of GAM and zonal flow. The non-inertial effects induced by toroidal rotation are proved to be important to GAM and ZF.

Finally, 4-field reduced-MHD equations were also derived in a non-inertial rotating frame. Linear and non-linear simulations were performed under BOUT++ elm code. We find the ELM size can be suppressed by rigid toroidal rotation, when considering non-inertial effects. Results suggest that velocity shear and pressure perturbation phase shift , caused by centrifugal and Coriolis effect respectively, are the key mechanisms in rotation's effect on ELM mitigation.

Acknowledgements

This thesis would not have been possible without the support I have received over the last four years from a vast number of individuals within the fusion community. Primarily I wish to express my gratitude to my supervisor, Ben Dudson, for his enthusiasm, guidance, and always making time for me.

I have also been fortunate enough to work closely with Jarrod Leddy, Brendan Shanahan Yulin Zhou, Qing Zhou and Na Wu who have both been extraordinarily helpful, and have provided many fruitful discussions.

Lastly I wish to thank my parents, who have always supported and encouraged my education. I would also like to express my deepest gratitude for my beloved wife, Meng , who supports and encourages me with all her effort in all those years. Her companion and love are always my source of endeavor and lighthouse of effort.

Declaration of Authorship

I declare that the work in this thesis is my own and that it has not been submitted for examination at this or any other institution for another award.

Aspects of this work have previously been presented in the following publications:

Section 4.6 is based on Qing Zhou, Xinliang Xu, Jie Wen, Lin Nie, Changjian Tang, and YubinGong. “Poloidal rotation driven by electron cyclotron resonance wave intokamak plasmas.” AIP Advances, 7(10):105021, 2017

Contents

List of Figures

Chapter 1

Introduction

1.1 Basic relevant concepts for fusion

1.1.1 Background

After the industrial revolution, energy has gradually become a fundamental issue that restricts the development of human society. With the depletion of fossil fuels, the search for new energy source is urgent. In that situation, it becomes a vital and emergent issue to develop new and clean alternative energy[1]. Benefiting from the huge nuclear energy released during the nuclear reaction, nuclear energy is unanimously considered to be the key to solving the energy crisis[2].

The use of nuclear energy can generally be divided into two ways: nuclear fission and nuclear fusion. Since the Soviet Union built its first nuclear power plant in 1954, nuclear reactors now are built worldwide and applied widely to commercial energy supplement . However, nuclear fission is also constrained by factors such as scarce reaction materials, huge nuclear radiation, intractable nuclear waste, and controversial safety[3]. Therefore, as a rich, efficient, safe, almost pollution-free nuclear reaction, the use of nuclear fusion energy are drawing increasing attention. To obtain a fusion reaction, nuclei must be sufficiently close together. Therefore, high temperature is required for nuclei to overcome repulsive force[3].

With the gradual deepening of fusion research, scientists found it difficult to achieve controlled nuclear fusion. Since it requires the maintenance of high-temperature atoms and high density reactive material for a certain period of time, aiming to provide sufficient energy to overcome the barriers between atomic nuclei. In addition, as a kind of commercial commercial supplement, net energy gain is also required. In 1957, British scientist Lawson summed up the basic principle factor for plasma self-sustained combustion and gave criteria for the condition to achieve fusion[4]:

$$nT\tau_E > 10^{21}m^{-3}skeV. \tag{1.1}$$

Where n, T, τ_E are the density, temperature(keV) and confinement time of reacting substance receptively. From the expression of Eq.(1.1), scientists concluded two approachable ways to meet the criteria: the high density short confinement time of inertial confinement fusion (ICF), or the low density long confinement of magnetic controlled fusion (MCF)[4]. ICF is the method of converging reactive material onto a small fuel target (typically a pellet made of deuterium and tritium) using multiple lasers and X rays. In the process of reaction, material of the fuel surface evaporates instantaneously and project outwards intensely. Thus generates a strong reaction force pushing the particles to the center, which make the fuel reach high temperature and high pressure in a mean short time by particle inertia . MCF is based on the fact that a charged particle traverses a magnetic field and is constrained by a Lorentz force, hot plasma is confined in vessel by magnetic field to meet the Lawson criterion. There is still no definite result that shows which approach is superior. ICF has a target to reach ignition, while MCF is more practical and closer to reaching the economical purpose.[4]

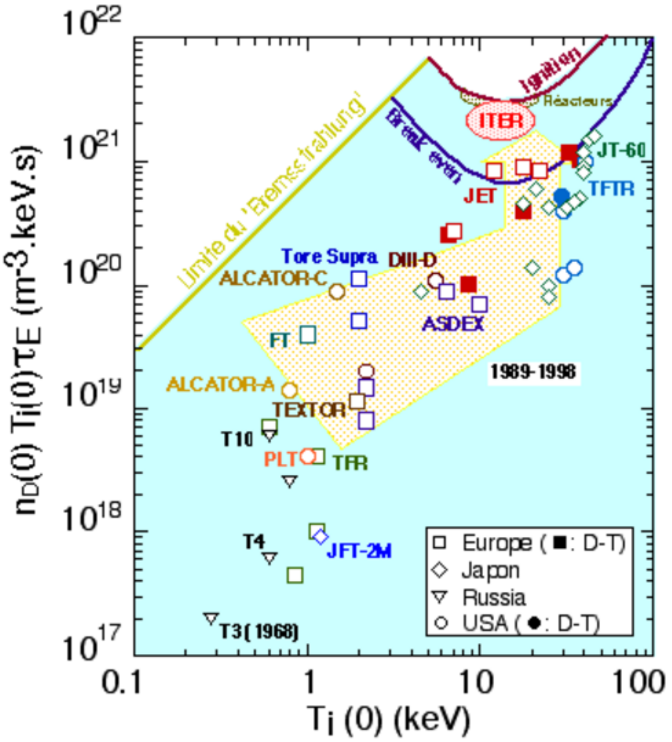

Figure 1.1: The triple product (density, temperature and energy confinement time, see also Lawson's criterion) plotted against the centre plasma temrerature. The yellow arrow shows the progress accomplished in the course of the recent decade 1989-1998. The open symbols correspond to experiments with deuterium plasmas, and the solid symbols to plasmas of a mixture of deuterium and tritium. [5]

The current operating magnetic confinement devices are mainly divided into several categories: Stellarator, Reversed field Pinch, Mirror machine, Spherical torus and tokamak. Among those different types, the Tokamak, as a mainstream device for magnetic confinement fusion research, has achieved considerable development in recent years and are continuously approaching the break-even. In the 1960s, the "triple product" reached $10^{15} m^{-3} skeV$ firstly, with more than half century's development, the value of "triple product " ran up to $1.5 \times 10^{21} m^{-3} skeV$ in recent years. Meanwhile, in the JET and TFTR Tokamak devices, fusion powers from nuclear reaction achieved 16.1 MW and 10.7 MW respectively. The confinement time of the former device also attained 1 second. Currently, the ITER (International Thermonuclear Experimental Reactor) device , which is studied and constructed jointly by more than 7 countries and unions, us expected to attain 4 seconds' energy confinement time with more than 15 keV's core temperature.

1.1.2 Tokamaks

Tokamak devices mainly use a magnetic torus to confine charged particles. The basic structure is shown in Figure 1.2, the toroidal field is generated by external fields. However, solely toroidal field is not enough to confine plasma, due to the non-uniformly of the toroidal magnetic field , charged particles are affected by the curvature and gradient of the magnetic field . This will cause the constrained particles to be lost continuously on the weak field side and eventually break the confinement.

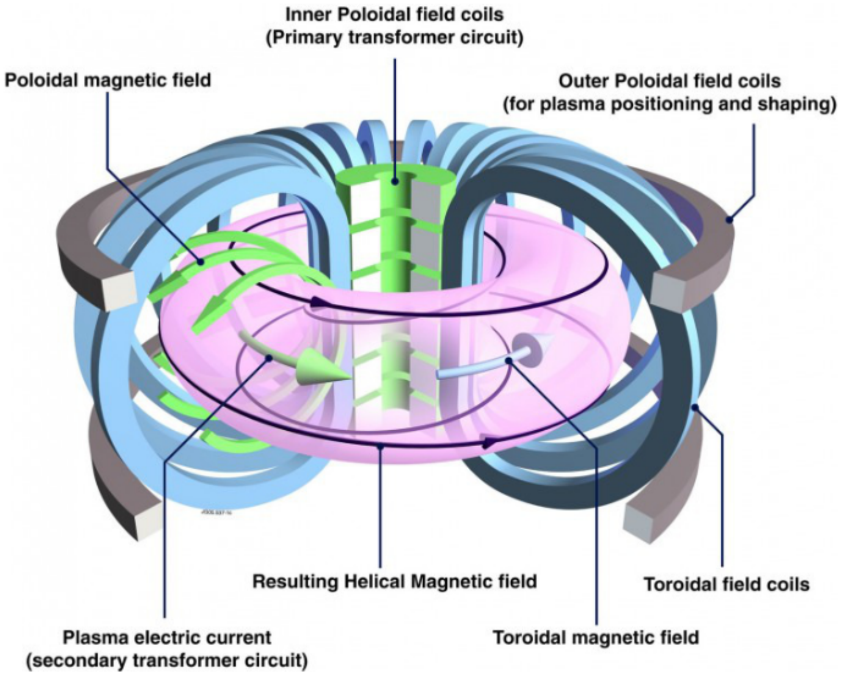

FIGURE 1.2: Schematic of a tokamak.
[6]

In a non-uniform magnetic field, the positive and negative charges drift in opposite directions. This makes the separation of charges and the forms an electric field perpendicular to the magnetic field. Under the effect of $\mathbf{E} \times \mathbf{B}$ drift, drift velocities of charged particles become asymmetric in the cross section. Particles drift outward in the weak field side and drift inward in the strong field side. Therefore, the tokamak device introduces a poloidal magnetic field besides the toroidal magnetic field, which makes particle orbit switch between the high field side (HFS) and the low field side (LFS) periodically, resulting in particle's average drift tends to zero.

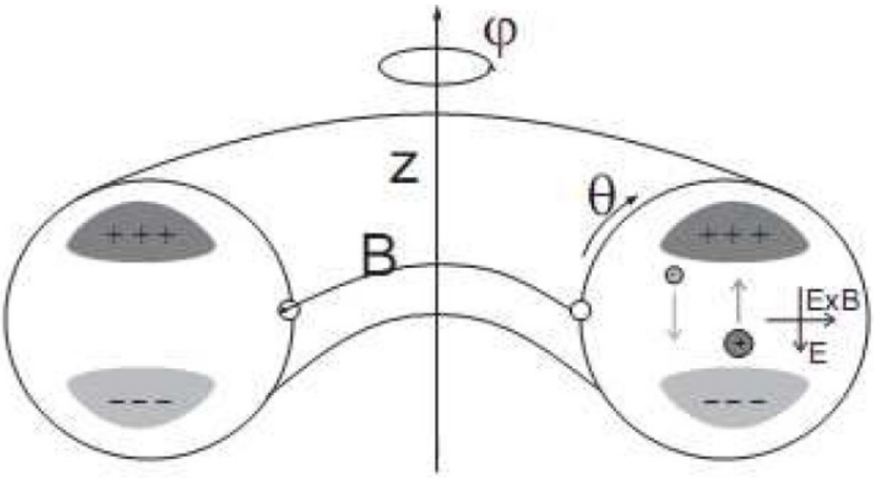

FIGURE 1.3: Charge separation and $\mathbf{E} \times \mathbf{B}$ drift in tokamak.
[7]

Since the existing of both the toroidal and poloidal field. The magnetic field lines are twisted in a polar magnetic field. Then one can define the safety factor q:

$$q = \frac{2\pi}{\iota} = \frac{d\Phi}{d\Psi} \tag{1.2}$$

Where $\frac{\iota}{2\pi}$ is named the rotational transform, which is defined as the number of poloidal transits per single toroidal transit of a field line on a toroidal flux surface. Ψ is so-called poloidal magnetic flux function, and Φ is toroidal magnetic flux. With the assumption of large aspect ratio in circular tokamak (in the other word, the inverse aspect ratio is small $\epsilon = r/R_0 << 1$), the safty factor can be approximated by

$$q(r) = \frac{rB_t}{RB_p} \tag{1.3}$$

where R and r are major radius and minor radius of tokamak, B_t and B_p are the toroidal and poloidal field respectively. In the experimental study and mode analyze of plamsa instability, the safety factor (the expression of mode structure which aligns to the magnetic field) can also be expressed as:

$$q(r) = \frac{m}{n} \tag{1.4}$$

Where m and n is poloidal and toroidal number, which represents number of turns that field line circle back to original point. If both m and n are integers, it indicates that the magnetic field lines can be "closed" after several transit. The magnetic surface composed of such lines is called rational magnetic surface. On the contrary, field lines on irrational surface can not close within limited circles. In magnetically confined plasma, the oscillations of current, pressure. etc can cause resonance with magnetic field on rational surface . Therefore, the main concentrations on tokamak instability studies are focused on rational surface physics.

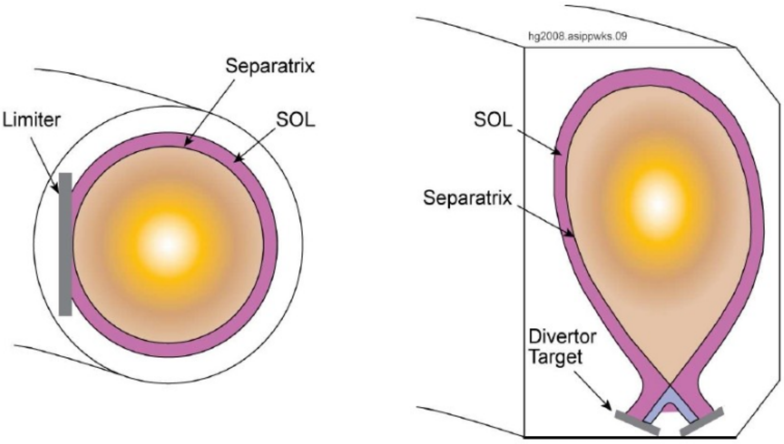

Figure 1.4: Tokamak limiter configuration(a) and Divertor configuration (b) [8]

In tokamaks, the solid wall facing the plasma inside the vacuum chamber is called the first wall. Due to the extremely high temperature and density of the plasma, the first wall is easy to be damaged. Therefore,to avoid heat particles heating the first wall, the magnetic flux lines of the outermost layer are generally opened artificially to form a transition layer. The plasma in the vacuum chamber can then be divided into two regions: the scraping layer SOL (Scrape-off Layer) and the confined zone . The boundary between them is defined as the last closed magnetic surface LCFS (Last Closed Flux Surface). In the confined zone, the magnetic flux is closed, which is the main area that confines the plasma. This area can be further subdivided into Main Plasma (MP) and Edge Plasma (EP) . In the SOL, the lines of magnetic force are open, plasma parameters and profiles (ie. pressure,current and temperature) decrease rapidly from MP to SOL in the radial direction, providing protection for the first wall.

There are two kinds of shape or configurations of tokamak, the limiter configuration and divertor configuration, shown in Figure 1.4(a) and Figure 1.4(b) respectively. The installation of one or more restricting metal hole bars close to the internal edge of the first wall block the magnetic field lines to make field lines open. The advantage of this approach is easy to control. The divertors configuration is to introduce one or two independent small-scale annular divertor outside the EP. The main function of divertor focus on making the magnetic filed on confinement zone connect to the divertor magnetic field . The critical point of re-connection is named X-point, the magnetic field lines inside the X-point remain closed, and the magnetic field lines outside the X-point are introduced into the divertor. The advantage of this configuration is that most of the particles and heat flow can be directed to a specific divertor target plate, and limit the impurity generated by plasma and target panel back to the confinement area effectively.

Experiment results have found that it is still hard to confine the particles in the tokamak a long time with poloidal fields. This indicates that there is still a strong radial particle and energy transport process in Tokamaks, which has strong correlation with tokamak operating mode. Since then, it is important to study the operating modes in tokamak.

1.2 H mode and L-H transition

1.2.1 Intoductions to L and H mode

In the tokamak discharge experiment, based on different discharge conditions and macroscopic parameter distribution. Scholars divided them into three different confinement modes: Ohm confinement mode, low confinement mode (L mode), and high confinement mode (H mode).

In the early experiments, Ohmic heating (transformer produce the changing magnetic fields to create high-intensive current and heat plasma through induction) was the primary method. However, with the increase of plasma temperature, the resistance of plasma decrease severely, which is inversely proportional to the 3/2 power of the electron temperature. Therefore, the heating efficiency is significantly reduced as the temperature increases. This kind of resistance was first obtained by Spitzer and is named as Spitzer conductivity[9]. With the presence of Spitzer conductivity, the plasma is far from reaching Lawson criteria with Ohmic heating alone. In order to raise the constrained plasma temperature T, scientists have developed a variety of auxiliary heating methods. The main methods include neutral beam heating (NBI), low-hybrid heating (LHRH), ion cyclotron resonance heating (ICRH), and electron cyclotron resonance heating (ECRH)[10]. However, in the experiments with with those auxiliary heating, plasma confinement time decreased significantly with the increase of plasma temperature. That makes the "triple product" can not reach the minimum required value. This confinement mode is defined as L-mode.

With the development in the auxiliary heating technique and tokamak, new confinement mode is obtained. In the year of 1982, an enhanced confinement mode is discovered in the experiment of ASDEX when the auxiliary heating power exceeded a certain threshold at a high density[11]. On the contrary to L-mode, the energy confinement time in this enhanced mode, does not decrease with plasma temperature dramatically. In the ASDEX team's observations, the confinement time $\tau_L \approx 40ms$ can be improved up to $\tau_H \approx 150ms$ from L to H mode. That makes it approachable to reach and maintain a higher fusion energy gain factor Q, defined as the ratio of fusion power produced in a nuclear fusion reactor to the power required to maintain the plasma in steady state. At the same time, in this mode, the plasma edge region transport coefficient is reduced severely, along with the increase of plasma density and temperature gradient. And the profile of density and temperature become steep near the boundary. Since this mode has much better confinement performance, it is also named as high confinement mode (H mode). Ion temperature increase but edge density decrease signifantly from L mode to H mode.

Many MCF device (tokamaks, stellarators etc.) have observed H-modes. In addition, it has been experimentally proved that various heating methods can achieve H-modes, such as NBI (ASDEX, 1982); ECRH (DIII-D, 1988); ICRH (ASDEX, 1987); LHRH (JT-60, 1990). There are even some devices that implement the H mode in the case of ohmic heating alone, such as DIII-D (1990), ASDEX (1992), Compass-D (1994) and MAST(1995) .

In the study of L and H mode confinement time, the scaling law is used to reveal the dependence of confinement time on tokamak variables[12]. The energy confinement time is defined as a function of the global plasma energy content W, and the applied total heating power P[13]:

$$\tau_{E,th} = \frac{W}{P - dW/dt} \tag{1.5}$$

It is one of the main figures of merit of magnetically confined plasmas. Since the heating methods of these devices are different, the discharge patterns are various, but the H-modes obtained by them all have similar parameter distribution characteristics(profiles of density, current and pressure, etc). The estimated energy confinement time is usually obtained from database of tokamaks. The typical energy confinement scaling, such as IPB98(y,2)[12], has the expression:

$$\tau_{E,thIPB98} = 0.0365 I^{0.97} B^{0.08} P^{-0.63} n^{0.41} M^{0.20} R^{1.93} \epsilon^{0.23} \kappa^{0.67} \tag{1.6}$$

Where $I(Unit : MA)$ is the plasma current, $B(Unit : T)$ denotes the toroidal magnetic field, $n(10^{19}m^{-3})$ is the central line averaged density, $P(MW)$ is the absorbed power, $R(Unit : m)$ is the major radius, and the dimensionless factor M , κ and ϵ are the hydrogen isotope mass, elongation and the inverse aspect ratio respectively. Fig.1.5 demonstrate the experimental confinement time and energy confinement scaling of some major devices in the world. From the figure, one can see that predicted confinement time comes with fine agreement with experimental results. Therefore, it is possible to estimate ITER's (International Thermonuclear Reactor) confinement time, since H mode will be one of its standard baseline operating scenario[12].

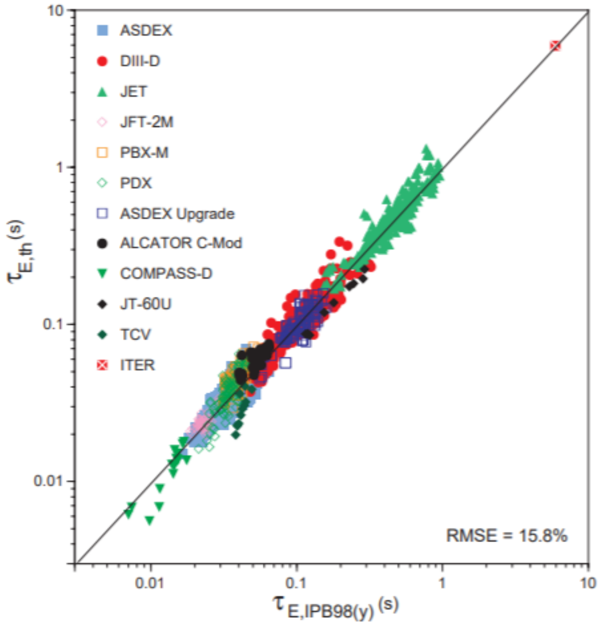

FIGURE 1.5: H mode measured confinement time (y axis) vs. Predicted confinement time in different device.

[14]

1.2.2 L-H transition

The process of overcoming the power threshold from L mode to H mode is called L-H transition. To obtain and keep a steady H mode, it is of great importance to understand the physics and character changes during the process of L-H transition. From the experiment of JET in Figure.1.6, with the input of auxiliary heating, one can find out that the D_α signal has a significant decrease around 18.0 seconds, indicating that the outward transport of the plasma drops sharply. At the same time of this L-H transition procedure, a large rise occurs in ion temperature T_i, flow shears also become severe in this process.

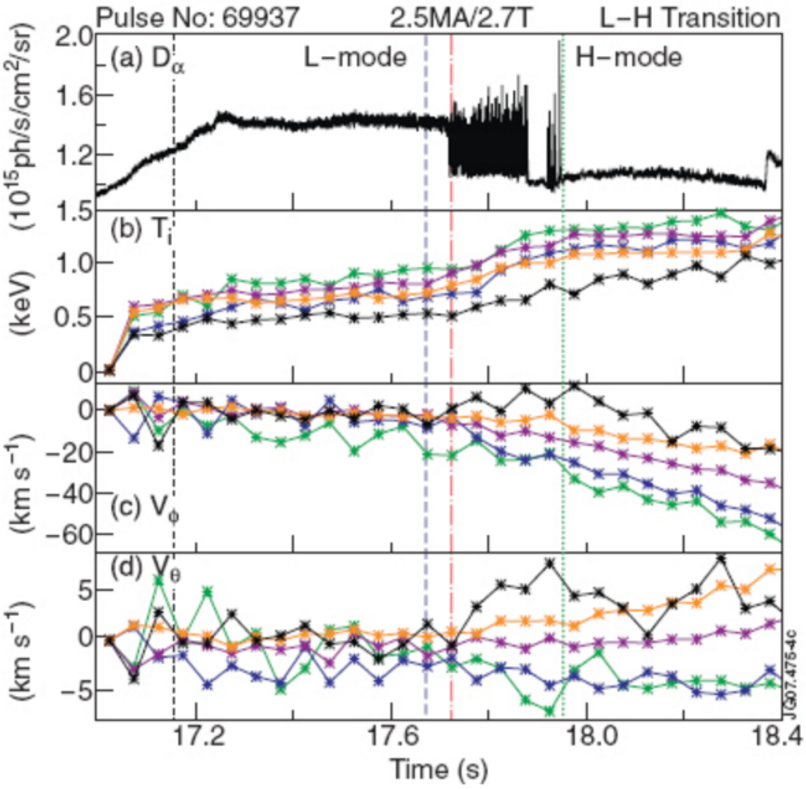

FIGURE 1.6: L-H transition in JET, the above figures are the time evolutions of (a) D_α , (b) ion temperature, (c)toroidal and (d) poloidal velocities. Different color indicate the data in different poloidal position.

[15]

In an experiment on DIII-D (Figure.1.7)[16], with the development of the H-mode, it can be seen that the core density profile is gradually flattened, and the relative edge-density is rapidly steepened. At the same time, the spatial scale of density gradient peaking is becoming narrow. After the full development of the H-mode

(105ms), it is apparent that the density profile is significantly different from the L-mode. In the experimental measurement of the H mode in different devices, the density profiles always become steeper in a small interval (0.5-3 cm). This area is called the edge transport barrier (ETB), also known as the pedestal zone. The width of the area is defined as the width of the pedestal, and the maximum value of this area is defined as the height of the pedestal. Besides the critical improvement of density and temperature' profile and gradients(shown in Fig.1.7) , a peak of current also occur in pedestal region(Fig.1.8). The current and current gradient will induce some instabilities, which will be discussed in section 1.3 and Chapter 3.

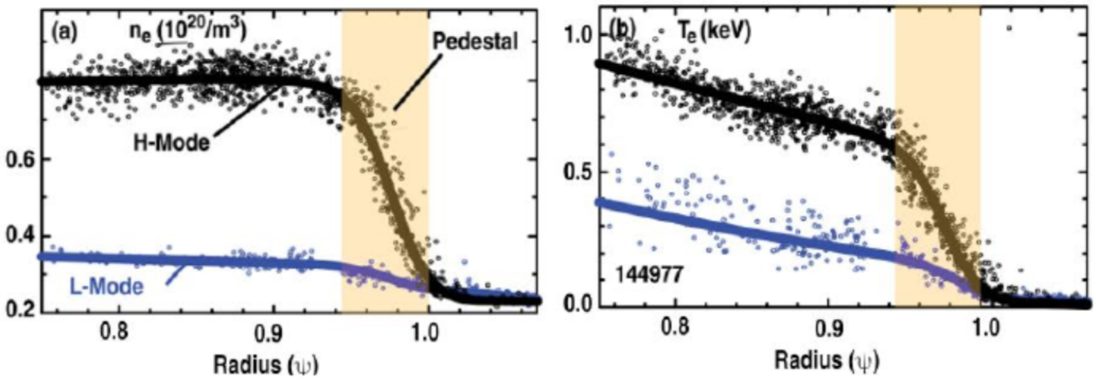

FIGURE 1.7: The typical pedestal electron density(left) and temperature(right) of L and H mode in DIII-D.

[16].

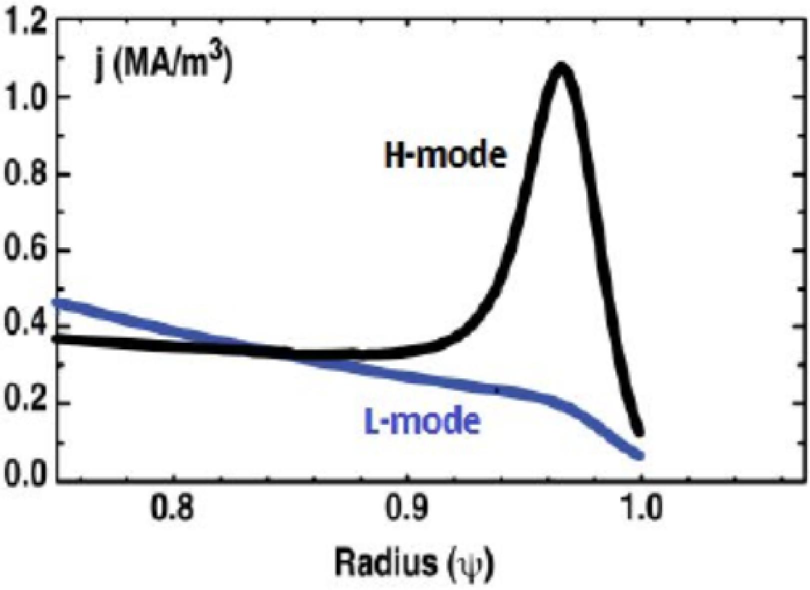

FIGURE 1.8: The typical current profile of L and H mode, regenerated from DIII-D's data.

[16]

Edge transport suppression means the improvement of confinement. Although the confinement time of H mode also decreases with heating power's growth, it is still 2-3 times the energy confinement time of L-mode. On the other hand, longer energy confinement time also means enhancement of impurity constrain. This leads to the rapid rise of thermal radiation caused by the impurity particles , resulting in the aggravating of energy loss. It is impossible to maintain H mode anymore when impurity's fraction reaching a high rate. At this time, the H mode will be converted back to the L mode. Therefore, the pure H mode is actually difficult to be maintained all the time in the experiment.

Fortunately, experiment on JET revealed that there is a self-regulating mechanism for H mode, that is, periodic outburst oscillation [17]. This kind of instability is usually called Edge Localized Mode (ELM)[17, 18]. The oscillating mode causes the ETB of the H-mode to collapse periodically, while releasing a large amount of energy and particles. And then ETB will be quickly rebuilt due to the continuous injection of external particles and heating power. The process of ELM crash is generally very fast, which takes around 1ms. This process benefits the emission of impurities and stabilizes the H mode discharge. This kind of H mode with ELM is usually referred as the ELMy-H mode. At present, most of the devices are mainly operating with ELMy-H mode. However, the side effect of ELMy-H mode is also serious. Since the ELM emits a large amount of energy and in a short duration, it will bring a huge instantaneous thermal load to the first wall of the device and the divertor (especially type I ELM). Therefore, the current research on ELM mechanism and mitigation has become the urgent task of fusion research. In the process of L-H transition, the flow shears and rotation are believed to play an important role[15], especially with shear flows[19], in which zonal flow is one of vital shear flow . The physics of zonal flow will be discussed in section 1.4 and Chapter 4.

1.3 Edge localized modes(ELMs)

1.3.1 Definition

As it mentioned in the previous section, the H mode is a possible main operating mode for ITER and future devices. In the ITER plan, the ELM-H mode is one of the most important operating mode, since it is a possible way of maintaining H mode (shown in Figure.1.9). With the progress of experiments, the data of ELM is becoming more and more abundant, which provides a lot of data for further experimental and theoretical research.

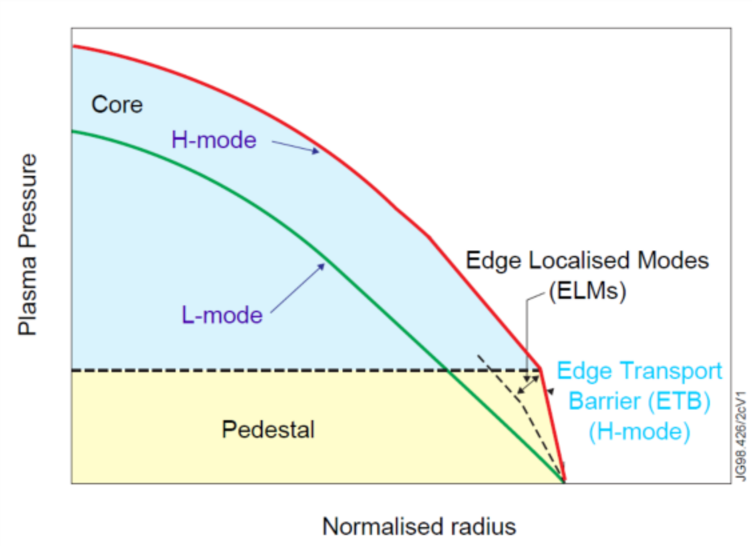

Figure 1.9: The H-mode and L-mode typical pressure profiles and the effect of losing plasma energy from the edge plasma as a result of an ELM; not only is there a reduction in the edge gradients and a lowering of the edge pedestal, but this leads to a reduction in core confinement, particularly for stiff transport models

[20]

Generally, ELMs are defined as repetitive eruptions of particles and energy which occur in some H mode plasma[21]. In the experiment, spikes of D_α trace(emitted by the interactions between neutral particles and electrons), measured near the seperatrix region, are widely used to indicate crashes and recovery of ELMs (Fig.1.10). The eruption itself ELM is a local instability mode originating from MHD instability and mainly occurring in the pedestal region. And is now generally considered to occur when the pressure gradient in the base region reaches a certain threshold. It makes the crashes of ETB on the boundary, and releases some energy and particles. After ELM crash, the ETB is re-established and goes to next circle. In Figure.1.11, an intuitive image of discharge are displayed to illustrate ELM crash.

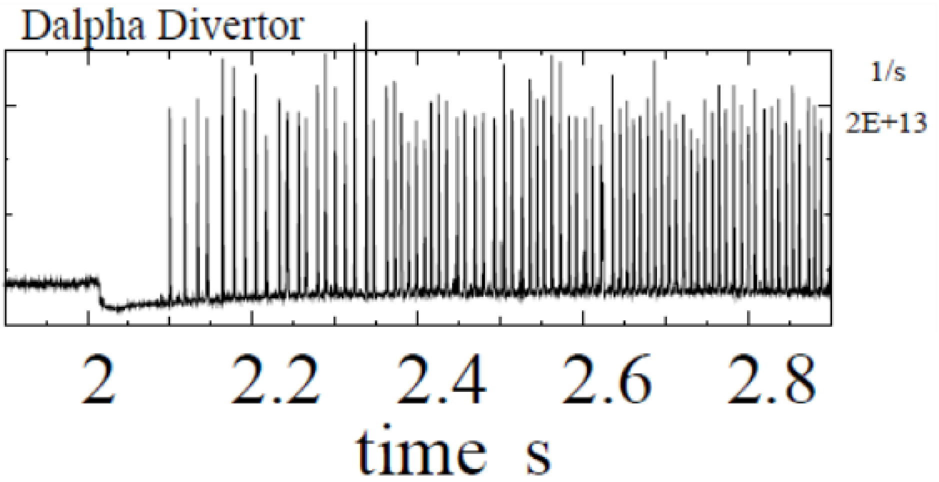

FIGURE 1.10: The measurement of D_α traces indicating ELMs [22]

1.3.2 ELMs in experiments

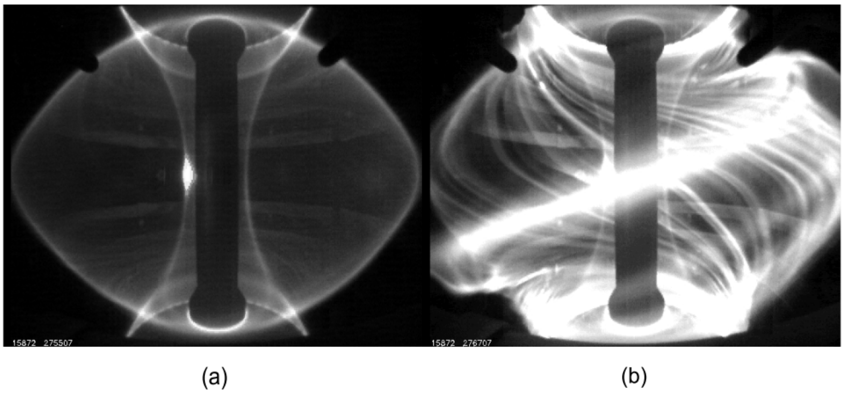

(a)
(b)

FIGURE 1.11: (a) Inter ELM H-mode in MAST. (b) An ELM eruption in MAST [22] .

In the experimental exploration of ELMs, scholars found that the characteristics of ELM are not exactly the same. Under normal circumstances, based on relationship between heating power and ELM burst frequency, ELMs are divided into three types[23].

Type I ELMs: The burst frequency of this type of ELM grows with heating power. And its occurrence causes an isolated, sharp outburst on the D_α signal.

Type II ELMs: If tokamak trangularity keeps growing during type I ELM , then the characters of type I ELM may change: the frequency increases, and the D_α signal amplitude decreases. For Type II ELM, there is no obvious dependence of the burst frequency on the heating power.

Type III ELMs: To the oppsite of type I ELMS, the burst frequency of this type decreases with the heating power. This type of ELM often occurs at low power and high collisional plasmas, which is not compatible with high performance operating.

Generally, the type I ELMy-H modes are one of most common modes. In addition, the physics of type I ELMs are less complicated that the other two. Therefore, the main focus of this thesis is type I ELMs.

1.3.3 Theoretical reviews of ELMs

Gohil et al simulated the type I ELM discharge in DIII-D using an infinite ideal ballooning mode [24], and analyzed the ELM mechanism using Magneto hydro dynamics (MHD) stability methods. They found that the plasma edge pressure gradient continue to grow until it reaches a certain threshold. Subsequently, the pedestal crashes and type I ELM occurs. Nevertheless, this conclusion is the linear result of non-resistive mode. After that, the theory of ballooning mode was developed, resistive ballooning mode[25] and kinetic ballooning mode[26] is proposed.

Zohm et al analyzed the type III ELM in ASDEX using a nonlinear calculation in a free-boundary cylindrical geometry[27]. They found that a turbulent mixture with a nonlinear resistive exchange mode can induce a distortion instability, under a sufficiently strong boundary current density gradient and pressure gradient. The edge profile then crashes and causes intense radial transport. This mode is known as the peeling mode, where both the boundary plasma current and the pressure gradient provide energy for this instability.

Concluding previous theoretical studies, Synder et al proposed the coupled peeling-ballooning mode[28], which predicts operational regimes where pedestal pressure and bootstrap current lead to peeling unstable or ballooning unstable modes. The peeling ballooning mode is well accepted and wide used theory in ELMs studieswhich described the conditions of different types of ELMs qualitatively(Figure.1.12). The Fig.1.12 gives the threshold spectrum of bootstrap current J and edge pressure gradient ∇P of three different types of ELMs. However, Webster and Gimblett do not agree with this argues that the peeling mode could occur, but its growth rate can be arbitrarily small near the separatrix[29]. Hence, it is essential to explore the coupling of the peeling and ballooning modes and other effects leading to ELMs. We will explore this topic in chapter 3.

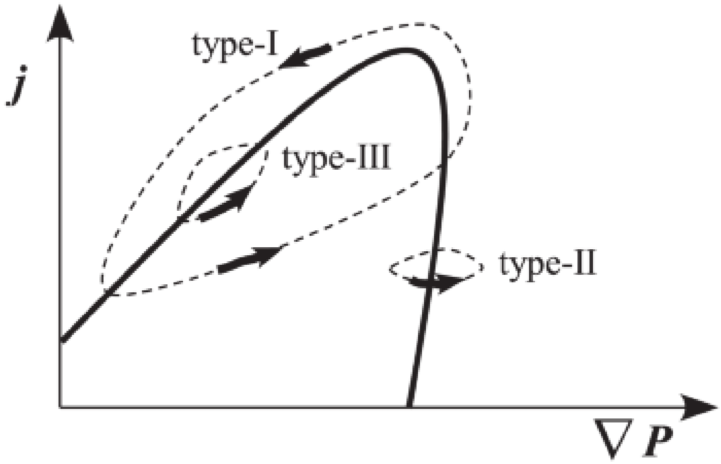

FIGURE 1.12: The image interpretation of the relationship between the bootstrap current J and the boundary pressure gradient for the three ELM crashes, the black solid line represents the ideal scraping balloon mode stability zone, and the dashed line represents the possible trajectory of the ELM burst. [30]

In addition, the effects of flow shear on different MHD instabilities have been discussed in numerous analytical studies[31]. Resistive wall modes can be stabilized by sufficiently fast toroidal rotation; ballooning modes are stabilised by sheared toroidal flows[32]. Experimental work on KSTAR also suggests stabilization of pedestal instabilities due to toroidal rotation[33]. In addition, the energy losses of ELMs have been shown to be reduced by counter current direction NBI heating in JT-60U [34]and DIII-D [35].

However, all the simulations and analysis work on rotation and flow shear effect are treat the shear flow as a correction term, which are not self-consistency modes. Therefore, it is needed to develop a self-consistency on the influences of plasma rotation and flow shear on ELMs. Related studies will carried out in chapter 5.

1.3.4 Methods in ELM mitigation

At present, the methods of ELM mitigation can be divided into active and passive ways. The passive method mainly puff cold plasma or impurity gas in the divertor chamber to generate off-target plasma. This method can significantly reduce the temperature of the divertor, but neglect the ELM's influence on plasma. The positive method mainly focus on directly changing the behavior characteristics of ELM. The active control methods mainly include Resonant Magnetic Perturbations (RMP), pellets injection, radio frequency (RF) heating and so on.

The method of RMP has achieved relatively successful results on DIII-D, ASDEX-U, JET and MAST devices[22, 36, 37]. RMP forms a stochastic magnetic field at the edge of the plasma, enhances particle transport (but has little effect on energy transport, its mechanism is unclear) The mechanism is to make pedestal plasma pressure and current under Peeling-Ballooning mode stability threshold. However, the applying of RMP cause plasma pump-out, leading to weaker energy constraint.

The method of Pellet ELM Pace Making mitigate ELM by adding pellet on pedestal to trigger ELMs to reduce the level of ELM crash[38]. But the pellets are hard to control since large pellet are found to break the plasma confinement[39].

Another method is using Electron Cyclotron Resonance Heating (ECRH) to change the pedestal pressure gradient to suppress the ELM. which has been achieved in TCV devices[40](Fig.1.13). By heating the plasma directly in pedestal regions, the pressure profiles are changed, then the characteristic of ELM will be changed. Then ECRH can trigger small ELMs more frequent by avoiding large size ELM. The experiments in ASDEX-U also reveal that edge ECRH can mitigate ELM by increasing the natural ELM frequency, and decreasing the energy loss per crash[41]. Moreover, ECRH is unparalleled in its degree of localization of the power deposition. Therefore, ECRH can be a potential method to mitigate ELM. We will also address short discussions in chapter 4 and appendix A about this idea.

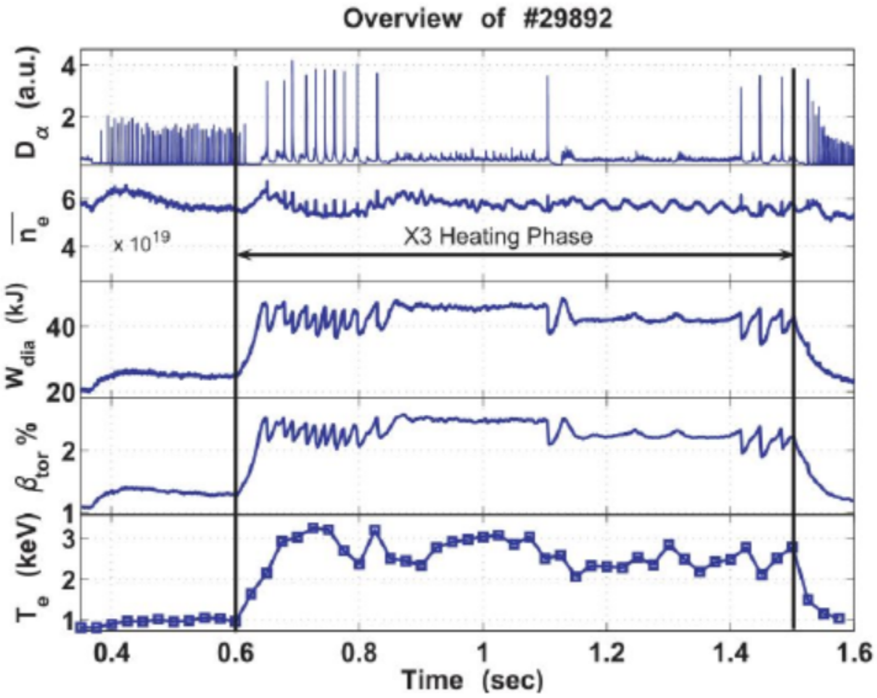

FIGURE 1.13: ELM was significantly relieved or even suppressed from 0.8s after the injection of ECRH. The y axis in each graph (from top to bottom) is D_α, electron density, energy, β and electron temperature.

[40]

1.3.5 The Quiescent H-mode

Benefiting from the improvement of core transport and impurity control[20], ELMy-H mode is one of most significant most operating mode in current and further machines[42]. However, ELMs can also produce significant erosion in the divertor and the first wall. Due to this intolerable bursty heat loads, ELM becomes one of the the serious concerns for next generation devices such as ITER[42]. Under that circumstance, possible solutions are required which still possess good H-mode confinement and sufficient edge particle transport for impurity exhaust but have good mitigation of ELMs.

Among the ELMy-free H mode, the Q-H mode is supposed to access higher and wider pedestal pressure[43, 44], and give rise to a path to the Super H-mode regime with very high pedestals[44]. Therefore, the Q-H mode is suggested to be one achievable higher performance H mode in ITER and further devices[45]. In the

First discovered on DIII-D[46] and obtained later on other machines like ASDEX-Upgrade[47], JT-60U[48] and JET [49], Q-H mode is proved can retain good confinement and impurity transport as ELM, but avoid impulsive heat load problem. Under the operation of Q-H mode, the confinement time can reach 4s in DIII-D. The fusion performance is close to the goal of $Q = 10$ performance on ITER. In the experiments of DIII-D, Q-H modes are proved to operate at high pedestal density and temperature profiles as ELMy-H mode (shown in Fig.1.14).

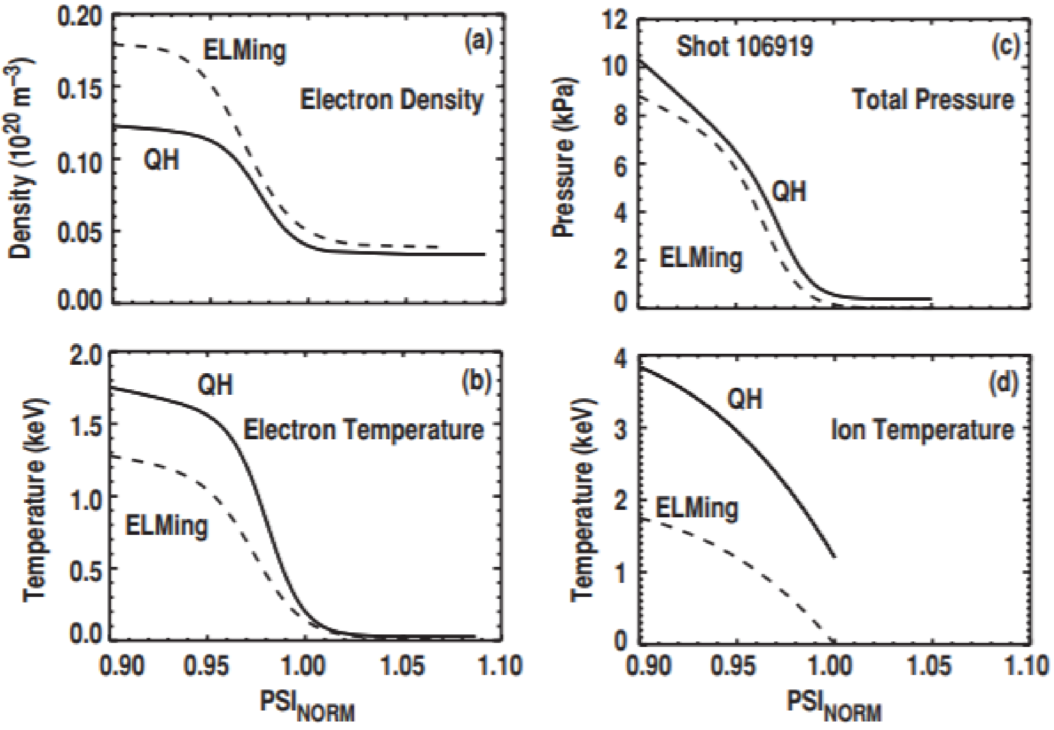

FIGURE 1.14: Fits of (a) edge electron density, (b) temperature, (c) total pressure and (d) the ion temperature for a QH phase (solid line), shot 3000 ms, and ELMing phase (dashed line) at 1210 ms (shot 106919)

[50]

First, QH-mode plasmas on DIII-D and other devices were obtained under the injection of counter-current NBI [51]. Later, Q-H co-current NBI injection was also observed on DIII-D[52]. Further on, Q-H mode operation was achieved by both counter-current[53] and co-current rotation shear[54] at low NBI toque, with the use of non-axisymmetric fields.

In the theoretical researches, the low-toroidal (n) mode number multiple MHD oscillation (specifically electrostatic potential), named the edge harmonic oscillation (EHO), is thought to be the key factor causing Q-H mode[55]. The mechanism of

EHO induced Q-H mode is mainly considered as the momentum saturation of low n kink/peeling mode, which mitigates the explosive process of ELM[52]. Varies simulation work using EFIT[45], M3D-C1[56] and BOUT++[57] believe that large edge flow shear plays an important role in driving EHO. However, the dynamics of EHO's formation is still not fully understood, related studies are planned for future work.

1.4 Zonal flow and geodesic acoustic mode

1.4.1 Introductions of Zonal flow and geodesic acoustic mode

The Zonal flow (ZF) is a kind of steady flow along the latitudinal direction, oposed to meridional flow along longitudinal lines. ZF is a ubiquitous phenomenon in nature, such as the light and dark strips in Jupiter's atmosphere (1.15)[58]. These strips of different colors have different rotational velocities.

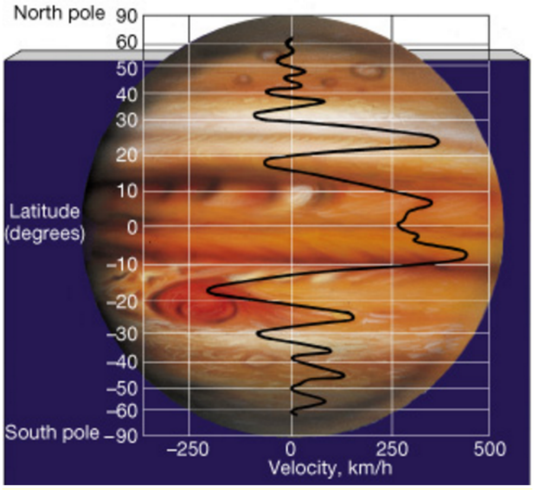

FIGURE 1.15: ZF in Jupiters atmosphere, measured relative to the planets internal rotation rate. Alternations in wind direction are associated with the atmospheric band structure.
[58]

There also exists ZF in the plasma. The ZF in the Tokamak plasma is defined as a flow with symmetrical structure in poloidal direction. The existence of ZF was predicted from theory and simulation, which closely related to the transport phenomenon in magnetic confinement fusion[59]. Also, the presence of the zonal flow was observed in the experiment[60]. Recent researches show that ZFs can effectively mitigate the turbulence transport(Figure.1.16), and thus, improve the confinement of plasma and promote L-H transition[61]. On the other hand, the geodesic acoustic mode (GAM), the high frequency branch of zonal flows, also received increasing attention, which also plays a key role in H mode operation[25].

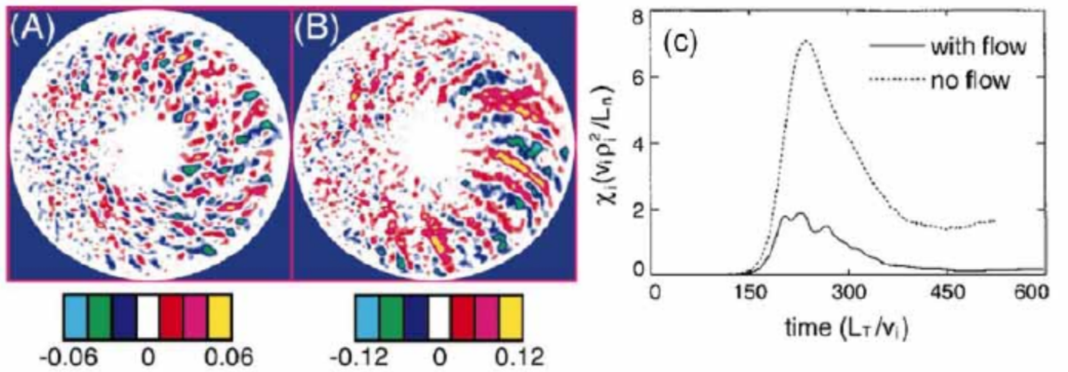

FIGURE 1.16: a) Voticity of turbulence (eddies) with ZFs b)Vorticity of turbulence without ZFs c)Ion heat transfer coefficient with and without ZFs. From the figure, it is found that ZFs can reduce the scale of turbulence and improve the confinement.

[61]

1.4.2 Basic studies for ZFs and GAMs in plasma

The ZF is an electric field oscillation with a finite radial wave number which is symmetric/approximately symmetric in both toroidal and poloidal directions ($n = 0, m \approx 0$)[62]. It can not absorb free energy from plasma or cause radial transport. There are two types of ZFs, one of them is steady-state, named zero frequence zonal flow (LFZF) or residual; the other has a finite oscillation frequency, known as GAM.[62] Normally, the LFZF is called ZF while the high frequence on is called GAM.

Hasegawa and Mima first proposed the concept of a ZF in the simulation of the Hasegawa-Mima equation[59], which was originally used to describe the drift wave turbulence, which later explained the anomalous transport phenomena in the plasma. Lin et al verified the presence of ZF using the simulations of gyro-kinetic code[61]. The characters of ZFs were then widely studied, and the machanism and damping rates revealed using MHD equations[63–65]. Later, Diamond[62] reviewed those works and summarized that ZFs are related to the drift flow, flow damping and turbulence.

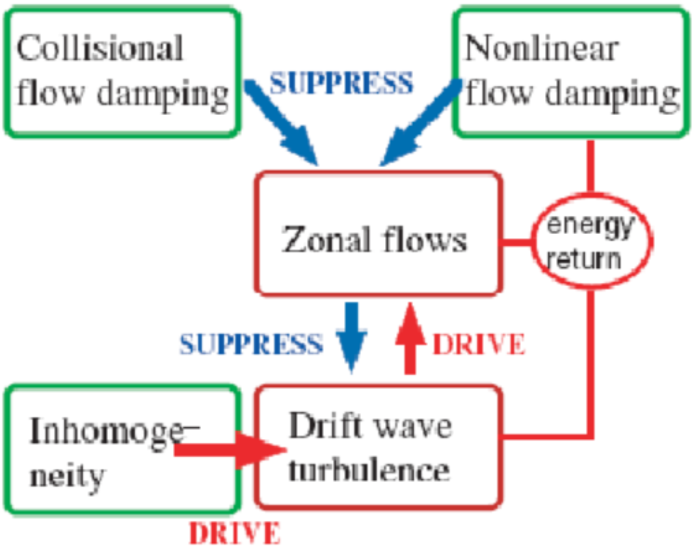

FIGURE 1.17: A physical image of the interaction between drift waves, turbulence and ZFs.

[62]

The GAM was first discovered theoretically by N. Winsor et al. in 1968 [66]. They discovered a new mode when studying the confinement properties of the plasma, and the period of this mode is almost the time required for the sound wave to rotate around the large torus($\approx (\frac{C_s}{R})$, where C_s is the ion acoustic velocity). This mode is also accompanied by a large radial electric field. The density perturbation is a single harmonic (m=1) in the poloidal direction. Winsor et al[66] then derived its dispersion relation. It was found that this mode was caused by the geodesic curvature of magnetic fields, leading to compression of the poloidal EB flow. Therefore, this mode is called the geodesic acoustic mode. In magnetic confinement fusion experiments, the phenomenon of GAM was first observed in the German tokamak device TEXT[67]. Since then, it has been observed on many different devices[32, 68, 69]. Then the damping rate, frequency and propagation characters have also been studied by many scholars[70, 71], which will reviewed in chapter 5.

As reviewed in section 1.2, flow shear plays an important role in the L-H transition and ELMs. As a vital part of shear flow, the study of ZFs and GAMs are necessary.

It has been found that in a non-rotating system, ZFs are linearly stable and the GAMs are standing waves[62]. However, it has been suggested that there exists a critical equilibrium toroidal rotation flow in a tokamak plasma[72].Some authors have solved the eigen value problem of geodesic acoustic modes in such toroidally rotating plasmas using fluid models [73, 74]. However, they mainly studies the effects of rotational correction in non-rotating system, which are not so self-consistent. Therefore, it is of great interest to investigate the effects of toroidal flow on ZFs and GAMs, which will be explored in chapter 4.

This thesis will be arranged as follows: the first chapter reviewed relevant plasma concepts and theories related to this thesis. In chapter 2, we will list and review the methodologies including FCI method, BOUT++, Corsica and Hermes code. In the third chapter, the theory of ELMs crashes, especially the Peeling-Ballooning mode and kink mode are discussed. In this Chapter, we studied the influence of current profiles on ELM crashes, the kink-ballooning mode are proposed and verified by simulation. A rigid derivation of Simokav's cold ion fluid equation is derived under the condition of uniform toroidal rotation in Chapter 4. In this chapter, we also modified the Hermes cold ion model to simulation the rotation's effects on GAM and ZF. In the Chapter 5, we further derived a reduced MHD model to simulate toroidal rotation's effect's on ELM crashes. The conclusions and discussion are lay on last chapter.

Chapter 2

Methodology

The main methods of this thesis is analytic and simulation work, trying to explain experimental and physic problems qualitatively by adding new terms to simulation codes. The main simulation tools used in this thesis are Elm-pb(chapter 3 and Chapter 5) and the Hermes-1 cold ion model (chapter 4), both of them are developed using the BOUT++ framework. The CORSICA tool is also used to generate equilibrium(chapter 3). The outputs analysis of simulation results were developed by the author using MATLAB. In this chapter, the BOUT++, CORSICA and Hermes code will be introduced briefly.

2.1 BOUT++ framework

2.1.1 History and basic functions

The BOUT++ code is an object oriented C++ code. Its predecessor was the Boundary Turbulence (BOUT) code developed X.Xu and M.Umansky in the 1990s . The BOUT code is mainly applied to the numerical simulation of the fluid model of the boundary physics of the plasma in the Tokamak. Developed by Dr. Benjamin Dudson[75], the main objects of BOUT ++ focus on the physics near (both inside and outside) the last closed surface in tokamak geometry, including the physics of the core plasma (not applied for the region near the axis) , scrape-oof layer and the divertor of tokamak geometry.

BOUT++ enables users to build and change the physics problems without requiring lots of numerical works of on the underlying code. BOUT++ consists of routines to handle input/output files, Ordinary Differential Equation (ODE) integrators, definitions of operators and data types for calculating time derivatives and so on.

For the users, only two parts need to be developed: physics-init" and physics-run". Physics-init is the initialization and specification of grids,variables, data and operators, which is only executed once when the program is initialized. physics-run" is used to solve physics models and equations, with choices of derivative and integration operators.

BOUT++'s physical module requires two input files for initialization, an option file BOUT.inp and a grid file to provide grid point information for program execution. The option file BOUT.inp uses the standard text configuration file format, which has the same format as a windows ini file . It contains various parameters that control the simulation process and can be easily edited. By specifying the simulation time, the iteration step number, the solver, the boundary conditions, and other options of equations in this file, users can open or close some terms during the simulation to look into the physic problems.

The equilibrium information can be read from the grid file, including the coordinate system used in the simulation. The BOUT++ code itself does not have a module that calculates the force-balanced equilibrium files. These sort of funcitions are usually fulfilled by other codes such as Corsica and EFIT. BOUT++ can interface to NetCDF or HDFS data file formats, which can be converted from "a file" and "g file" .

The output data of BOUT++ is usually saved into NetCDF files. Due to the parallel computing method, the data will be allocated to different CPUs. So the outputs will be stored in different files based on each process. After the simulation is completed, various numerical analysis tools such as python, IDL and matlab can be used to collect the data from output files generated by each process.

In the following parts of this chapter, the boundary condition and coordinate system of BOUT++ will be introduced briefly. I will also give short review on Corsica and Hermes cold ion mode in last two chapters.

2.1.2 Boundary conditions

There are numerous predefined boundary conditions, such as Dirichlet(zero value) and Neumann(zero gradient), which are available for input file and physics models. Users can also define the position and width of the boundary. Each boundary conditions of variables should be chosen carefully to meet the needs of variables and keep the model self consistent. In the x (radial) direction, there are two boundary cells of each sides of boundary, shown in Fig.2.1. The current density and electrostatic potential of the boundary have the relations (boundary conditions of electromagnetic field):

$$\begin{aligned} \mathbf{B} \cdot (j + j_0) &= 0 \\ \mathbf{B} \cdot \nabla(\phi + \phi_0) &= 0 \end{aligned} \tag{2.1}$$

where j_0 and j, ϕ_0 and ϕ represent equilibrium, perturbed current and potential separately. And the vorticity U is set to zero for the outer boundary cell.

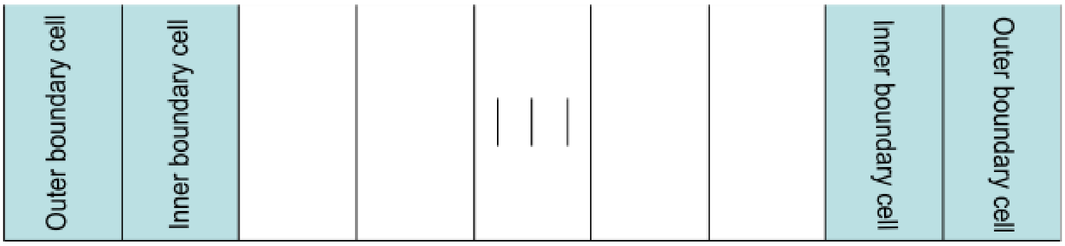

FIGURE 2.1: Grid cells of x direction eclosed with inner and outer boundary [76]

2.1.3 Coordinate system of BOUT++

The field-aligned coordinate system is the main coordinate applied in BOUT++. All the grids are generated and placed in field-aligned coordinate system. The expressions for coordinates are:

$$x = \sigma_{B\theta} (\psi - \psi_0) \qquad y = \theta \qquad z = \sigma_{B\theta} \left(\zeta - \int_{\theta_0}^{\theta} \nu (\psi, \theta)\, d\theta \right) \tag{2.2}$$

where $\sigma_{B\theta} \equiv B_{\text{pol}}/|B_{\text{pol}}|$ is the sign of magnetic field, ζ and θ are toroidal and poloidal angle, ψ is ploidal flux, h_θ denotes the poloidal arc length of field line, ν is the pitch of field line with [75]:

$$\nu(\psi,\theta) = \frac{\boldsymbol{B}\cdot\nabla\zeta}{\boldsymbol{B}\cdot\nabla\theta} = \frac{B_{\text{tor}}h_\theta}{B_{\text{pol}}R} = B_{tor}J/R \tag{2.3}$$

from the definition, the contra-variant basis vector can be written as[75]:

$$\nabla x = \sigma_{B\theta}\nabla\psi \qquad \nabla y = \nabla\theta \qquad \nabla z = \sigma_{B\theta}\left(\nabla\zeta - \left[\int_{\theta_0}^{\theta}\frac{\partial\nu(\psi,\theta)}{\partial\psi}d\theta\right]\nabla\psi - \nu(\psi,\theta)\nabla\theta\right) \tag{2.4}$$

In filed aligned coordinate, the magnetic field is written in Clebsch form:

$$\boldsymbol{B} = \nabla z \times \nabla x = \frac{1}{J}\boldsymbol{e}_y. \tag{2.5}$$

And the contra-variant components of B are therefore:

$$B^y = \frac{B_{\text{pol}}}{h_\theta} \qquad B^x = B^z = 0 \tag{2.6}$$

Hence the expressions of field B has the form:

$$\boldsymbol{B} = \frac{B_{\text{pol}}}{h_\theta}\boldsymbol{e}_y \tag{2.7}$$

where $\mathbf{e}_y$ is the y component of co-variant vector basis. The Jacobian J in this coordinate is defined as:

$$J^{-1} \equiv (\nabla x \times \nabla y)\cdot\nabla z = B_{\text{pol}}/h_\theta. \tag{2.8}$$

The use of Clebsch coordinate systems both benefits some advantages and bring several shortcomings. The main advantage is to make the numerical computation more efficient in turbulence and MHD instability models[77]. Since the parallel perturbation often dominates the plasma oscillations when flute assumption ($k_{||} << k\perp$) is applied. And most MHD equations are written into perpendicular and parallel directions separately[10]. In Clebsch coordinate systems, the parallel derivatives can be simplified to be taken along y direction, benefiting less number of necessary grid points. By aligning a coordinate to the magnetic field, flows along the magnetic field are not mixed with the perpendicular direction. If this is not done, then large parallel flows can lead to numerical perpendicular flows which are bigger than the physical cross-field flows.

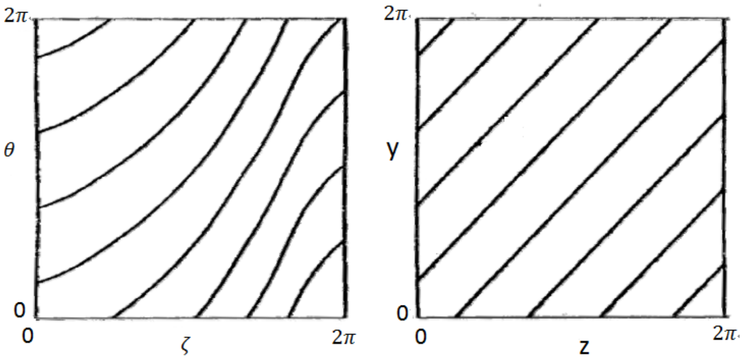

FIGURE 2.2: Field lines in (θ, ζ) (left) and (y, z) (right) space in orthogonal and Clebsch coordinate separately.

[78]

On the other side, there is no way to refrain from shortcomings of field-aligned system. One demerit is that the system has difficulties to deal with physics in complex geometries, such as tokamak poloidal cross section with magnetic nulls or X -points. Since the singularities of metric tensors are inevitable for multiple magnetic topologies[79]. To avoid this topological singularity, grids of separatrix locations are generated independently. However, BOUT++ simulations of geometry with X-points physics are still susceptible to numerical instabilities[80]. A second disadvantage is field-aligned coordinate system is complicated, makes transforming from real space to simulation space error-prone.

Although BOUT++ defined its own coordinate system and grids, it still rely on other codes to calculate equilibrium. Corsica is one of these codes.

2.2 Tokamak equilibrium and Corsica

Grids are also an important input for BOUT++. An equilibrium file is often required for the BOUT++ model. For tokamaks, the Grad-Shafranov equation is a widely used method to generate equilibrium arising from ideal MHD[81]:

$$\delta^2\Psi = -\mu_0 R^2 p^{'} - FF' \tag{2.9}$$

where p is the pressure profile, F relates to $I_p/2\pi$ the poloidal current contributed from coils and plasma. The poloidal flux surface $\Psi = \Psi_p$ is defined as(Fig.2.3):

$$\Psi_p = \int \mathbf{B} \cdot d\mathbf{S}_p \tag{2.10}$$

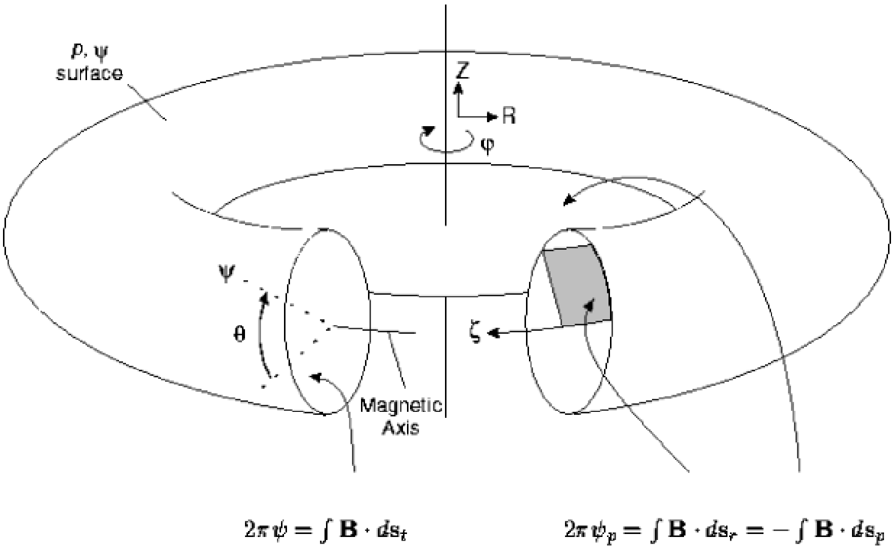

FIGURE 2.3: Sketch of poloidal flux surface function in torus device [82]

CORSICA[83] is an advanced modeling tool to generate grids file suitable for BOUT++ by solving Grad-Shafranov equation. It can generate free boundary (without the wall of plasma) and fixed boundary(with ideal or conductive tokamak walls) equilibrium with various radial and poloidal grids. Users can also change the current and pressure profiles or increase the grids of existing equilibrium by resolving the Grad-shafranov equation. Therefore, it is self-consistent way to get the grids for BOUT++ framework. In Chapter 3, we will use Corsica to generate a new equilibrium for the simulations.

2.3 Hermes cold ion mode

To study the edge turbulence and ion, momentum, heat transports. A 5-field reduced 2-fluid MHD code was developed in the BOUT++ framework[84]. The basic equations of Hermes follows the equations derived by Simokav[85]. Because of the increasing complexity and difficulties in numerical simulations for full drift-fluid model. When the ion ion diamagnetic effects(for example, core region plasma with little pressure gradients) and ion viscous are not the mains concerns of the study. Model can be reduced to cold ion model by assuming the ion thermal pressure $p_i = eT_i = 0$. This is a common assumption in fluid turbulence codes such as STORM[86, 87], ESEL[88], GBS[77]. It simplifies the equations by removing the ion viscous forces and the difficulties associated with the ion diamagnetic cancellation (the near, but not exact, cancellation between the ion diamagnetic advection, and ion gyroviscosity terms in the momentum and ion energy equations). The cold ion assumption neglects the ion diamagnetic effects, which tend to suppress small scale instabilities, but retains the essential effects required here, including radial force balance, plasma momentum, the ballooning, peeling and kink instabilities which cause ELMs. Because the ions do not experience a diamagnetic drift, some effects are not included, such as the ion pfirsh-schluter flow, although the pfirsch-schluter current is included through the electron diamagnetic terms. Equations evolve the of density n, electron pressure p_e, vorticity ω and Ohm's law :

$$\begin{aligned} \frac{\partial n}{\partial t} = -\nabla \cdot \left(n\mathbf{V}_{E\times B} + n\mathbf{V}_{mag}\right) - \nabla_{||}\left(n_e v_{||e}\right) + \nabla \cdot \left(D_n \nabla_\perp n\right) \\ + S_n - S \end{aligned} \tag{2.11}$$

$$\begin{aligned} \frac{3}{2}\frac{\partial p_e}{\partial t} = -\nabla \cdot \left(\frac{3}{2}p_e\mathbf{V}_{E\times B} + p_e\frac{5}{2}\mathbf{V}_{mag}\right) - p_e\nabla\cdot\mathbf{V}_{E\times B} \\ -\frac{5}{2}\nabla_{||}\left(p_e v_{||e}\right) + v_{||e}\partial_{||}p_e + \nabla_{||}\left(\kappa_{e||}\partial_{||}T_e\right) \\ +0.71\nabla_{||}\left(T_e j_{||}\right) - 0.71 j_{||}\partial_{||}T_e + \frac{\nu}{n}j_{||}\left(j_{||} - j_{||0}\right) \\ +\nabla\cdot\left(\frac{3}{2}D_n T_e \nabla_\perp n\right) + \nabla\cdot\left(\chi n \nabla_\perp T_e\right) + S_p - Q \end{aligned} \tag{2.12}$$

$$\begin{aligned} \frac{\partial \omega}{\partial t} = \begin{cases} -\nabla\cdot\left(\omega\mathbf{V}_{E\times B}\right) & \text{[Boussinesq]} \\ -\nabla\cdot\left[\frac{1}{2}\left(\omega + \frac{n}{B}\nabla_\perp^2\phi\right)\frac{\mathbf{b}\times\nabla\phi}{B}\right] + \nabla_\perp\cdot\left(\frac{1}{2}\frac{\partial n_i}{\partial t}\frac{1}{B^2}\nabla_\perp\phi\right) \end{cases} \\ +\nabla_{||}j_{||} - \nabla\cdot\left(n\mathbf{V}_{mag}\right) + \nabla\cdot\left(\mu_i\nabla_\perp\omega\right) \end{aligned} \tag{2.13}$$

$$\begin{aligned} \frac{\partial}{\partial t}\left(n v_{||i}\right) = -\nabla\cdot\left[n v_{||i}\left(\mathbf{V}_{E\times B} + \mathbf{b}v_{||i}\right)\right] - \partial_{||}p_e \\ +\nabla\cdot\left(D_n v_{||i}\nabla_\perp n\right) - F \end{aligned} \tag{2.14}$$

$$\begin{aligned} \frac{\partial}{\partial t}\left[\frac{m_e}{m_i}\left(v_{||e} - v_{||i}\right) + \frac{1}{2}\beta_e\psi\right] = \nu j_{||}/n_e + \partial_{||}\phi - \frac{1}{n_e}\partial_{||}p_e - 0.71\partial_{||}T_e \\ +\frac{m_e}{m_i}\left(\mathbf{V}_{E\times B} + \mathbf{b}v_{||i}\right)\cdot\nabla\left(v_{||i} - v_{||e}\right) \end{aligned} \tag{2.15}$$

where the S_n, S_p, Q and F are the external density, pressure , thermal and force sources. The parallel current $j_{||} = \nabla_\perp^2\psi$, The value of parallel electron thermal conduction coefficient in this model is given by $\kappa_{||e} = 3.2 n_e v_{th,e}^2 \tau_e$, where $v_{th,e}$ is electron thermal speed and τ_e is the electron collision rate. The resistivity is used as $\nu = (1.96\tau_e m_i/m_e)^{-1}$, $D_\perp$ and $\chi_\perp$ represent anomalous particle and thermal diffusivities coefficients. Derivative notations are have the following definition:

$$\partial_{||}f \equiv \mathbf{b}\cdot\nabla f \qquad \nabla_{||}f \equiv \nabla\cdot(\mathbf{b}f) \tag{2.16}$$

the definitions of E×B and dia-magnetic drifts are:

$$\mathbf{V}_{E\times B} = \frac{\mathbf{b}\times\nabla\phi}{B} \qquad \mathbf{V}_{mag} = -T_e\nabla\times\frac{\mathbf{b}}{B} \tag{2.17}$$

For the approximation of Boussinesq (with assuming spatial derivative of density is zero in vorticity equation), vorticity can be also written as:

$$\omega \simeq \nabla \cdot \left(\frac{1}{B^2} \nabla_\perp \phi \right) \tag{2.18}$$

Compared to other BOUT++ model, Hermes is a fully non-linear code that can simulate parallel asymmetric cases for turbulence including GAM and ZF(will be discussed in Chapter 4). New solvers and operators, especially for the calculations of petential ϕ and $\mathbf{E} \times \mathbf{B}$ flows are also developed to improve the numerical accuracy. The Hermes code makes it possible to simulate local and global flux-driven transport or MHD instability self-consistently driven by density and potential turbulence.

In this thesis, the Hermes and Elm-pb model (will be introduced in chapter 3) are the main codes in simulation work. Hermes is a 5 field double fluid model focusing the edge turbulence and transport. While Elm-pb mainly studies the edge MHD instabilities based on shear-Alfven's law. Compared to the Elm-pb mode, Hermes can study physics in the low toroidal mode number n. Since the Elm-pb model is derived assuming the flute ordering[89], which fails for low n modes. This is particularly obvious in the Laplacian inversion, plasma potential is calculated from Eq.(2.18) using Laplacian inversion[90], parallel derivatives are neglected in the elm-pb and other old version BOUT++ models. Especially for n=0, the Laplacian inversion causes great numerical errors in elm-pb and other old versions BOUT++ code. Also, more operators are developed for Hermes code specified in Parallel derivatives, which makes it possible to study asymmetric problems.

Chapter 3

The study of coupling effects of peeling-ballooning mode and Kink-ballooning mode

In this chapter, the theories about ballooning, peeling and kink modes are reviewed. In particular, for the operation of ITER, ELM studies are a very important topic[91]. A predictive understanding of the onset of type-1 ELMs has been gained via the development of the peeling ballooning model[31], in which ELMs are triggered by instabilities driven by the large pressure gradient (ballooning) and bootstrap current (peeling) in the edge of the plasma. However, studies of peeling modes in the presence of an X-point [29] indicate that peeling modes can occur, but that its growth rate is arbitrarily small in the presence of a separatrix[29]. However, that paper does not address the question of what happens with a separatrix. Instead it studies whether high-n kink modes can occur in the pedestal, and their properties in simple geometries without X-points. Analytic work by Wang[92] et al proposed that kink instabilities can occur with high toroidal mode numbers in the pedestal, triggering ELMs[92]. His work also indicates that kink modes in the pedestal depend on the current shape instead of the geometry of separatrix. Following his work, we study the kink-ballooning mode plasma instability, which is driven by internal current close to the plasma boundary and pressure gradient. The kink mode criteria of plasma current profile is investigated. Caltrans-Corsica was then used to regenerate the equilibrium, keeping the pressure constant whilst varying current profiles. Using the BOUT++3-field elm-pb code, then we obtain the growth rates and mode structures of kink-ballooning mode. We find that the kink-ballooning mode has smaller poloidal resonant mode numbers and lower growth rates at low toroidal mode numbers compared to peeling-ballooning mode. The main findings of this chapter indicate that the current-driven (peeling) components of the peeling-ballooning mode are sensitive to resonances outside the plasma. This makes it sensitive to the separatrix and resistivity in the SOL. In contrast, kink modes can in some circumstances be unstable in the pedestal, which are not sensitive to external resonances or conditions outside the plasma edge, implying that kink-ballooning modes may drive ELMs in some peeling-ballooning stable regions.

3.1 Ballooning, kink and peeling mode

As reviewed in the previous chapter, most existing theories propose that the ELM instability is related to two modes: the ballooning mode [93]- a kind of interchange instability driven by the pressure gradient, which can be stabilized by current gradient ; and the peeling mode[94], which is a current-driven external kink instability in the boundary. It is believed that the coupling between the peeling and ballooning modes makes the plasma exceed the stability threshold, triggering the ELM and the crash of pedestal profiles. As shown in Figure.3.1, the operating profiles of pressure gradient plasma current are limited in a narrow region by the peeling-ballooning mode.

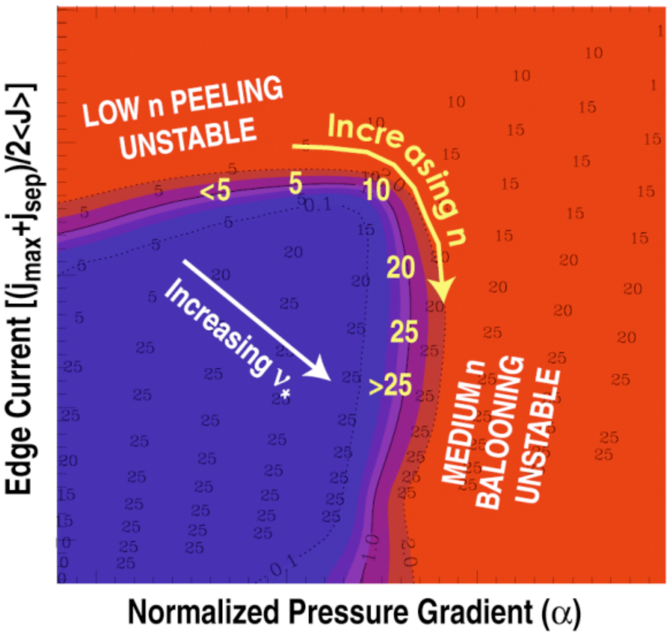

Figure 3.1: Stable operating region of peeling-balloon mode in pressure gradient and edge current space.

[95]

Besides the peeling-ballooning mode, Manickam [94] proposed that the ideal kink mode can trigger ELMs. They studied this linear mode using a series of ideal current and pressure profiles, neglecting the plasma resistivity. In those cases, it was found that the instability of the kink mode is mainly determined by the edge current density and stabilized by the shear of the plasma current. Thus, a similar conclusion can be given that the enhanced edge current density will make the kink mode unstable. In a finite pressure plasma, this mode can lead to two outcomes: exciting an ELM or extend into the plasma core region with a relatively wide radial dimension. Therefore, it is still necessary to look into the mechanism of ELMs, focusing on the relationships between ballooning, peeling and kink mode. Before exploring their coupling effects, basic theories of these modes are reviewed.

3.1.1 Ideal MHD equation and Energy principle

As mentioned in the first chapter, unstable ideal MHD modes are often dangerous for the plasma[89]. In order to avoid them, the main equations to study the characters of fluid plasma are the combination of the ideal MHD equation with Maxwell equations.[4]:

$$\text{Continuity Equation}: \frac{d\rho}{dt} + \rho\nabla\cdot\mathbf{v} = 0 \tag{3.1}$$

$$\text{Momentum Equation}: \rho\frac{d\mathbf{v}}{dt} = \mathbf{J}\times\mathbf{B} - \nabla p \tag{3.2}$$

$$\text{Energy Conservation Equation}: \frac{dp}{dt} + \gamma p\nabla\cdot\mathbf{v} = 0 \tag{3.3}$$

$$\text{Faraday}'\text{s Law}: \frac{\partial\mathbf{B}}{\partial t} = \nabla\times(\mathbf{v}\times\mathbf{B}) \tag{3.4}$$

$$\text{Ampere}'\text{s Law}: \nabla\times\mathbf{B} = \mu_0\mathbf{J} \tag{3.5}$$

$$\nabla\cdot\mathbf{B} = 0 \tag{3.6}$$

Where ρ is the plasma density , $\mathbf{v}$ is the plasma velocity, $\mathbf{B}$ and $\mathbf{J}$ are magnetic field and plasma current respectively, and the time derivative operator is defined as $\frac{d}{dt} = \frac{\partial}{\partial t} + \mathbf{v}\cdot\nabla$. These forms of the ideal MHD equations make several assumptions: 1) quasi-neutrality $n_i = n_e$, 2) the typical length scales are much larger than Larmor radius, 3) the frequencies of interest should be much smaller than the ion cyclotron frequency, 4) electron inertia (m_e) and hall effect ($\mathbf{j}\times\mathbf{B}$ term in Ohm's law) are neglected, 5) high collision rate, no dissipation and no trapped particles(no neoclassical effects), 6) displacement current is also set to zero in Maxwell equations.

However, these equations are not so “simple” in analytic study of plasma stability when including boundary conditions. Therefore, a simple method is required to avoid instability without studying the details of plasma self-destruction.

In that situation, the energy principle was proposed from the perspective of energy, which is a powerful method for testing ideal MHD stability in arbitrary 3D magnetic confinement configurations. The energy principle is applicable to linear stability analysis. To obtain expressions of a system, one should linearize all quantities of interest in their equilibrium values[4]:

$$q(\mathbf{r},t) = q_0(\mathbf{r}) + \widetilde{q_1}(\mathbf{r},t) \tag{3.7}$$

$$\widetilde{q_1}(\mathbf{r},t) = q_1(\mathbf{r})e^{-i\omega t} \tag{3.8}$$

where q represents each variable in the equations. ω is the frequency of variable's eigenmode. And we can also introduce the plasma displacement vector $\widetilde{\boldsymbol{\xi}}$ defined as $\widetilde{\mathbf{v_1}} = \frac{\partial \widetilde{\boldsymbol{\xi}}}{\partial t}$.

Setting the initial conditions of perturbed variables to zero, one can obtain the linearized expressions for the ideal MHD equation[96]:

$$\text{Continuity}: \ \widetilde{\rho_1} = -\nabla \cdot \rho_0 \widetilde{\boldsymbol{\xi}} \tag{3.9}$$

$$\text{Momentum}: \mathbf{F}(\widetilde{\boldsymbol{\xi}}) = \mathbf{J_1} \times \mathbf{B_0} + \mathbf{J_0} \times \mathbf{B_1} + \nabla \left(\widetilde{\boldsymbol{\xi}} \cdot \nabla P_0 + \gamma p_0 \nabla \cdot \widetilde{\boldsymbol{\xi}} \right) \tag{3.10}$$

$$\text{Energy Conservation Equation}: \widetilde{p_1} = \widetilde{\boldsymbol{\xi}} \cdot \nabla P_0 + \gamma p_0 \nabla \cdot \widetilde{\boldsymbol{\xi}} \tag{3.11}$$

$$\text{Faraday's Law}: \mathbf{B_1} = \nabla \times (\widetilde{\boldsymbol{\xi}} \times \mathbf{B_0}) \tag{3.12}$$

$$\text{Ampere's Law}: \mu_0 \widetilde{\mathbf{J_1}} = \nabla \times (\nabla \times (\widetilde{\boldsymbol{\xi}} \times \mathbf{B_0})) \tag{3.13}$$

Where $\mathbf{F}(\widetilde{\boldsymbol{\xi}})$ is the force acting on plasma due to virtual displacement. Using the variational principle, one can obtain an intuitive expression of energy principle after some manipulation[4]:

$$\begin{aligned} \delta W_P = \frac{1}{2} \int dV \times [\frac{|B_1|^2}{\mu_0} \ & \text{Field-line bending} \geq 0 \\ + \frac{B_0^2}{\mu_0} |\nabla \cdot \boldsymbol{\xi}_\perp + 2\xi_\perp| \ & \text{Magnetic compression} \geq 0 \\ + \gamma p_0 |\nabla \cdot \boldsymbol{\xi}|^{\mathbf{2}} \ & \text{Plasma Compression} \geq 0 \\ -2 \left(\boldsymbol{\xi}_\perp \cdot \nabla p \right) \left(\kappa \cdot \boldsymbol{\xi}_\perp^* \right) \ & \text{Pressure drive, + or -} \\ -\mathbf{B_1} \cdot \left(\boldsymbol{\xi}_\perp \times \mathbf{b} \right) j_{||}] \ & \text{Parallel current drive, + or -} \end{aligned} \tag{3.14}$$

From the expressions in the above equation, the first three terms are never less than zero, that means they stabilize the plasma.[10] However, the last two terms can be negative and become the source to drive instabilities.

In those terms of Eq. 3.14, $\frac{|B_1|^2}{\mu_0}$ is the energy which goes into bending field-lines. The perturbed magnetic field $\mathbf{B_1}$ is given by

$$\mathbf{B_1} = \nabla \times (\boldsymbol{\xi_1} \times \mathbf{B}).$$

In the second term, $\kappa = \mathbf{b} \cdot \nabla \mathbf{b}$ is magnetic field line curvature. The term $\gamma p_0 |\nabla \cdot \xi|^2$ represents compression of plasma, its value is zero for an incompressible fluid . The last two terms of Eq. 3.14 can be destabilizing when they are less than zero. Instabilities driven by these terms are often called pressure-driven and current-driven modes respectively. Pressure-driven instabilities include interchange modes(eg. ballooning mode), whilst external kink (peeling) and internal kink modes are current-driven instabilities. These instabilities are considered as the cause of ELMs[89] instabilities.

3.1.2 Ballooning mode

In the Tokamak magnetic configuration, the magnetic field strength decreases with the major radius, so the magnetic pressure gradient (also known as magnetic pressure force $P_B = \frac{B^2}{2\mu_0)}$) is always inwards major radius. The plasma pressure gradient is always in the minor radius. This radial asymmetry causes the curvature of the magnetic field to be divided into “good curvature” and “bad curvature” regions (shown in Figure.3.2). Assuming an initial disturbance of a flux surface, the plasma is shifted outward, thus makes the magnetic field weaker in the LFS. In the ”bad curvature” side (LFS), the weakening of the magnetic field is accompanied by a reduction of the magnetic tension and magnetic pressure. This further exacerbates the imbalance between magnetic and plasma pressure. The greater the disturbance, the smaller the resistance force from the field, which makes this instability grow. On the HFS, the oscillations are suppressed due to the enhancement of the magnetic field HFS strength the stabilizing effect of ”good curvature”.

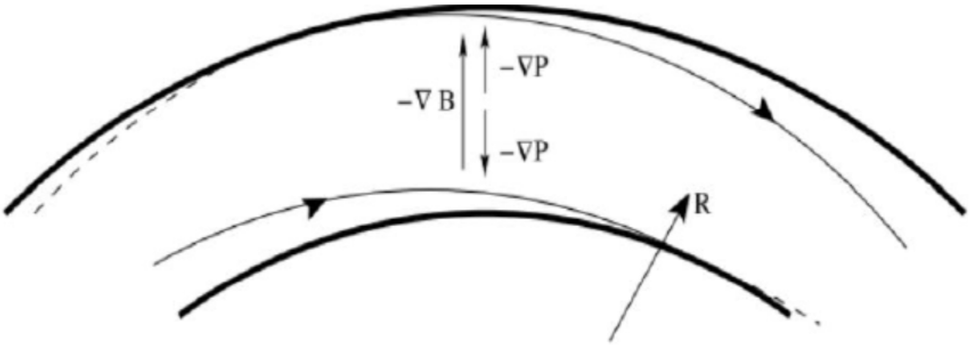

Figure 3.2: Relationship between magnetic pressure and dynamic pressure in tokamak.

[91]

In a further theoretical analysis, the one-dimension ballooning mode equation is derived from energy principle[93]:

$$\frac{d}{d\eta}\Big[1 + (s\eta - \alpha sin\eta)^2\Big]\frac{dF}{d\eta} + \alpha\Big[cos\eta + sin\eta(s\eta - \alpha sin\eta)\Big]F = 0. \tag{3.15}$$

Where F is function of energy, η is defined as the ballooning angle θ by Fourier and ballooning transformation:

$$F(\theta, x) = \sum_m e^{-im\theta} \int_{\infty}^{+\infty} e^{im\theta} F(\eta, x) d\eta \tag{3.16}$$

The magnetic shear and pressure gradients are expressed as two dimensionless quantities s and α respectively. The relationship between those two parameters are expressed as [31]:

$$\begin{aligned} s &= \frac{r}{q}\frac{dq}{dr} \\ \alpha &= -\frac{2\mu_0 R q^2}{B^2}\frac{dp}{dr} \end{aligned} \tag{3.17}$$

Where R and r are major and minor radius respectively, p is pressure and q is safety factor. Qualitative analysis indicates that the balloon mode has a stable space at high magnetic shear and low pressure gradient. For a circular cross-section plasma, the stable region of the ballooning model can be obtained in the $s-\alpha$ space, shown in Figure.3.3. Consistent with qualitative understanding, as the pressure gradient increases, the plasma becomes more unstable, requiring stronger magnetic shear to stabilize the plasma. Since the magnetic shear is the measure of the magnetic field, the distance between field lines grows with magnetic shear, thus the instabilities can not entire localized on the unfavorable side, resulting in destabilizing energy reduced. On the other hand, low shear allows mode structures to keep almost the same on adjacent field lines, the increasing magnetic shear can prevent the fast growth of ballooning instability in the radial direction.

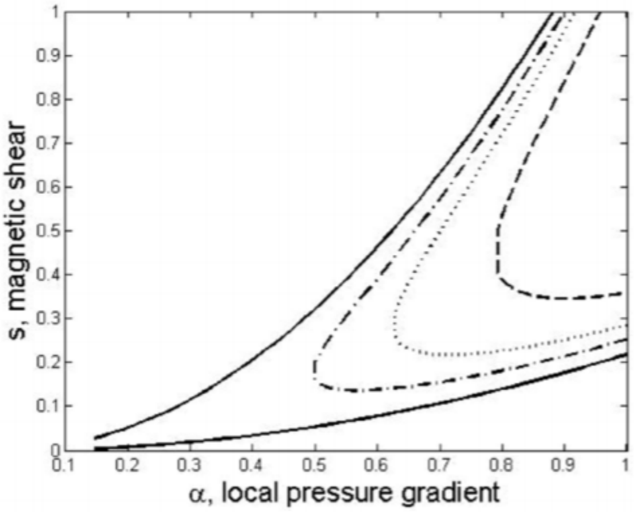

FIGURE 3.3: The $s-\alpha$ stability diagram for different aspect ratios, the space enclosed by different curves are the ballooning instability regions for different aspect ratios($\epsilon = a/R_0$) respectively. The solid line shows $\epsilon = 0$, the dash-dot line $\epsilon = 0.025$, the dotted line $\epsilon = 0.05$ and the dashed line $\epsilon = 0.1$ when q = 3. [97]

At fixed shear s, when α is small, the ballooning mode is stable (first stable zone); when the pressure gradient parameter α increases, the ballooning mode will become unstable. When α continues to increase, the ballooning mode changes back to stability and enters the so-called second stable zone. The stable space of the ideal ballooning mode is in the upper left part of Figure.3.3 , which is the working space for most tokamaks. However, there is also a second stable region in the case of higher pressure. This region also has a high β, the reason for stabilization is that the local shear is negative. The possible existence of the second stable zone is good news for future high-parameter operation, but further testing is still needed [91]. Unfortunately, it is quite hard to access to the second instability for circular plasmas [98], but when the plasma is shaped, theoretical work proved that the increased elongation and triangularity can access to the second stable region[99]. Nevertheless, there has been a long debate about second instability. It may be closed by kink/peeling modes. Experiments on DIII-D [100]and C-MOD[101] report the existence of "Super-H-mode", with higher density and pressure operation than standard H-Mode operation. Theoretically, a model named EPED[102], with the hypothesis that multi-mechanisms contribute to the forming of H mode, including kinetic ballooning mode(KBM) and P-B mode, predicts the H-mode and Super-H-mode performance regions in pedestal(mainly pedestal height and width). The calculation results come to good agreements with some experiments[103]. The EPED model also indicates and proves that shaping effects play a very important role in accessing Super-H-mode. The strongly shaped plasma can not only stabilize the ballooning mode, but decouple peeling and ballooning instability[100]. Therefore, although the shaping effects on ELMs are not this thesis, it will be studied in future work.

3.1.3 Kink and peeling mode

The last term of Eq.3.14 illustrates that plasma current can lead to ideal MHD instabilities. This kind of instability was first observed in the ZETA (The Zero Energy Toroidal Assembly, at Harwell, UK) magnetic confinement device in the year of 1957[104]. This instability had been predicted theoretically and is driven by the plasma current[105].

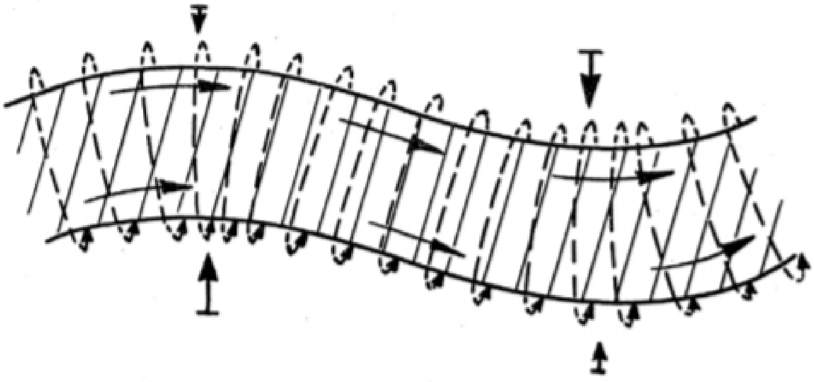

Figure 3.4: Displacements induced by the plasma current profile. [9]

Due to the current profile and gradient, the magnetic field is compressed in some places and expanded in others, which makes a small displacement begins to develop in a column. The magnetic forces on the inside of the kink become larger than those on the outside (shown in 3.4). At the same time, the magnetic field pressure acts to enhance the motion, leading to the growth of the perturbation. This kind of original perturbation is harmonic in the poloidal direction, which makes field ”twist” along the axis. Figure.3.5 shows the perturbations of the field for different poloidal modes.

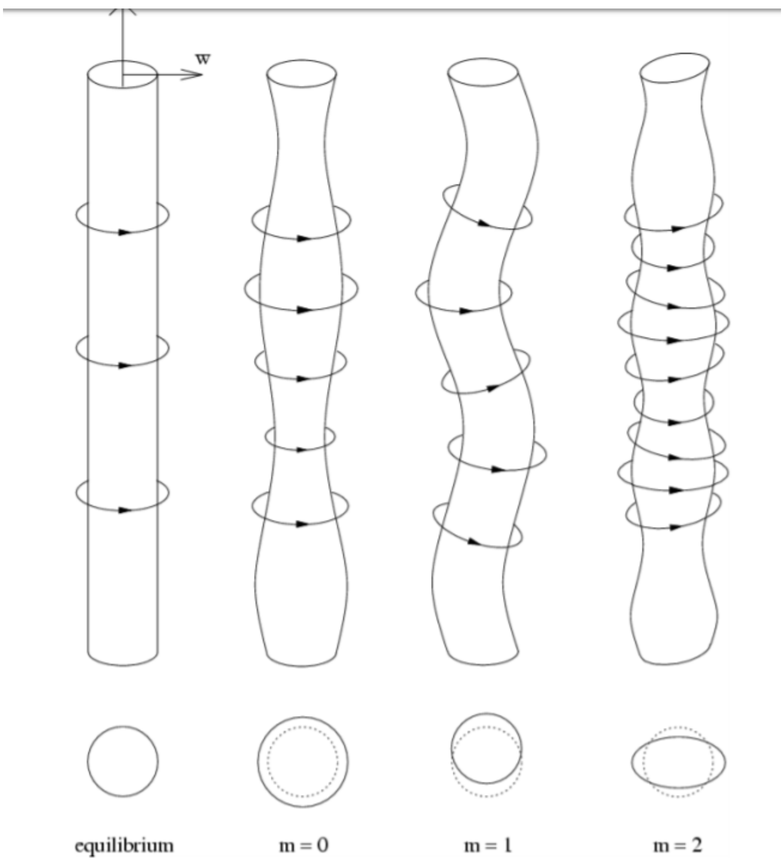

FIGURE 3.5: Displacements induced by the plasma current profile. Re-created by author from paper[10]

Generally, kink modes are divided into internal kink modes and external kink modes[10]. Internal kink modes are typically thought to occur in the case of n=1,m=1. In the 1970s, Shafranov[106] and Rosenbluth[107] studied the internal kink mode in cylindrical configurations. They found the ideal internal kink mode is stable when

$$q(0) > 1 \tag{3.18}$$

where $q(0)$ is the value of safety factor on the axis. Following their work, Bussac et al. theoretically analyzed the kink instability in a circular cross-section tokamak, he found that the internal kink mode is stable for sufficiently low β_p. Edery[108] then studied the effect of cross-sectional deformation on the internal kink mode, the analytical result indicates that cylindrical distortions play stabilizing (m=3,4 distortions) and destabilizing(m=2 distortion) role when the symmetries of cylindrical pinch are lost.

In a circular cross-section tokamak with the large aspect ratio assumption. The variation of the plasma energy can be written as[109]:

$$\delta W = (1 - \frac{1}{n^2})\delta W_c + \frac{1}{n^2}\delta W_T \tag{3.19}$$

Where δW_c is the potential energy change under the cylindrical configuration, δW_T corresponds to the contribution of the toroidal effect. For a parabolic safety factor distribution, the corresponding dimensionless potential energy is

$$\widetilde{\delta W_T} = 3(1 - q_0)(\frac{13}{144} - \beta_{p1}^2) \tag{3.20}$$

Where $\beta_{p1} = [\int_0^{r_1}(p - p_1)2rdr]/[(B_{\theta 1}^2/2\mu_0)r_1^2]$,$p_1 = p(r_1)$, $B_{\theta 1} = (r_1/R)B_\theta$, r_1 is the minor radius of q=1. Noticing that change of potential energy could be positive even if $q_0 < 1, \beta_p^2 > 13/144$. For monotonic q profile, the region $r > r_1$ can also keep stable, that means internal kink instability general occurs in core region. After minimizing the energy expression, the growth rate of the ideal internal kink instability with toroidal effects is[110]:

$$\frac{\gamma}{\omega_A} = -\frac{1}{r_1 q'}\frac{\pi}{\sqrt{3}}\frac{r_1^2}{R^2}\widetilde{\delta W_T} \tag{3.21}$$

Here $q' = (dq/dr)_{r_1}$, $\omega_A = v_A/R$, v_A is the Alfven velocity. In the large aspect ration assumption, internal kink instabilities are believed to happen when $q < 1$, this criteria is also named Kruskal-Shafranov limit.

Hastie argued that the ideal internal kink mode can be unstable when $q > 1$[110], so that internal kink instabilities do not always happen at the m=1,n=1 surface. The previous works are based on ideal MHD. Since the plasma has resistivity, in 1976, Coppi studied resistive kink instability and include the effects of plasma resistivity[111]. Then Hastie systematically reviewed the effect of resistance on the internal kink instability. In his paper, the growth rate of internal the kink mode was written as:

$$\gamma\tau_H = -\delta W_H \left[\frac{1}{8}\left(\frac{\gamma}{\gamma_{\gamma_\eta}}\right)^{9/4} \frac{\Gamma\left(\frac{(\gamma/\gamma_\eta)^{3/2}-1}{4}\right)}{\Gamma\left(\frac{(\gamma/\gamma_\eta)^{3/2}+5}{4}\right)}\right] \tag{3.22}$$

$$\gamma_\eta = \tau_H^{-2/3}\tau_R^{-1/3} \tag{3.23}$$

Where $\tau_H = \left[\sqrt{\mu_0\rho}/(B_\theta q^{'})\right]_{q=1}$, $\tau_R = (\mu_0 r^2/)_{q=1}$, τ_η is the growth rate of resistive internal kink mode. Γ is the gamma function. In the ideal MHD limit, $\tau_R \to \infty$, $\gamma = -\delta W_H/\tau_H$, and the growth rate is the same as the ideal internal kink mode. When $\gamma W_H \to 0$, $\gamma = \gamma_\eta$. When $\delta W_H > 0$, the kink mode is stable and the growth rate becomes the m=1 tearing mode. Figure.3.6 shows how the m = 1 mode growth rate varies with δW, showing that plasma resistivity helps to stabilize the kink instability.

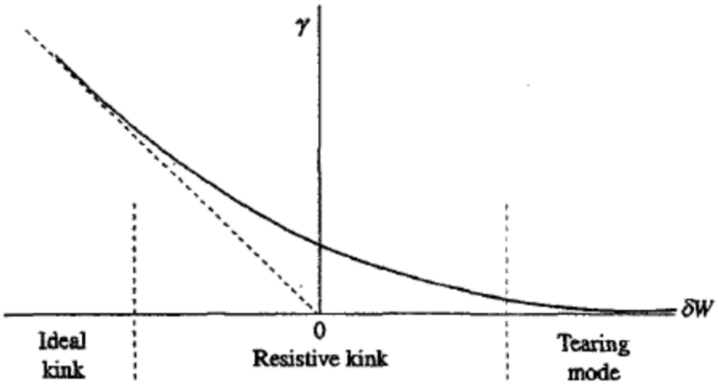

FIGURE 3.6: The m = 1 mode growth rate various with δW_H. When δW_H changes from negative to positive, the internal kink mode transforms to resistive kink mode and tearing mode .

[4]

Besides the instability driven by the current and current gradient in the core region, kink modes can also be triggered by boundary current, named the external kink mode. The edge current does not always have a destabilizing effect on the external kink mode, and bad curvature can enhance the distortion of this mode. Since the distortion driven by edge current makes the resonant surface "peel" from the core plasma, the external kink mode is also called the "peeling mode", meaning a mode driven by parallel currents, which requires the boundary of the plasma to move, driven unstable by a finite current density at the plasma boundary[112]. More recently, the term peeling mode has also been used, in a more general sense, to describe external kink modes that are strongly localized at the edge of the plasma, driven unstable either by a finite current density or a finite current gradient at the plasma edge[113]. In the rest of this thesis, we will refer to internal kink modes as “kink modes” and external kink modes as “peeling modes”. The mechanism of the peeling mode is quite similar to the kink mode, it is thought to happen at $m > 1$, and unstable modes are aligned with the magnetic field (resonant) just outside the plasma edge. In the large aspect ratio and free boundary assumption, kink and peeling modes are often studied using the same methods[112] but using different current profiles:

$$\begin{aligned} j &= j_0(1-(r/a)^2)^{\upsilon} \\ \upsilon &= q_a/q_0 \end{aligned} \tag{3.24}$$

j_0 and q_0 are the plasma current and safety factor in the core plasma region, a is the minor radius of the plasma boundary.

The research reviewed above is theoretical analyses that did not consider data from experiments. In 1984, Troyon used the ERATO code to study the peeling mode and found that there is a limit to the normalized β_N that can be obtained in the Tokamak device without considering a resistive wall[114]. His work revealed that there is a limit in normalized β, where $\beta = \beta_N(aB_T/I)$, and this limit is around 2.8, which is now known as the Troyon limit. Ten years later, the world’s major tokamak devices have verified the existence of the Troyon limit[115, 116]. Wesson then summarized the conditions for kink and peeling instabilities with different q profile and current profile[10].

Different from kink mode, wall effects have a great influence on the peeling mode, requiring the wall is close enough to the plasma. As shown in Figure.3.7, if there is no wall (the wall is far away) then the flux-surface perturbation goes like $\delta\psi \approx r^{-m}$. An ideal wall is a superconductor that forces the perturbation to zero at the boundary. This corresponds to a current sheet which pushes back on the mode. In real machines, the vessel walls always have some finite resistivity. The current and hence radial magnetic field can diffuse into the wall. We can conclude that conductivity has an important effect on the peeling mode.

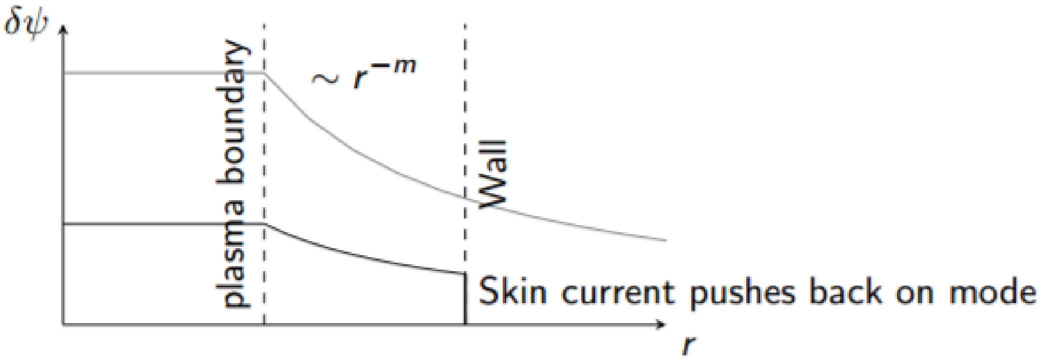

FIGURE 3.7: The change of potential with and without wall effects. [10]

In later studies, it was found that the peeling mode plays an important role on ELMs[91]. A predictive understanding of the onset of type-1 ELMs has been gained via the development of the peeling ballooning model[91], in which ELMs are triggered by instabilities driven by the large pressure gradient (ballooning) and bootstrap current (peeling) in the edge of the plasma. For general axisymmetric toroidal geometry without Grad-Shafnov shift, this peeling mode stability condition is[91]:

$$\sqrt{1-4D_M} > 1 + \frac{1}{\pi q'} \oint \frac{j_{||}B}{R^2 B_p^3} dl \tag{3.25}$$

where D_M is the Mercier index, defined as

$$D_M = -\mu_0 \frac{2r}{B^2} \frac{1}{s^2} \frac{dp}{dr} (1-q^2) \tag{3.26}$$

where s is magnetic shear defined in Eq.3.3, $j_{||}$ is the current density parallel to the magnetic field B, R is the major radius, B_p is the poloidal magnetic field strength, dl is a poloidal arc length element on a flux surface.

From the above discussion in this section, we can summarize that both kink and peeling mode are edge current-driven instablities. Then a question is raised: can kink mode also trigger ELMs as peeling mode? This question will be studied in the rest part of this chapter.

3.1.4 The effects of X-points

As mentioned in subsection 1.1.2, the majority tokamak operates in divertor configuration with X-point and double X-points, which is recognized to play a role in the formation of transport barrier[117], turbulence mitigation[118] and ELM stabilization[119]. Specifically, in the studies of edge stability, X-point geometry is verified to take a major effect in the ELM simulation work. Huysmans finds that X-point can stabilize peeling mode greatly utilizing CASTOR code[25], with setting edge current zero. Saarelma's work reveals that the magnetic shear in the vicinity of X-point can stabilize peeling mode using ELITE[119]. His simulation results also suggest the locations of X-point takes effects on ballooning mode: X-points on low field side can destabilize ballooning mode, while X-points on high field side has a little improvement on stability. Webster also indicates that peeling modes can occur, but that its growth rate can be arbitrarily small in the presence of a separatrix[29]. Further, Analytic work by Wang et al proposed that kink instabilities can occur with high toroidal mode numbers in the pedestal, triggering ELMs[92]. However, this paper does not address the question of what happens with a separatrix. Instead, it addresses whether high-n kink modes can occur in the pedestal and their properties in simple geometries without X-points. His work also indicates that kink modes in the pedestal rely on the current shape rather than the geometry of the separatrix. Under that condition, we aim to verify that whether the kink like instability can drive the ELM crash and the existence of kink-ballooning mode numerically.

However, as discussed in subsection 2.1.2, BOUT++ simulations of geometry with X-points physics are still susceptible to numerical instabilities. Since the grid points are strongly packed near the X-point in the vicinity of separatrix, but not on surfaces deeper inside the plasma [119] in straight filed line coordinate system. The coordinate system has a singularity near the X-point and separatrix. This is particularly a problem for the coordinate system mostly used in BOUT/BOUT++, which aligns the parallel direction to the poloidal angle. It even harder to simulate X-point geometry modified by CORSICA. Large numerical instabilities seems inevitable even high-resolution was applied(516×256). Therefore, we only present the work in circular tokamak geometry in this chapter.

3.2 MHD model for ELMs

3.2.1 Plasma moments and MHD equations

The time evolution of the plasma distribution function is well described by the collisional Vlasov equation[120]:

$$\frac{\partial f_\alpha}{\partial t} + \mathbf{v} \cdot \nabla f_\alpha + \frac{e_\alpha}{m_\alpha}(\mathbf{E} + \mathbf{v} \times \mathbf{B}) \cdot \frac{\partial f_\alpha}{\partial \mathbf{v}} = C_\alpha(f_\alpha). \tag{3.27}$$

Where $f_\alpha(\mathbf{x}, \mathbf{v}, t)$ represents the distribution function, α is the species of particles, the term on right of the equality is the collision operator. The electric and magnetic field can be written as:

$$\nabla \cdot \mathbf{E}(\mathbf{x}, t) = \frac{1}{\epsilon_0} e_\alpha \iiint f_\alpha(\mathbf{x}, \mathbf{v}, t) d^3 v \tag{3.28}$$

$$\nabla \cdot \mathbf{B}(\mathbf{x}, t) = 0 \tag{3.29}$$

$$\nabla \times \mathbf{E}(\mathbf{x}, t) = -\frac{\partial \mathbf{B}(\mathbf{x}, t)}{\partial t} \tag{3.30}$$

$$\nabla \times \mathbf{B}(\mathbf{x}, t) = \mu_0 \left[\sum_{k=1} e_\alpha \iiint f_\alpha(\mathbf{x}, \mathbf{v}, t) d^3 v \right] + \mu_0 \epsilon_0 \frac{\partial \mathbf{E}(\mathbf{x}, t)}{\partial t} \tag{3.31}$$

where e_α is electric charge, ϵ_0 is vacuum permittivity and μ_0 is vacuum permeability. Using the distributions function, one can fully describe the plasma behavior. However, the Vlasov equations and Maxwells equations are the governing equations of the Vlasov-Maxwell system, which includes eight unknowns $(f_e, f_i, \mathbf{E}, \mathbf{B})$ and eight independent equations in a six-dimensional phase space. That makes it too complex to solve in most situations. Therefore, a practicable way is to integrate over the velocity spance in collisional Vlasov equation and obtain fluid equations[120].

Before introducing the fluid equations, we need to define plasma fluid variables. The number density of the αth species, is defined by

$$n_\alpha(\mathbf{x}, t) = \iiint f_a(\mathbf{x}, \mathbf{v}, t) d^3 v \tag{3.32}$$

The particle flux of the αth species is :

$$n_\alpha(\mathbf{x},t)\mathbf{V} = \iiint \mathbf{v} f_a(\mathbf{x},\mathbf{v},t)d^3v \tag{3.33}$$

The momentum flux of the αth species is:

$$m_\alpha n_\alpha \mathbf{V}_\alpha \mathbf{V}_\alpha + \mathbf{P}(\mathbf{x},t) = \iiint m_\alpha \mathbf{v}\mathbf{v} f_a(\mathbf{x},\mathbf{v},t)d^3v \tag{3.34}$$

where $\mathbf{P}(\mathbf{x},t)$ is the thermal pressure tensor:

$$\mathbf{P}(\mathbf{x},t) = \iiint m_\alpha[\mathbf{v}-\mathbf{V}_\alpha][\mathbf{v}-\mathbf{V}_\alpha] f_a(\mathbf{x},\mathbf{v},t)d^3v \tag{3.35}$$

Using these relations, one can apply the zero, first and second moments over the Eq.3.27 and obtain the fluid equations[121]:

the continuum equation,

$$\frac{\partial n_\alpha}{\partial t} + \nabla\cdot(n_\alpha \mathbf{V}_\alpha) = S^n_\alpha \tag{3.36}$$

the momentum conservation equation,

$$\begin{aligned}\frac{\partial m_\alpha n_\alpha \mathbf{V}_\alpha}{\partial t} + \nabla p_\alpha + \nabla\cdot(\overleftrightarrow{\pi} + m_\alpha n_\alpha \mathbf{V}_\alpha \mathbf{V}_\alpha) = \\ Z_\alpha e n_\alpha(\mathbf{E} + \mathbf{V}_\alpha \times \mathbf{B}) + \mathbf{S}^{\mathbf{m}}_\alpha\end{aligned} \tag{3.37}$$

and the energy conservation equation,

$$\begin{aligned}\frac{\partial}{\partial t}(\frac{3}{2}p_\alpha + \frac{1}{2}m_\alpha n_\alpha V^2_\alpha) + \nabla\cdot\mathbf{Q_j} = \\ W_\alpha + \mathbf{V}_\alpha\cdot(\mathbf{R}_\alpha) + S^E_\alpha\end{aligned} \tag{3.38}$$

where the $S^n_j, \mathbf{S^M_j}, S^e_j$ are density, momentum and energy sources for species α, respectively. The heat-flux tensor $\mathbf{Q}_\alpha(\mathbf{x},t)$ is a third rank tensor, which is defined by

$$\mathbf{Q}_\alpha(\mathbf{x},t) = \iiint m_\alpha[\mathbf{v}-\mathbf{V}_\alpha][\mathbf{v}-\mathbf{V}_\alpha][\mathbf{v}-\mathbf{V}_\alpha] f_a(\mathbf{x},\mathbf{v},t)d^3v \tag{3.39}$$

and the heat-flux vecctor $\mathbf{q}_\alpha(\mathbf{x},t)$ is defined by

$$\mathbf{q}_\alpha(\mathbf{x},t) = \iiint \frac{1}{2} m_\alpha [\mathbf{v}-\mathbf{V}_\alpha]\cdot[\mathbf{v}-\mathbf{V}_\alpha][\mathbf{v}-\mathbf{V}_\alpha] f_a(\mathbf{x},\mathbf{v},t) d^3v \tag{3.40}$$

These fluid equations of the αth species reduce the variables to 6 in 3-dimensional phase space. Since the main plasma mainly contains electron and ion species, this description is also named 2-fluid equations[4]. Since the mass of ions is much bigger than the electron, the ion's relaxation time is longer, we can merge the above fluid equations into single species ones:

$$\begin{aligned}
\textit{Continuity Equation}: \ & \frac{\partial \rho}{\partial t} + \nabla\cdot(\rho\mathbf{V}) = 0 && (3.41)\\
\textit{Momentum Equation}: \ & \rho\frac{\partial \mathbf{V}}{\partial t} + \nabla\cdot(\rho\mathbf{V}\mathbf{V}+\mathbf{P}) = \mathbf{J}\times\mathbf{B} && (3.42)\\
\textit{Energy Conservation Equation}: \ & \frac{3}{2}\left[\left(\frac{\partial}{\partial t}+\mathbf{V}\cdot\nabla\right)p\right] + \frac{3}{2}p(\nabla\cdot\mathbf{V}) = \\
& -\nabla\cdot\mathbf{q} + \mathbf{J}\cdot(\mathbf{E}+\mathbf{V}\times\mathbf{B}) && (3.43)
\end{aligned}$$

where the new variables are given below:

$$\begin{aligned}
\textit{Mass density } \rho &= n_e m_e + n_i m_i \\
\textit{Electric Current Density}: \ \mathbf{J} &= e_e n_e \mathbf{v_e} + e_i n_i \mathbf{v_i} \\
\textit{Veloctiy}: \ \mathbf{V} &= (m_i n_i \mathbf{v_i} + m_e n_e \mathbf{v_e})/\rho \\
\textit{Total Pressure}: \ p &= p_e + p_i
\end{aligned} \tag{3.44}$$

Eq.3.41 to Eq.3.43 are much simpler than kinetic and 2-fluid descriptions. Some terms in those equations can be simplified further in specific cases.

3.2.2 Shear Alfven law

Eq.3.41 to Eq.3.43 still have some high order closure terms (such as heat flux q) with complex terms, making analytic and simulation work difficult. In the quasi-neutral and adiabatic cases, most terms including heat flux and external electromagnetic waves can be cancelled (besides those in quasi-neutral phases, such as Alfven waves). The shear Alfven law is a useful starting point in the analysis of many common plasma instabilities, and is a fundamental part in the analysis which follows[89]. Assuming the density is constant, the single fluid momentum equation can be written as[4]:

$$\rho\frac{d\mathbf{V}}{dt}+\nabla\cdot\overleftrightarrow{\Pi}=-\nabla P+\mathbf{J}\times\mathbf{B} \tag{3.45}$$

with $\overleftrightarrow{\Pi}$ denotes the viscous tensor, and the usual convective derivative is:

$$\frac{d}{dt}=\frac{\partial}{\partial t}+\mathbf{V}\cdot\nabla$$

Taking the parallel component of the curl of this equation (i.e. apply $\mathbf{B}\cdot\nabla\times$ to each side)

$$\mathbf{B}\cdot\nabla\times\left[\rho\frac{dV}{dt}+\nabla\cdot\Pi\right]=\underbrace{-\mathbf{B}\cdot\nabla\times\nabla P}_{\Rightarrow 0}+\mathbf{B}\cdot\nabla\times(\mathbf{J}\times\mathbf{B}) \tag{3.46}$$

The $\mathbf{J}\times\mathbf{B}$ term can be written as:

$$\mathbf{B}\cdot\nabla\times(\mathbf{J}\times\mathbf{B})=\nabla\cdot[(\mathbf{J}\times\mathbf{B})\times\mathbf{B}]+(\mathbf{J}\times\mathbf{B})\cdot(\nabla\times\mathbf{B}) \tag{3.47}$$

making using of tensor identities and taking $\mathbf{b}\cdot\nabla\times$ of Eq.3.46, the shear Alfven Law can be derived[89]:

$$\mathbf{b}\cdot\nabla\times\mathbf{f}=B^2\mathbf{b}\cdot\nabla\left(\frac{J_{||}}{B}\right)+2\mathbf{b}\times\boldsymbol{\kappa}\cdot\mathbf{f}+2\mathbf{b}\times\boldsymbol{\kappa}\cdot\nabla P+\mathcal{O}(\kappa^2)$$

$$\mathbf{b}\cdot[\nabla\times\mathbf{f}-2\boldsymbol{\kappa}\times\mathbf{f}]=B^2\mathbf{b}\cdot\nabla\left(\frac{J_{||}}{B}\right)+2\mathbf{b}\times\boldsymbol{\kappa}\cdot\nabla P \tag{3.48}$$

where $\boldsymbol{\kappa}$ is magnetic field line curvature $\boldsymbol{\kappa}=(\mathbf{b}\cdot\nabla)\mathbf{b}$, the LHS side of this is primarily the parallel component of the vorticity $\nabla\times\mathbf{V}$, so this equation is often called the vorticity equation.

$$\begin{gathered}\boldsymbol{\kappa}=\frac{\mu_0}{B^2}(\mathbf{f}+\nabla P)+\frac{1}{B}\nabla_\perp B\\ \Rightarrow\nabla_\perp B^2=2B^2\boldsymbol{\kappa}-2\mu_0(\mathbf{f}+\nabla P)\end{gathered}$$

The shear Alfven's law makes it much easier to study kink and interchange instabilities, assuming parallel spatial frequency is much smaller than perpendicular one $k_{||} << k_{\perp}$.

3.2.3 Models for ELMs in BOUT++

Based on the shear-Alfven law and neglecting viscosity and parallel velocity term, Hazeltine and Meiss derived a reduced MHD equation suitable for the simulations of peeling-ballooning mode[89]:

$$\rho\frac{dU}{dt} = B^2\mathbf{b}\cdot\nabla\left(\frac{J_{||}}{B}\right) + 2\mathbf{b}\times\boldsymbol{\kappa}\cdot\nabla P \tag{3.49}$$

$$\frac{\partial\psi}{\partial t} = -\frac{1}{B_0}\nabla_{||}\phi \tag{3.50}$$

$$\frac{\partial P}{\partial t} = -\frac{1}{B_0}\mathbf{B}_0\times\nabla\phi\cdot\nabla P \tag{3.51}$$

$$U = \frac{1}{B_0}\nabla_{\perp}^2\phi \tag{3.52}$$

$$J_{||} = J_{||0} - \frac{1}{\mu_0}B_0\nabla_{\perp}^2\psi \tag{3.53}$$

Where U is the parallel component of fluid vorticity, perturbed vector potential $\psi = A_{||}/B_0$, ϕ is electrostatic potential. Linearizing those equations and making explicit the non-linear terms, we obtain the 3-field Elm-pb model which is solved using BOUT++[75]:

$$\frac{d\hat{\omega}}{d\hat{t}} = \hat{B}_0^3\mathbf{b}\cdot\hat{\nabla}\left(\frac{\hat{J}_{||}}{\hat{B}_0}\right) + 2\hat{B}_0\mathbf{b}_0\times\hat{\kappa}\cdot\hat{\nabla}\hat{P} \tag{3.54}$$

$$\frac{\partial\hat{A}_{||}}{\partial\hat{t}} = -\frac{1}{B_0}\nabla_{||}\hat{\phi} \tag{3.55}$$

$$\frac{\partial\hat{P}}{\partial\hat{t}} = -\frac{1}{\hat{B}_0}\mathbf{b}_0\times\hat{\nabla}\hat{\phi}\cdot\hat{\nabla}\hat{P} \tag{3.56}$$

$$\hat{\nabla}_{\perp}^2\hat{A}_{||} = -\frac{1}{2}\beta_x\frac{m_i}{m_e}\hat{J}_{||} \tag{3.57}$$

$$\hat{\nabla}_{\perp}^2\hat{\phi} = \frac{\hat{\omega}}{\hat{N}} \tag{3.58}$$

with the full parallel derivative

$$\mathbf{b}\cdot\hat{\nabla} = \mathbf{b}_0\cdot\hat{\nabla} - \frac{m_e}{m_i}\frac{1}{\hat{B}_0}\mathbf{b}_0\times\hat{\nabla}\hat{A}_{||}\cdot\hat{\nabla}$$

All the variables from Eq.3.54 to Eq.3.58 are normalized, evolving variables can be normalized using MHD-like normalization. The normalized factors are [75], a typical length scale $\overline{L}$, timescale $\overline{T}$ and magnetic field $\overline{B}$, related by $\overline{V_A}^2 = \overline{B}^2/\mu_0\rho m = \overline{L}^2/\overline{T}^2$. The normalized parameters are defined as: $\hat{t} = \frac{t}{\overline{T}}, \hat{B} = \frac{B}{\overline{B}}, \hat{\nabla} = \overline{L}\nabla, \hat{\kappa} = \overline{L}\kappa$. Evolving variables are then normalized as: $\hat{U} = \overline{T}U, \hat{\psi} = \frac{\psi}{\overline{L}}, \hat{P} = \frac{2\mu_0 P}{\overline{B}^2}$ and auxiliary variables have the following normalized form: $\hat{J}_{||} = -\frac{\mu_0\overline{L}}{B_0}J_{||}, \hat{\phi} = \frac{\phi}{\overline{V_A}\overline{L}B_0}$.

3.3 Simulations of kink-ballooning modes

As discussed in section 3.1, kink modes, or internal kink modes, are driven by the plasma current. Different from the peeling mode, the kink mode is driven by the current gradient and pressure gradient inside of the resonant surface. Also, the edge current does not always have a destabilizing effect on the kink mode.

Generally, peeling and kink modes are driven by the current gradient outside and inside the resonant surface separately. In previous work, authors have derived the criteria for peeling[31] and kink mode[92] in the pedestal. The simulation work here is based on these criteria to explore the ELM mechanism.

It is well recognized that the stability criteria of the peeling mode, in circular equilibria with large aspect ratio, can be written as [31]:

$$\alpha\left[\frac{r}{R}(1-\frac{1}{q^2}) + s\Delta' - f_t\frac{Rs}{2r}\right] > Rqs\left(\frac{j_{||}^{driven}}{B}\right) \tag{3.59}$$

Where Δ' is the gradient of the Shafranov shift, s refers to the magnetic shear, $\alpha = -\frac{2\mu_0 Rq^2}{B^2}\frac{dp}{dr}$ is related to the gradient of β, $j_{||}^{driven}$ is the externally driven current (usually boot-strap current). And f_t is the fraction of the trapped particles (since kinetic particle effects are ignored in the analysis, so this can be important). Meanwhile, the kink mode stability criterion in Hamada coordinates from the energy principle can be written as[92]:

$$
\begin{aligned}
\delta W = \int \frac{ada}{2R}\frac{\epsilon^2+1}{2\epsilon}\Big[\left(u^{'2} + \frac{(m+1)^2}{a^2}u^2\right) - Du^{'}\xi_m - D\frac{m+1}{a}u\xi_m \\
+\frac{(m+1)Ru^2}{\chi^{'}}\frac{2\epsilon}{\epsilon^2+1}\frac{\partial J^{'}}{a\partial a} - \left(g_{33}\frac{p\phi^{''}}{\phi^{'}} + \frac{p^{'2}}{\phi^{'2}}\xi_m^2\right)\Big] \qquad (3.60)
\end{aligned}
$$

In this equation, a is defined as an average minor radius $a = (V/2\pi^2 R)^{1/2}$, V is plasma volume, $g_{33} = R^2$ is the metric tensor in Hamada coordinates, $D = \frac{-2}{\iota\epsilon^{1/2}}\frac{p^{'}}{\phi^{'}}\frac{2\epsilon}{\epsilon^2+1}$, $\iota \approx 2\pi\frac{RB_p}{rB_t}$ is the rotational transform. Minimizing δW with respect to displacement u, the following can be derived:

$$
\begin{aligned}
\frac{d}{da}\left(a\frac{du}{da}\right) - \frac{(m+1)^2}{a}u + \frac{(m+1)Ru^2}{\chi^{'}}\frac{2\epsilon}{\epsilon^2+1}\frac{dj}{da} \\
= -\frac{d}{da}\left(\frac{aD\xi_m}{2}\right) + \frac{m+1}{2}D\xi_m \qquad (3.61)
\end{aligned}
$$

Integrating the equation across the boundary a_0, we get:

$$
\lambda = \frac{1 - 2(\frac{a_0}{b})^{2(m+1)} - dj[1-(\frac{a_0}{b})^{2(m+1)}]}{(\frac{a_0}{b})^{2(m+1)} + dj[1-(\frac{a_0}{b})^{2(m+1)}]} \qquad (3.62)
$$

where b is the position of the wall, λ is arbitrary parameter comes from the general solution of Eq.3.61, then following the steps in the paper[92], the criterion is obtained:

$$
\iota^2 < \frac{2}{\epsilon^2+1}\Big[1+\frac{\epsilon^2-1}{3\epsilon^2+1}\Big[\left(\frac{1}{2}+\frac{3}{2}\Delta\right) - 2\beta_p\left(\lambda\left(1-\frac{1+\lambda}{4}\right)+\frac{\epsilon^2-1}{3\epsilon^2+1}\right)\Big]\Big] \qquad (3.63)
$$

From this equation, the conditions for the kink to be stable are

$$
\lambda < \frac{3-\sqrt{9+4\Lambda}}{2},\ \lambda > \frac{3+\sqrt{9+4\Lambda}}{2} \qquad (3.64)
$$

where the expression for Λ is

$$
\Lambda = \frac{2}{\beta_p}\left[\iota^2 - \frac{2}{\epsilon^2+1}\frac{\epsilon^2-1}{3\epsilon^2+1}(\frac{1}{2}+\frac{3}{2}\Delta) + 2\beta_p\frac{\epsilon^2-1}{3\epsilon^2+1}\frac{2}{\epsilon^2+1}\right] \qquad (3.65)
$$

The differential of the current can be written as:

$$\delta j = \frac{1 - \lambda(\frac{a_0}{b})^{2(m+1)} - 2(\frac{a_0}{b})^{2(m+1)}}{(1+\lambda)[1-(\frac{a_0}{b})^{2(m+1)}]} \tag{3.66}$$

Where $\delta j = \frac{dj_{internal}}{da} - \frac{dj_{external}}{da}$, $j_{internal}$ and $j_{external}$ is the current density inside and outside of the boundary. Considering the case in which b is infinite, $(\frac{a_0}{b})^{2(m+1)}$ tends to zero. Then

$$\delta j = \frac{1}{1+\lambda} \tag{3.67}$$

We can further obtain the kink criteria by submitting Eq.3.67 into Eq.3.64:

$$\delta j > \frac{2}{5 - \sqrt{9+4\Lambda}} - 1, \; \delta j < \frac{2}{5 + \sqrt{9+4\Lambda}} - 1 \tag{3.68}$$

After getting the criteria for these two different modes (Eq.3.59 and Eq.3.64), we use Corsica[71, 83] to generate new current profiles and recalculate equilibria. The aim is to adjust the current profile to make only one of peeling mode and kink mode unstable. The plasma volume is calculated in the (ψ, θ, ϕ) coordinates, $dr^3 = J_0 d\psi d\phi d\theta$. The Jacobian J_0 of the coordinate system obeys the equation:

$$\frac{\partial J_0}{\partial \psi} = -2\frac{\partial}{\partial \psi} lnB_p - 2\beta_p \frac{\partial}{\partial \psi}(\mu_0 P) - \left(\frac{B_t}{B_p}\right)^2 \frac{\partial}{\partial \psi} ln(RB_t) \tag{3.69}$$

The we can obtain the current profiles that meet the crieria of peeling and kink modes, shown in Fig.3.8

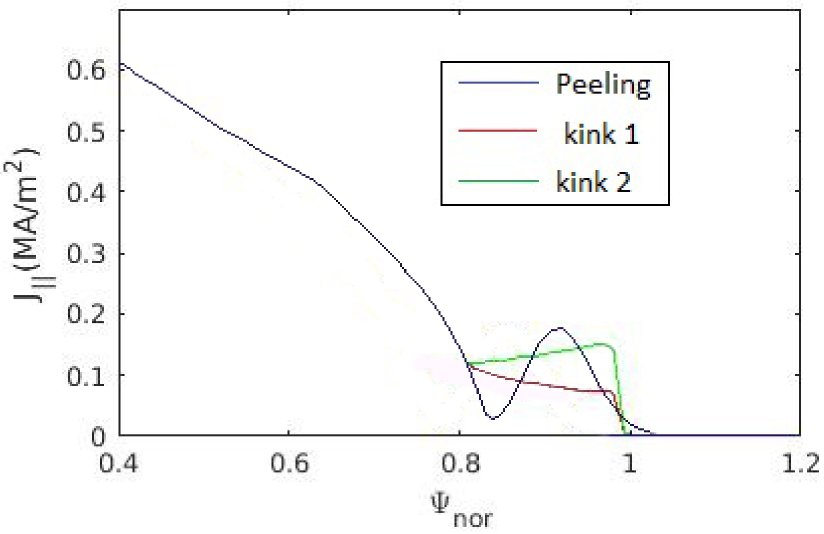

FIGURE 3.8: The parallel currents against normalized flux coordinate. The blue line is peeling unstable, whilst red and green lines are the two solutions of Eq.3.64, the region between them is the kink-instability area.

From Fig.3.8 it can be seen that the region where kink instability exists is quite small. Then it is possible to regenerate equilibria which meets special criteria(Fig.3.9).

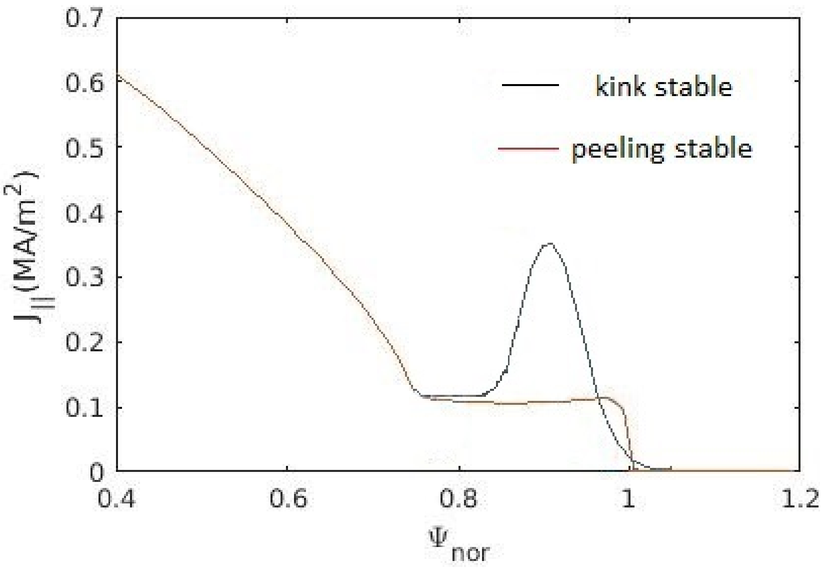

FIGURE 3.9: The current profiles in simulations, the black one makes kink stable but peeling unstable, on the contrary, the red one is peeling stable but kink unstable profile.

3.4 Simulation results

In the simulations of ELM, Eq.3.54 to Eq.3.58 are solved using the BOUT++ framework. First, we scan over different toroidal modes using the equilibria generated from the “peeling stable” and “kink stable” profiles in Fig.3.9 separately. The starting equilibrium is one of widely used shifted circular equilibria named cbm18[122–124], shown in Fig.3.10. Some of the primary plasma parameters are as follows: minor radius $a = 1.2m$, major radius $R_0 = 3.4m$, magnetic field on axis $B_0 = 1.94T$, edge safety factor $q \approx 3$. The starting equilibrium pressure, current and q profiles are demonstrated in Fig.3.11. Then equilibria are regenerated applying current profiles in Fig.3.9.

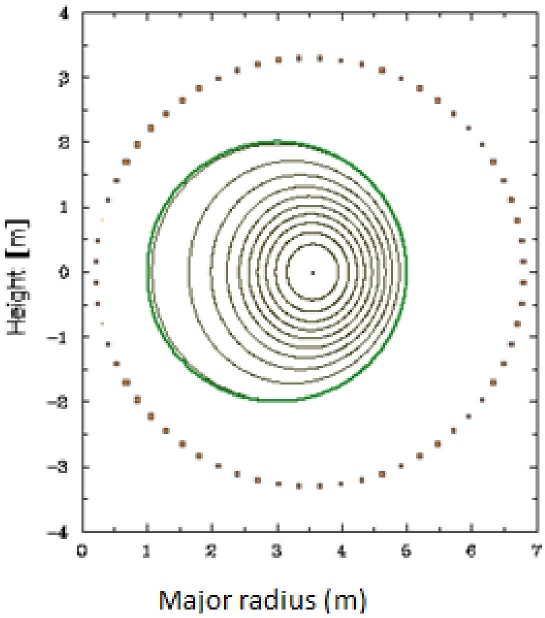

FIGURE 3.10: The sketch of cbm18 shifted circular equilibrium.

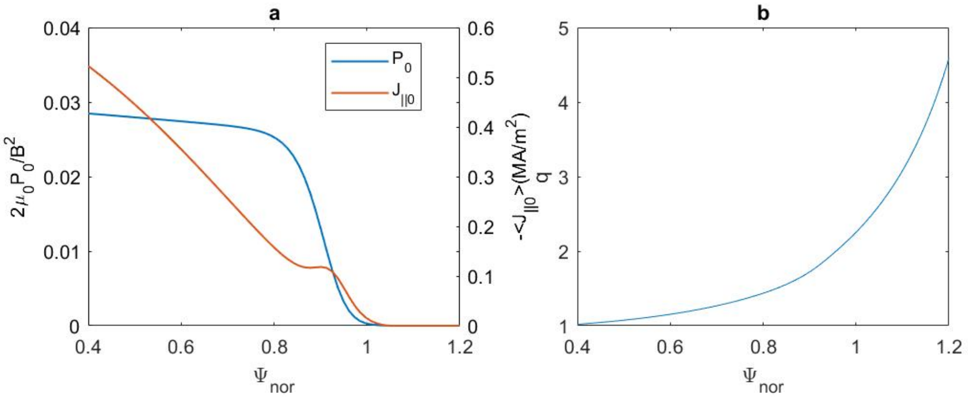

FIGURE 3.11: The pressure, current profiles(a) and q profiles(b) versus normalized flux coordinate.

We then use the BOUT++ 3-field reduced MHD model (Eq.3.54 to Eq.3.58) to study ELM stability[124] in different profiles. The evolving quantities are vorticity, the parallel component of the vector potential, and the plasma pressure. All the outer boundary conditions of involving variables are Dirichlet, while inner boundary conditions are Neumann. The grid resolution is $n_\Psi = 260$, $n_y = 64$, which performed well in previous BOUT++ simulation study on the influence of different current profiles modified by CORSICA[122].

To distinguish current-driven and pressure-driven instabilities, we carry out simulations by turning off pressure gradient term and current term respectively in RHS of Eq.3.54, shown in Fig.3.12.

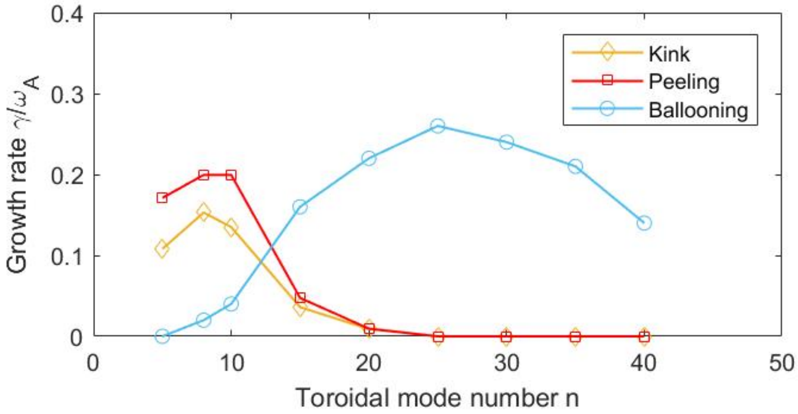

FIGURE 3.12: The linear growth rates of current-driven and pressure-driven modes versus toroidal mode number n . The growth rates are normalized by Alfven frequency. The yellow line labelled with diamonds is the growth rate of the kink mode, whilst the red square line is the peeling growth rate. The blue circle line is the growth rate of the pressure-driven instabilities.

From Fig.3.12, it can be concluded that the current-driven modes peak at lower toroidal model number than pressure-driven instabilities. Moreover, current-driven (yellow diamond line) instabilities are also triggered in peeling stable equilibria. To identify the kink and peeling mode further, we then perform the spatial Fourier transform on perturbed ϕ in the poloidal direction (y direction in BOUT++), the mode structures of 'kink' (Fig.3.13) and 'peeling' (Fig.3.14) modes are then obtained:

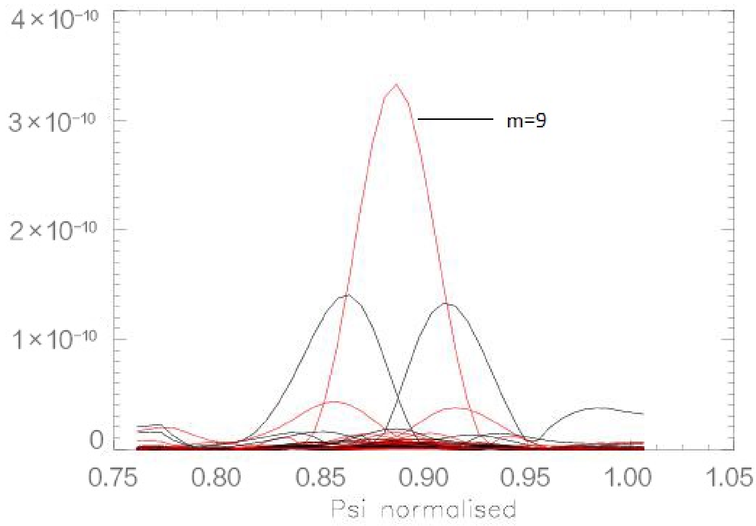

Figure 3.13: Poloidal resonance mode structures of the equilibrium with regenerated by peeling stable current profile , the x axis is the normalized flux coordinate. Toroidal mode number n=10.

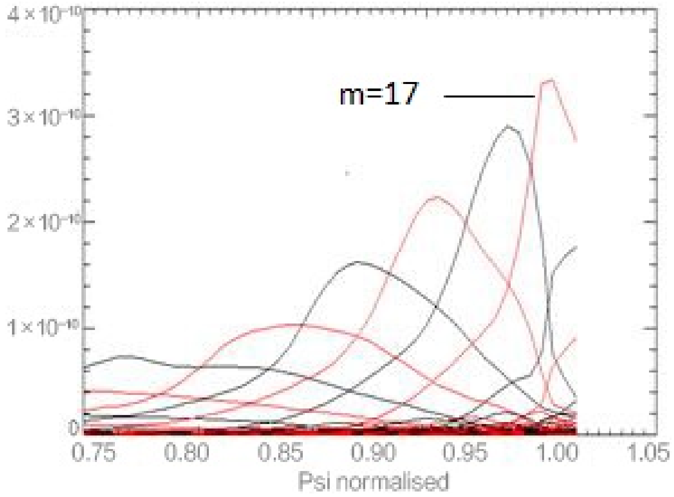

Figure 3.14: Poloidal resonance mode structures of the equilibrium with regenerated by kink stable current profile , the x axis is the normalized flux coordinate. Toroidal mode number n=10.

After comparing these above two figures, it can be seen that the mode structure in Fig.3.13 has a lower mode peak resonance number. These poloidal resonance mode structures are more close to kink mode, while the peeling mode, shown in Fig.3.14, localized at the edge. In addition, the main resonance flux surface in Fig.3.13 lay on $m = 9$, while the major poloidal mode in Fig.3.14 is $m = 17$. Therefore, kink mode can trigger pedestal instability instead of peeling mode, with the special current profiles in our simulation.

Then we verify our assumption from the aspects of resistivity, because it is recognized that internal and external current-driven modes are sensitive to plasma resistivity[25, 110]. When considering the resistive effect, the parallel electric field Eq.3.57 becomes:

$$\frac{\partial \psi}{\partial t} = -\frac{1}{B_0}\nabla_{||}\phi + \frac{\eta}{\mu_0}\nabla_{\perp}^2\psi \tag{3.70}$$

where η is the resistivity. In BOUT++, a dimensionless ratio-Lundquist number denoted by S is used to define the resistivity:

$$S = \frac{R_0 v_A}{\eta} \tag{3.71}$$

where R_0 is the typical length scale of the MHD system. In BOUT++, two separate coefficients S_{core} and $S_{boundary}$ denoted core and boundary Lundquist numbers , corresponding to the region inside ($\Psi_{nor*} < 1$) and outside ($\Psi_{nor*} > 1$) the plasma edge .In the equilibrium with kink unstable but peeling stable profile, we simulate several cases with different core and boundary Lundquist numbers:

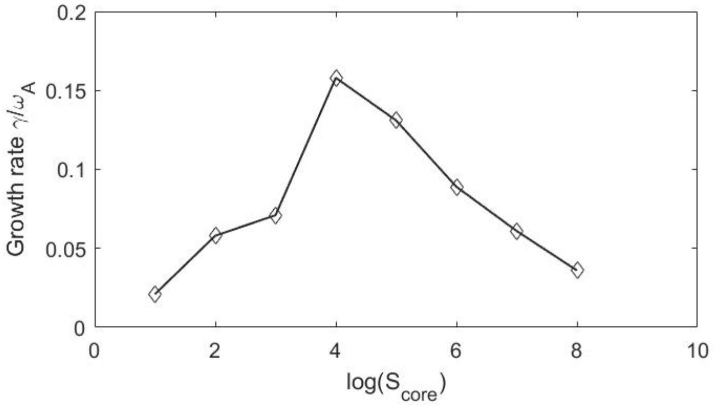

FIGURE 3.15: The growth rate of ELM versus the core Lundquist number, toroidal mode number n=10.

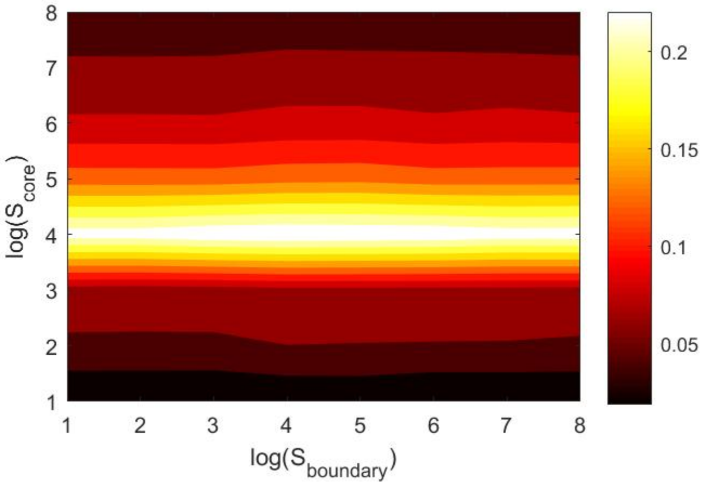

FIGURE 3.16: The spectrum of growth rate for the kink unstable case versus the core and boundary Lundquist number, the index of x and y axis is logarithm of boundary Lundquist number respectively, where toroidal mode number n=10.

Comparing Fig.3.15 with Fig.3.16, it can be seen that the growth rates relate to core plasma resistivity and do not respond to the resistance of the boundary plasma. Then, it is verified that, in some cases when peeling modes are stable, kink mode plays a dominant role in the current driven mode in ELM crashes. Since this kink mode can also couple to the ballooning mode, we call this kind of instability the kink-ballooning mode. The current-driven (peeling) component of the peeling-ballooning mode is sensitive to resonances outside the plasma. This makes it sensitive to the separatrix and resistivity in the SOL. However, current-driven (kink) modes in some circumstances are unstable in the pedestal, which is not sensitive to external resonances or conditions outside the plasma edge.

In further simulations, we then study two different fixed equilibria with two different current profiles (kink and peeling stable), noting that pressure-driven terms are concluded in simulation, with Lundquist number $S = 10^4$, shown in Fig.3.16.

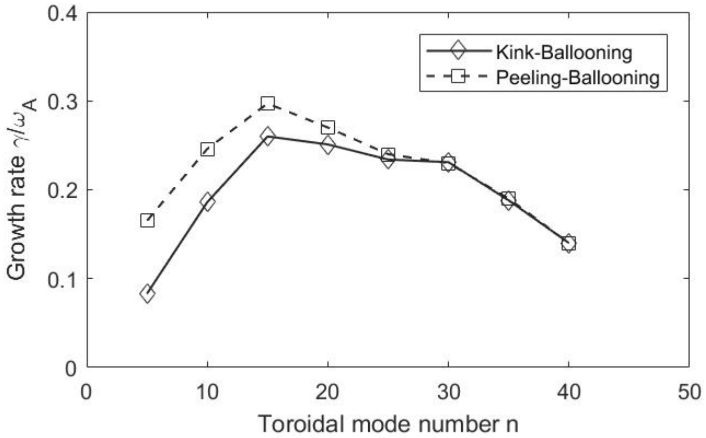

Figure 3.17: Linear growth rates for different toroidal numbers, the core and boundary lundquist number $S_{core} = S_{boundary} = 10^4$, the dashed square line denotes peeling-ballooning mode while solid diamond line is kink-ballooning mode.

Fig.3.16 shows that the kink-ballooning mode has a lower growth rate than the peeling-ballooning mode at low toroidal mode numbers, whilst they become similar at high mode number. The peak growth rates for resistive kink-ballooning mode (n=15) are lower than peeling-ballooning mode. Presumably at high n both kink and peeling cases are driven by pressure (ballooning) not current. Current-driven modes should be mainly at low n.

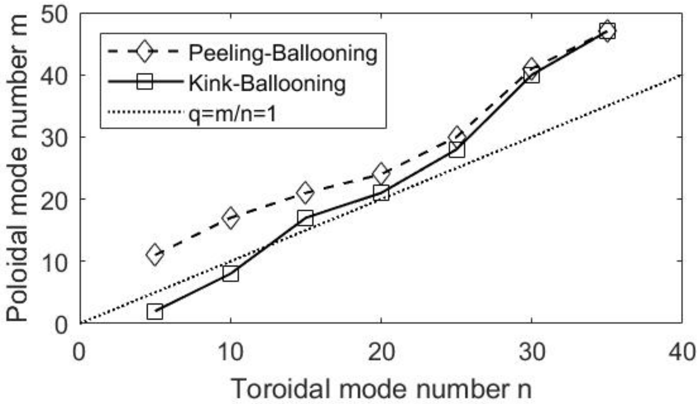

Figure 3.18: Peak resonance poloidal number for different toroidal numbers, core and boundary lundquist number $S_{core} = S_{boundary} = 10^4$, the dashed-diamond line is peeling-ballooning mode while solid-square line is kink-ballooning mode.

From Fig.3.18, we could find that kink-ballooning mode has lower resonant poloidal modes. And the main resonant q surfaces are around but not limited to q=1 profile.

3.5 Summary and disscussion

In this chapter, the theories of ballooning, peeling and kink modes have been discussed critically. The general reduced MHD equations were also reviewed. Following on the derivation from previous work[92], we propose the kink-ballooning mode plasma instability which is driven by the current gradient inside the resonance surface and boundary pressure gradient. From the energy principle, we get the kink mode criteria related to plasma current and current gradient. Then Caltrans-Corsica is used to generate new equilibria for fixed current profiles. Simulations of these generated equilibria indicate kink-ballooning mode can drive pedestal instabilities, even if when peeling mode keeps stable, only in special current profiles. The results also show Kink-ballooning mode has smaller poloidal resonant mode and lower growth rates at low toroidal mode number. In ITER's design, peeling mode is stable for the strong magnetic and current shear in outer boundary[125]. Kink instabilities may be an alternative way for current-driven mode, if some possible ways were found to achieve the special current profiles.

Limitations of the work in this chapter are also apparent. Due to the inevitable numerical instabilities, simulations of geometries with X-point are not available. Recent FCI (Flux Coordinate Independent) method work on BOUT++ make much better treatments of the geometry with X-point[126]. In future work, we plan to extend the work in this chapter into X-point regions, by applying FCI method into BOUT++ ELM simulations. Secondary, although we verified the existence of kink-ballooning mode in simulation, the edge current profile of kink mode is a bit unrealistic. One of the possible ways to obtain such current profiles is current ramp-down. In the ramp-down phase of FTU (Frascati Tokamak Upgrade) tokamak[127], edge current was found to decrease greatly.Therefore, current ramp may be one possible way to make the pedestal current profiles close to ones used in our simulations. In the ITER design, poloidal field (PF) coils are believed to play a significant role in maintaining and fixing plasma shape and current in ramp-down phase[128]. In addition, the resonance gap for peeling mode are narrower in X-point shape. Then current-driven mode can be mixed with peeling and kink mode, with the operation of PF coils. However, no literature reports edge current control utilizing current ramps. The possibility of this work's link to experiments requires a plenty of further studies.

Chapter 4

Non-inertial effects in plasma and its roles on flow-shear, GAM and Zonal Flows

In the study of plasma rotation[129] and GAM (including zonal flow)[130], centrifugal convection has been shown to play a key role due to plasma toroidal rotation. However, it is not self-consistent to just add some non-inertial convection terms to the inertial MHD equations[131]. There have been few studies of Coriolis force effects on GAM and ZF, while Coriolis force effects are believed to cause parallel asymmetry in transport[132]. In this chapter, we first derive self-consistent drift-ordered 2-fluid equations from the collisional Vlasov equation in a non-inertial rotating frame, and modify the Hermes cold ion code to simulate rotation's effects on GAM and ZF. The simulation results show that plasma rotation can increase the amplitude of ZF and GAM frequency. Moreover, it is found that Coriolis convection plays an important role in GAM's propagation and ZF's global structure.

In this chapter, theories of plasma spin-up, GAM and ZFs at first. Then a new nonlinear drift-fluid 5-field equations are developed in the non-inertial system from non-inertial collisional Vlasov equation. Simulations are also performed by modifying the Hermes cold ion model to study the centrifugal and Coriolis' effects on GAM and Zonal flow. We also derived a simplified analytic model to explain the results. At last, the preliminary experimental results are listed, aiming to validate the results.

4.1 Introduction of plasma poloidal spin-up

As reviewed in Chapter 1, flow shear and plasma rotation play an important role in suppressing MHD instabilities including ELMs. Therefore, exploration of the mechanisms of the plasma rotation is also an attractive subject. Generally, plasma rotation refers to flow on a flux surface[133]. It has been verified that external torques, such as helical field and NBI[134] can generate plasma rotation. However, it has been suggested that these methods are not suitable for ITER [135]. In some experiments[136, 137], the observation of spontaneous plasma rotation in the absence of an external momentum source has led to a renewed interest in plasma rotation and a focus on rotation measurement. However, the origins of this spontaneous rotation, especially poloidal rotation, are not fully understood. It is supposed that $\mathbf{E} \times \mathbf{B}$ flow and dia-magnetic flow contribute to the rotation in the boundary, but the rotation also occurs in core regions[138]. Other neo-classical effects such as finite-orbit, residual stress and neo-classic toroidal viscosity in non-axisymmetric magnetic fields are also proposed to explain the plasma rotation[133], which are not the focus of this thesis.

Hassam suggested a poloidal plasma rotation mechanism by developing the Stringer spin-up theory [139]. He pointed out that the injection of NBI or Ion Cyclotron Resonance Heating(ICRH) can produce an in-out asymmetric density distribution on a magnetic surface, which may induce a poloidal plasma rotation.

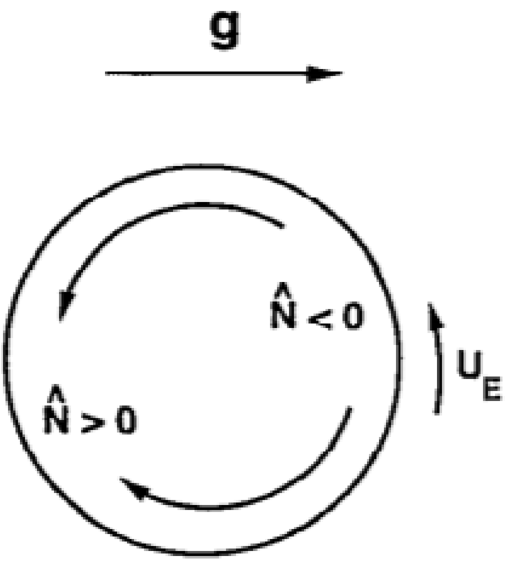

FIGURE 4.1: The coupling effects of effective gravity and perturbation flows. [139]

As shown in Fig.4.1, the in-out asymmetry density generates a parallel (poloidal) flow. When introducing a perturbation flow u_E, which causes the parallel flow shift along the poloidal direction. These flows causes an enhancement of the density ($N > 0$) in the lower half plane and the decrease of density ($N < 0$) in the upper half plane. Coupling with the effective gravity, the high density flow moves outboard while the low density flows inboard. This accelerates the perturbation flow u_E, and the growth of u_E is named the stringer spin-up[139]. However, due to the poloidal pumping, this flow is always damped[133], and an external source is required.

Later, Liu[129] developed Hassams work based on Hsu's[140] theory, in this theory, the magnitude of the poloidal density asymmetry would be significantly enhanced by the RF wave cyclotron heating because of the resonance localization. This kind of asymmetry can induce a poloidal electric field, ions will redistribute and form a poloidally in-homogeneous ion profile acted on by this field, which has the same effects as the in-out asymmetric density source in Hassams mode. Combining the poloidal density asymmetry produced by the resonance localization in the RF wave cyclotron heating with the poloidal plasma spin-up destabilized by the inout density asymmetry, the poloidal plasma rotation can be actively produced by means of Electron Cyclotron waves. If developed further, this may provide a way to control ELMs which would be reactor relevant.

The spin-up velocity is based on high order perturbation and the equations are similar to Hasegawa-Wakatani equation[59](will be reviewed in the next section). The stringer spin-up later was thought of as a kind of GAM or ZF under the effects of centrifugal force (effective gravity)[62]. Then the focus of this chapter becomes the effects of toroidal rotation on GAM and ZF.

4.2 Plasma physics in rotating frame

In the study of meteorology physics, the non-inertial effects comprising centrifugal and Coriolis force are important and essential concepts due to the rotation of earth. This deflects the direction of the wind to the right in the northern hemisphere and to the left in the southern hemisphere. This is why the wind-flow around low and high-pressure systems circulates in opposing directions in each hemisphere. In the formation of tornadoes, associated centrifugal and Coriolis forces play important roles, coupling with the pressure gradients of atmosphere[141].

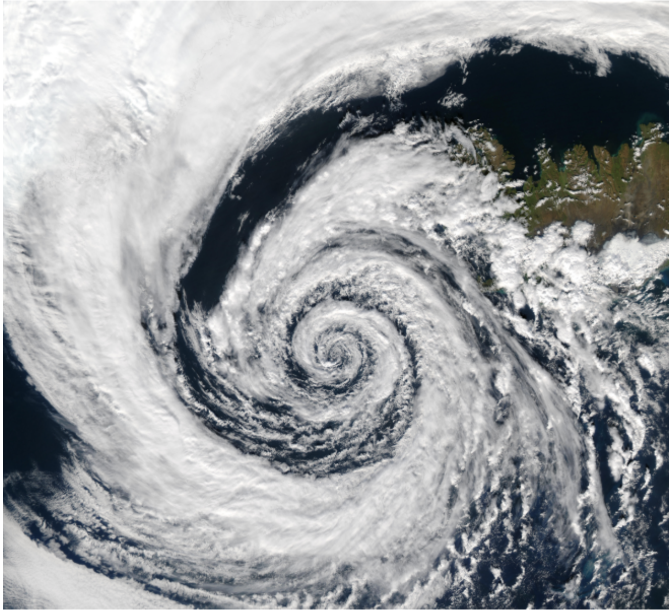

FIGURE 4.2: This low-pressure system over Iceland spins counterclockwise due to balance between the Coriolis force and the pressure gradient force. [141]

Historically, the equations of plasma physics have generally been studied using inertial reference frames, not least because Maxwells equations have their simplest form in such frames. However, tokamak plasmas often rotate at high velocities [9], which leads to the changes of equilibrium and plasma profiles when plasma rotation along the curved field lines[10]. However, the initial tokamak profiles are usually assumed to be in a stationary state. It is likely that the observed behaviour of such systems can be better understood in some respects by considering the equations determining their evolution in suitable non-inertial frames.

A well-known centrifugal force effect due to the impurity toroidal rotation in a tokamak plasma can push the impurities to accumulate on the outboard side of the flux surface (in-out asymmetry), which has been pointed out theoretically by Hinton[142] and Wesson [143] earlier and observed in the tokamak experiments [144, 145]. On the other hand, the Coriolis force is known to play an important role in the anomalous momentum transport that leads to spontaneous rotation[72, 146], and its impact on heat and particle transport[147] has also been studied.

In the study of plasma rotation[129] and GAM (including zonal flow)[130], centrifugal convection has been proven to play a key role due to plasma toroidal rotation. However, it is not self consistent to just add some non-inertial convection terms to the inertial MHD equations[131]. Also, the studies of Coriolis force effects are absent in the study of GAM and ZF, while Coriolis force effects is believed to cause parallel asymmetry in transport[132]. Peeters[146] first developed a self-consistent drift kinetic equation in non-inertial system to explore plasma momentum transport. But a self-consistent drift MHD model in non-inertial frame is still required, which can benefit the study of centrifugal and Coriolis force effects on ZF and GAMs.

4.3 Review of theories of GAM and Zonal Flow

4.3.1 Zonal Flow

Before exploring the effect of toroidal rotation, it is necessary to review the origins and basic theories of GAM and ZF. As reviewed in chapter 1, Zonal flows are a kind of azimuthally symmetric flow, which can be triggered by a toroidally symmetric electric field perturbation in toroidal plasma.[62] This flow contributes to plasma poloidal rotation and flow shear, the significant role of which is widely recognized in plasma confinement and L-H transition. Normally, zonal flows (ZF) and geodesic acoustic modes (GAMs) are present at the structure of $n = 0, m = 0, 1$, which were discovered in a theoretical magneto-hydrodynamic (MHD) analysis[148] and confirmed by several experiments[68, 149].

Instead of interacting with temperature and density gradient directly, ZF and GAM should often be grouped generically together with drift waves in a non-linear process. In plane geometry, there are generally two kinds of parametric drift-wave instability that can trigger ZFs[62]. One of them is the parametric decay instability, with wavenumber k_0 and frequency ω_0. This main drift wave can decay into two further waves with wave vectors $\mathbf{q}, \mathbf{k_1}$ and frequencies Ω, ω_1. Then the growth rate generated by this kind of instability is[150]:

$$\gamma = c_s \rho_s |\mathbf{k_0} \times \mathbf{q}| \sqrt{\frac{T_e}{T_i} \frac{k_0^2 - k_1^2}{q^2} \frac{e\Phi_e}{T_e}} \tag{4.1}$$

where the Φ_e is the electrostatic potential perturbation. The growth rate turns to zero when $k_0^2 = k_i^2$. Therefore, ZF can be driven when parametric decay instability occurs. The other kind of instability is called parametric modulational instability, which is driven by other two waves generated by the interactions between ZF and main drift wave. The growth rate excited by modulational instability has the following expression[59]:

$$\gamma = \sqrt{2} |\mathbf{k_0}_\perp \times \mathbf{q}| \sqrt{\Phi_e^2 - \frac{k_0^2 q^4}{2|\mathbf{k_0} \times \mathbf{q}|^2}} \tag{4.2}$$

In the general geometry and numerical studies, a simple reduced MHD model can describe mechanism of ZF flows well named Hasegawa-Wakatani (HW) equations[150]:

$$\frac{\partial n}{\partial t} = -\kappa \nabla_\perp \phi + [n, \phi] \tag{4.3}$$

$$\frac{\partial \omega}{\partial t} = [\omega, \phi] + \alpha(\phi - n) + \mu \nabla^2 n \tag{4.4}$$

where the resistive coupling term $\alpha = T_e k_{||}^2/(n_0 e^2 \eta \omega_{ci})$, η is the plasma conductivity, ω_{ci} is the ion cyclotron period, and μ is the ion viscosity coefficient. The vorticity $\omega = \nabla^2 \phi$, and the constant density gradient force term is

$$\kappa = -\frac{\partial ln(n_0)}{\partial x} \tag{4.5}$$

The bracket $[B, A]$ has the expression:

$$[B, A] = \frac{1}{J\sqrt{g_{yy}}}[(g_{yy}\frac{\partial B}{\partial z} - g_{yz}\frac{\partial B}{\partial y})\frac{\partial A}{\partial x} \\ +(g_{yz}\frac{\partial B}{\partial x} - g_{xy}\frac{\partial B}{\partial z})\frac{\partial A}{\partial y} + (g_{xy}\frac{\partial B}{\partial y} - g_{yy}\frac{\partial B}{\partial x})\frac{\partial A}{\partial z}] \tag{4.6}$$

Many simulation studies have been based on the HW equations. For example, Dewhurst[151] demonstrated intuitive images of ZF and drift waves in slab geometry, showing that the interactions and competition between ZFs and drift waves (Figure.4.3).

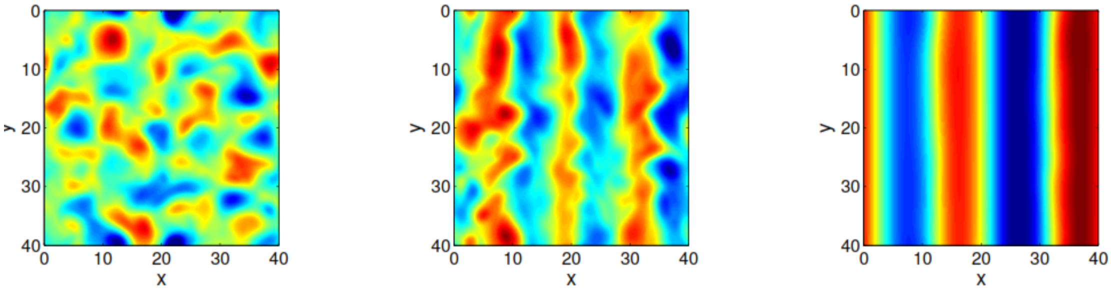

FIGURE 4.3: Electrostatic potential in quasi-stationary in 3 different cases: left where ZFs are damped, middle where total kinetic energy is balanced between zonal flows and non-zonal drift wave , and the right figure is the ZF dominant state.

[151]

In toroidal equilibrium, the space vector of drift wave is similar to ballooning eigen-function. The growth rates of GAM meet the equation:

$$\gamma^2 = \frac{2+\eta}{1.6\epsilon^{3/2}}\frac{B_\theta^2}{B_t^2}k_\theta^2 q_r^2 c_s^2 \rho_s^2 |\phi_0|^2 \tag{4.7}$$

where ϵ is inverse aspect ratio, c_s is sound speed in plasma.

4.3.2 Geodesic acoustic mode (GAM)

Different from the ZF, the GAM is generally driven by an $m = 1$ density oscillation, this oscillation is mainly top and bottom asymmetric. Figure.4.4 illustrates the mechanism intuitively: since the distributions of potential gradient $\nabla\phi$ are close to symmetric along the flux surface, the $\mathbf{E} \times \mathbf{B}$ drift velocity is higher on LFS than HFS due to the toroidal effects since $\mathbf{V}_{\mathbf{E}\times\mathbf{B}} \approx \frac{\nabla_\perp \phi}{B}$, resulting in the density accumulating on the bottom or top. Benefiting from the diamagetic effects, the pilling-up of poloidal density or pressure gradient can restore this imbalance due to momentum compression $\nabla\cdot(n\mathbf{V})$. That makes this kind of oscillation propagate along the radius direction[125].

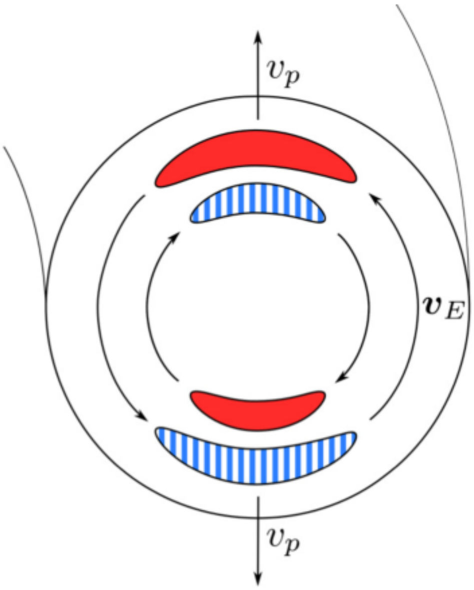

Figure 4.4: Sketch of a geodesic acoustic mode. Imbalance of zonal ExB flow on high and low field side, leads to compression or expansion of the plasma (indicated by the lled and striped areas, respectively). Thus, an up-down anti-symmetric $m = 1$ density perturbation arises, which is phase-delayed against the flow by $\pi/2$. This propagates outwards at phase velocity $\mathbf{v}_p$. [125]

The basic GAM dissipation equations can be derived from normal reduced MHD equation including density evolution. The dispersion relationship for the standard GAM was given by Winsor in 1968[66].

$$\omega_{GAM}^2 - \frac{2c_s^2}{R^2} - k_{||}^2 c_s^2 = 0 \tag{4.8}$$

where the $k_{||}$ is GAM's parallel wave number. Assuming $k_{||} = \frac{1}{Rq}$,we can obtain the frequency of GAM:

$$\omega_{GAM}^2 = 2\frac{2c_s^2}{R^2}(1 + \frac{1}{2q^2}) \tag{4.9}$$

And the phase velocity or 'group velocity' of GAM propagating outwards can be written as[125]:

$$v_p = \omega_{GAM}/k_r \tag{4.10}$$

In the further study, some other kinetic effects such as ITG and TEM have been included in the GAM and ZF studies[62], reviewed by Diamond, but the mechanism does not significantly change.

4.3.3 ZFs and GAMS with plasma rotation

It has been found that in a non-rotating system, ZFs are linearly stable and the GAMs are standing waves[62]. However, as it is pointed out in section 1, it has been suggested that there exists a critical equilibrium toroidal rotation flow in a tokamak plasma[72, 142], this is especially the case in experiments with strong tangential injection of neutral beams (NBI),to control the internal transport barrier induced by ZFs [152–155] and Electron Cyclotron Resonance Heating (ECRH)[137]. In both NBI and ECRH cases[155], the character(frequency, group velocity etc) of zonal flow and GAMs differ from theoretical results. General theories propose NBI torque and changes of ion temperature gradient (ITG) influence the frequency of ZF and GAMs[152]. But McDermott's experimental studies on ASDEX-U argue these views and find that the main influence on ZFs of NBI is the change of toroidal rotation[137]. Similar experiments on T10 verify Mcdermott's finding and suggest that the enhancement of electrostatic potential's asymmetricity is one of the main factors influencing ZF and GAMs[156]. Therefore, it is of great interest to investigate the effects of toroidal flow on ZFs and GAMs.

Some authors proposed the centrifugal correction and residual force caused by rotation are the key emergence to cause the changes in GAM and ZFs. The solved the eigenvalue problem of geodesic acoustic modes in such toroidally rotating plasmas using fluid models [130, 157]. Two solutions of fourth order polynomial dispersion relation are given[130]:

$$\omega_{GAM}^2 = \frac{c_s^2}{2R_0^2}\left(2+\frac{1}{q^2}+4M^2+\sqrt{(2+\frac{1}{q^2}+4M^2)^2+\frac{2M^4}{q^2}}\right) \tag{4.11}$$

$$\omega_{GAM}^2 = \frac{c_s^2}{2R_0^2}\left(2+\frac{1}{q^2}+4M^2-\sqrt{(2+\frac{1}{q^2}+4M^2)^2+\frac{2M^4}{q^2}}\right) \tag{4.12}$$

M is the rotation Mach number. However, centrifugal force only exists in the non-inertial system. It is also worth noting in this context that Camenen et al [147] finds that the Coriolis force can also have a significant effect on the turbulent transport of impurity ions, particularly those with low Z/A. Therefore, in the further study of parallel transport, it is still needed to extend toroidal rotation's effects into the non-inertial system with the consideration of all the non-inertial terms.

In the later sections of this chapter, we will follow Simakov's[85] methods to derive cold ion drift-ordered 2-fluid equations from the collisional Vlasov equation in non-inertial rotating frame. Based on this model, we will modify the Hermes code[84] and carry out simulations to explore toroidal rotation's effects, especially the non-inertial effects on GAMs and ZFs in the following section.

4.4 Drift-ordered fluid equations in a non-inertial frame

The time evolution of plasma distribution function is well described by the collisional Vlasov equation[9]:

$$\frac{\partial f_a}{\partial t}+\mathbf{v}\cdot\nabla f_a+\frac{e_a}{m_a}(\mathbf{E}+\mathbf{v}\times\mathbf{B})\cdot\frac{\partial f_a}{\partial \mathbf{v}}=C_a(f_a). \tag{4.13}$$

Where $f_a(x,v,t)$ represents the distribution function, a is the species of particles, the right term of the equality is the collision operator. With integral and moments operating on this equation, some standard descriptions of plasma such as the drift kinetic equation and fluid equations can be obtained. Nevertheless, since this

Vlasov equation is formulated in an inertial frame, modifications to the equation are required for rotating systems. Thyagaraja proved that the Vlasov equation has the same homogenous expression in a rotating systems[131]. However, tokamak profiles are measured in laboratory coordinate. Therefore, a distribution equation in non-inertial frame with regard to laboratory's electrostatic potentials is needed.

When treating fluid plasma in a moving frame, there is a coordinate transformation from laboratory frame to moving frame $\mathbf{q}(\mathbf{r}, \mathbf{v}, t) \rightarrow \mathbf{Q}(\mathbf{r}, \mathbf{v}_*, t)$, where $\mathbf{v}_* = \mathbf{v} - \mathbf{V}_*$, $\mathbf{V}_*$ is the velocity of the moving frame, then derivatives transform is written as:

$$\mathbf{q} = S_t \mathbf{Q} \tag{4.14}$$

S_t refers to Lorentz transformation matrix from $\mathbf{q}$ to $\mathbf{Q}$.The equality $S_t^T = S_t^{-1}$ is then obtained, with assuming the transformations between $\mathbf{q}$ and $\mathbf{Q}$ are reversible. The derivative of both sides are related by the following expression:

$$\dot{\mathbf{q}} = \dot{S}_t \mathbf{Q} + S_t \dot{\mathbf{Q}} \tag{4.15}$$

Applying $\mathbf{Q} = S_t^{-1}\mathbf{q}$, Eq.(4.15) is rewritten as the following, since $S_t S_t^{-1}$ is an anti-symmetric matrix.

$$\begin{aligned} \dot{\mathbf{q}} &= \dot{S}_t S_t^{-1} \mathbf{q} + S_t \dot{\mathbf{Q}} \\ &= \boldsymbol{\omega} \times \mathbf{q} + S_t \dot{\mathbf{Q}} \\ &= S_t(\boldsymbol{\omega} \times \mathbf{Q} + \dot{\mathbf{Q}}) \end{aligned} \tag{4.16}$$

Where $\boldsymbol{\omega}$ is the eigen-matrix of $\dot{S}_t S_t^{-1}$. After differentiating in time, we obtain from Eq.(4.17)

$$\ddot{\mathbf{q}} = S_t(\ddot{\mathbf{Q}} + 2\boldsymbol{\omega} \times \dot{\mathbf{Q}} + \boldsymbol{\omega} \times (\boldsymbol{\omega} \times \mathbf{Q}) + \dot{\boldsymbol{\omega}} \times \mathbf{Q}) \tag{4.17}$$

Combined with the Newton-Lorentz law, Eq.4.17 can be further rewritten as

$$\ddot{\mathbf{Q}} = -2\boldsymbol{\omega} \times \ddot{\mathbf{Q}} - \boldsymbol{\omega} \times (\boldsymbol{\omega} \times \mathbf{Q}) - \dot{\boldsymbol{\omega}} \times \mathbf{Q} + \frac{e_a}{m_a} S_t^{-1}(\mathbf{E} + \mathbf{v} \times \mathbf{B}) \tag{4.18}$$

Supposing a uniformly-rotating frame, where the rotation frequency is Ω_0 ,the Lorentz transformation has the following form from $\mathbf{q}(ct, R, \phi, Z)$ to $\mathbf{Q}(ct_*, Rr_*, \phi_*, Z_*)$[158],

$$S_t = \begin{bmatrix} \gamma & 0 & -\gamma\beta & 0 \\ 0 & 1 & 0 & 0 \\ -\gamma\beta & 0 & \gamma & 0 \\ 0 & 0 & 0 & 1 \end{bmatrix}$$

where $\gamma = (1-(r\Omega_0/c)^2)^{-1/2}$ is the Lorentz factor, $\beta = r\Omega_0/c$. In the non-relativistic limit,the electric and magnetic fields in the laboratory and rotating frames are related by the expressions [159]

$$\begin{aligned} \mathbf{B}_* &= \mathbf{B} \\ \mathbf{E}_* &= \mathbf{E} + (\mathbf{\Omega_0} \times \mathbf{R}) \times \mathbf{B} \end{aligned} \tag{4.19}$$

$\mathbf{\Omega_0}$ is the rotating frequency, defined as $\Omega_0 \mathbf{e_z}$ in tokamak (R, ϕ, Z) coordinate [72]. From the definition of the transformation matrix S_t, it can be seen that $\boldsymbol{\omega} = \mathbf{\Omega_0}$ the toroidal rotation rate. Therefore, collisional Vlasov equation in uniformly-rotating frames is obtained with combing Eq.(4.13), Eq.(4.18) and Eq.(4.19).

$$\frac{\partial f_a}{\partial t} + \mathbf{v}_* \cdot \nabla f_a + \frac{e_a}{m_a}\left(\mathbf{E}_* + \mathbf{v}_* \times \mathbf{B} - 2\frac{m_a}{e_a}\mathbf{\Omega_0} \times \mathbf{v}_* + \frac{1}{2}\frac{m_a}{e_a}\nabla\Omega_0^2 R^2\right) \cdot \frac{\partial f_a}{\partial \mathbf{v}_*} = C_a(f_{a*}) \tag{4.20}$$

Evidently, the metric tensor should be changed in a different coordinate system. In order to make it easier in the following integration and simulation, the metric tensor in this uniformly rotating system should be analyzed. Referring to [160], the rotating-frame transformation matrix can be expressed as (assuming time in two coordinate coincide at 0.

$$(dR_*, R_* d\Phi_*, dZ_*, icdt_*) = \begin{bmatrix} \frac{1}{\sqrt{1-\frac{R^2\Omega_0^2}{c^2}}} & 0 & 0 & 0 \\ 0 & \frac{1}{\sqrt{1-\frac{R^2\Omega_0^2}{c^2}}} & 0 & \frac{-i\frac{R\Omega_0}{c}}{\sqrt{1-\frac{R^2\Omega_0^2}{c^2}}} \\ 0 & 0 & 1 & 0 \\ 0 & 0 & 0 & \frac{1}{\sqrt{1-\frac{R^2\Omega_0^2}{c^2}}} \end{bmatrix} \begin{pmatrix} dR \\ Rd\Phi \\ dZ \\ icdt \end{pmatrix}$$

Multiplying the transformation matrix with its transpose, we obtain the co-variant tensor

$$g_{ij} = \begin{bmatrix} \frac{1}{\sqrt{1-\frac{R^2\Omega_0^2}{c^2}}} & 0 & 0 & 0 \\ 0 & \frac{1}{\sqrt{1-\frac{R^2\Omega_0^2}{c^2}}} & 0 & \frac{\frac{R\Omega_0}{c}}{\sqrt{1-\frac{R^2\Omega_0^2}{c^2}}} \\ 0 & 0 & 1 & 0 \\ 0 & \frac{\frac{R\Omega_0}{c}}{\sqrt{1-\frac{R^2\Omega_0^2}{c^2}}} & 0 & -1 \end{bmatrix}$$

Obviously, the contra-variant tensor equals to co-variant one in the non-relativitic limit $g_{ij} = g^{ij}$. We can say metric tensors keep the same in the assumed uniformly rotating system. The right side of Eq.(4.20) is the Fokker-Planck collision operator, we assume its form keeps the same in current frame. Following the process in most plasma textbooks[89], we can obtain fluid equations by integrating zero, first, second(scalar) moments over Eq.(4.20) for plasma species j, namely the continuity equation,

$$\frac{\partial n_j}{\partial t} + \nabla \cdot n_j \mathbf{V_j} = S_j^n \tag{4.21}$$

the momentum conservation equation,

$$\begin{aligned} \frac{\partial m_j n_j \mathbf{V_j}}{\partial t} + \nabla p_j + \nabla \cdot (\overleftrightarrow{\pi} + m_j n_j \mathbf{V_j} \mathbf{V_j}) = Z_j e n_j (\mathbf{E} + \mathbf{V_j} \times \mathbf{B}) \\ + 2 m_j n_j \mathbf{V_j} \times \mathbf{\Omega_0} + m_j n_j R \Omega_0^2 \nabla R + \mathbf{R_j} + \mathbf{S_j^m} \end{aligned} \tag{4.22}$$

and the energy conservation equation,

$$\begin{aligned} \frac{\partial}{\partial t}(\frac{3}{2} p_j + \frac{1}{2} m_j n_j V_j^2) + \nabla \cdot \mathbf{Q_j} = W_j \\ + \mathbf{V_j} \cdot (\mathbf{R_j} + Z_j e n_j \mathbf{E} + m_j n_j R \Omega_0^2 \nabla R) + S_j^E \end{aligned} \tag{4.23}$$

where the $S_j^n, \mathbf{S_j^M}, S_j^e$ are density, momentum and energy sources for species j, respectively.

The viscous stress tensor $\overleftrightarrow{\pi}$ is given in Ref.[161], and the friction force between species $\mathbf{R_j}$ has the same expression as in Ref.[85]:

$$\mathbf{R_e} = -\mathbf{R_i} = e n_e \left(\frac{\mathbf{J}_{||}}{\sigma_{||}} + \frac{\mathbf{J}_{\perp}}{\sigma_{\perp}} \right) - 0.71 n_e \partial_{||} T_e + \frac{3\nu}{2\Omega_e} n_e \mathbf{b} \times \nabla T_e \tag{4.24}$$

with $\sigma_{\perp} = 0.51 \sigma_{||} = e^2 n_e / m_e \nu_e$. The divergence of energy flux is written as the followings expression,

$$\begin{aligned}\nabla\cdot\mathbf{Q_j} &= \nabla\cdot[(\frac{5}{2}n_jT_j+\frac{1}{2}m_jn_jV_j^2)\mathbf{V_j}+\overleftrightarrow{\pi}\cdot\mathbf{V_j}+\mathbf{q_j}] \\ &= \nabla\cdot\iiint\frac{1}{2}m_jv_*^2\mathbf{v}_*f_ad^3v_*+\iiint\frac{1}{2}m_jv_*^2C_a(f_a)d^3v_* \end{aligned} \tag{4.25}$$

where ν_e is the electron classical collision frequency, Ω_e is the gyro-frequency of electron. T_j and $\mathbf{q_j}$ represent species' thermal temperature and heat flux respectively[85].

$$\begin{aligned}\mathbf{q_e} = -\kappa_{||e}\partial_{||}T_e &+ \frac{5p_e}{2m_e\Omega_e}\mathbf{b}\times\nabla T_e-\kappa_{\perp e}\nabla_\perp T_e \\ &-0.71\frac{T_e\mathbf{J}_{||}}{e}+\frac{3\nu_e}{2\Omega_e}\frac{T_e\mathbf{b}\times\mathbf{J}}{e}\end{aligned} \tag{4.26}$$

with $\kappa_{||e}=3.16\frac{p_e}{m_e\nu_e}, \kappa_{\perp e}=4.66\frac{p_e\nu_e}{m_e\Omega_e^2}$. Since the derivative remains unchanged in a uniformly rotation frame, viscosity terms are assumed to be the same as that in inertial frame[161], assuming the equilibrium distribution remain approximately Maxwellian. From Eq.(4.23), one can find that the Coriolis force has no contribution to the fluid energy.

Taking the same ordering and steps as Simakov's[85] work, we obtain the continuity equations under the cold ion plasma assumption:

$$\frac{\partial n}{\partial t}+\nabla\cdot[n(\mathbf{V_{E\times B}}+\mathbf{V_{mag}}+\mathbf{V_{||e}}+\mathbf{V_{pe}}+\mathbf{V_{Co-e}}+\mathbf{V_{Cf-e}})]=S^n \tag{4.27}$$

where $\mathbf{V_{||e}}$ is electron parallel velocity, the electron $\mathbf{E}\times\mathbf{B}$, diamagnetic and polarization drift velocities are defined by crossing $\mathbf{B}$ on Eq.(4.22).

$$\mathbf{V_{E\times B}}=\frac{\mathbf{b}\times\nabla\Phi}{B},\mathbf{V_{mag}}=-\frac{\mathbf{b}\times\nabla p_e}{enB},\mathbf{V_{pe}}=\frac{\mathbf{b}\times\mathbf{S_e^M}}{enB}. \tag{4.28}$$

The velocities due to Coriolis and centrifugal forces are given by:

$$\mathbf{V_{co-e}}=-\frac{2m_eV_{||e}}{eB}\boldsymbol{\Omega_{0\perp}},\mathbf{V_{cf-e}}=\frac{m_e\Omega_0^2R}{eB}\boldsymbol{b}\times\nabla R \tag{4.29}$$

Dotting Eq.4.22 with $\mathbf{b}$ and dividing by $m_e n$, we can use the continuity equation (4.27) to rewrite the electron momentum conservation equation:

$$\begin{aligned} \frac{\partial V_{||e}}{\partial t} + \mathbf{V_e}\cdot\nabla V_{||e} - \left(\frac{\partial \mathbf{b}}{\partial t} + \mathbf{V_e}\cdot\nabla\mathbf{b}\right)\cdot\mathbf{V_e} = \\ -\frac{e}{m_e}E_{||} + \frac{R_{||e}-\partial_{||}p_e}{m_e n} - \frac{\mathbf{b}\cdot(\nabla\cdot\overleftrightarrow{\pi})}{m_e n} + 2\mathbf{b}\cdot\mathbf{V_e}\times\mathbf{\Omega_0} + R\Omega_0^2\mathbf{b}\nabla R \end{aligned} \tag{4.30}$$

Performing the same operations on Eq.(4.22) for the ion species and neglecting $m_i n\mathbf{V_i}\cdot\frac{\partial\mathbf{b}}{\partial t}$ and $m_i n\mathbf{V_i}\cdot\nabla\mathbf{b}\cdot\mathbf{V_i}$ since they are comparatively small, we obtain ion parallel momentum equation.

$$\begin{aligned} \frac{\partial}{\partial t}m_i n V_{||i} + \nabla\cdot[m_i n V_{||i}(\mathbf{V_{E\times B}} + \mathbf{V_{||i}} + \mathbf{V_{co-i}} + \mathbf{V_{cf-i}})] = -\partial_{||}p_e \\ -\frac{3}{2}B^{3/2}\partial\left(\frac{\pi_{ci}}{B^{3/2}}\right) + 2m_i n_i\mathbf{b}\cdot\mathbf{V_i}\times\mathbf{\Omega_0} + m_i n_i R\Omega_0^2\mathbf{b}\nabla R + S^M_{||i} + S^M_{||e} \end{aligned} \tag{4.31}$$

Where Coriolis and centrifugal drift velocities for ions are given by:

$$\mathbf{V_{co-i}} = \frac{2m_i V_{||i}}{eB}\mathbf{\Omega_{0\perp}}, \mathbf{V_{cf-i}} = -\frac{m_i\Omega_0^2 R}{eB}\mathbf{b}\times\nabla R \tag{4.32}$$

The parallel viscosity $\frac{3}{2}B^{3/2}\partial(\frac{\pi_{ci}}{B^{3/2}}) \approx -1.28\sqrt{B}\partial_{||}[\frac{p_i}{\nu_i B}\partial_{||}(\sqrt{B}V_{||i})]$ [162] ,goes to zero in the cold ion plasma assumption. At the same time, one can write the electron and ion fluid velocities in terms of the centre-of-mass velocity[163]

$$\begin{aligned} \mathbf{V_i} \approx \mathbf{V} + O(m_e/m_i) \\ \mathbf{V_e} \approx \mathbf{V} - \frac{\mathbf{J}}{n_e e} + O(m_e/m_i) \end{aligned} \tag{4.33}$$

Then, Eqs. (4.30), and (4.33) can be combined to give a modified Ohm's law:

$$\begin{aligned} \mathbf{E}_{||} \approx \frac{R_{||e}-\partial_{||}p_e}{en_e} + \frac{m_e}{e^2 n_e}\frac{\partial J_{||}}{\partial t} - \frac{m_e}{n_e^2 e^2}(\mathbf{V_i}\cdot\nabla)J_{||} \\ -2\frac{m_e}{e}\mathbf{b}\cdot\mathbf{V_e}\times\mathbf{\Omega_0} - \frac{m_e}{e}R\Omega_0^2\mathbf{b}\nabla R \end{aligned} \tag{4.34}$$

The last two terms are relatively small compared to the other terms (m_e/m_i), and will be neglected in the following simulation. Further, following from plasma momentum conservation equation(Eq.(4.22)), we find

$$
\begin{aligned}
\mathbf{J} = \mathbf{J}_{||} + \frac{1}{B}\mathbf{b} \times \nabla p_e + en(\mathbf{V_{pi}} - \mathbf{V_{pe}}) \\
+en(\mathbf{V_{co-i}} + \mathbf{V_{cf-i}}) - en(\mathbf{V_{co-e}} + \mathbf{V_{co-e}})
\end{aligned} \tag{4.35}
$$

Applying this equation into the ambipolarity condition $\nabla \cdot \mathbf{J} = 0$, the vorticity equation can be obtained using the Boussinesq approximation[164]:

$$
\begin{aligned}
\frac{\partial \omega}{\partial t} = \nabla \cdot (\omega \mathbf{V_{E\times B}}) + \nabla_{||} J_{||} \\
-e\nabla \cdot (n\mathbf{V_{mag}} - nV_{co-i} - n\mathbf{V_{cf-i}}) - e\nabla \cdot (n\mathbf{V_{co-e}} + n\mathbf{V_{cf-e}})
\end{aligned} \tag{4.36}
$$

Using the expressions in Eq.(4.23), (4.24) and (4.26), we notice that the conservative form of electron energy equation can be written below:

$$
\begin{aligned}
\frac{\partial}{\partial t}\left(\frac{3}{2}p_e\right) + \nabla \cdot [\frac{5}{2}p_e(\mathbf{V_{E\times B}} + \mathbf{V_{||e}} + \mathbf{V_{co-e}} + \mathbf{V_{cf-e}}) \\
-\nabla \cdot (\kappa_{||e}\partial_{||}T_e) - \frac{0.71T_e}{e}\mathbf{J}_{||}] = -W_i + \frac{J_{||}^2}{\sigma_{||}} - \frac{0.71\partial_{||}T_e}{e}J_{||} \\
+(\mathbf{V_{E\times B}} + \mathbf{V_{||e}} + \mathbf{V_{co-e}} + \mathbf{V_{cf-e}}) \cdot (\nabla p_e - \mathbf{S}_e^M + m_e n R \Omega_0^2 \nabla R) + S_e^E
\end{aligned} \tag{4.37}
$$

4.5 Simulations and results

To investigate the global parallel momentum transportation under the non-inertial effects, we carry out the asymmetric simulations using the Hermes cold ion code under the BOUT++ framework. This code has good performance on the simulations on the global flux transport and edge turbulence[84]. Using the same parameters as in Ref.[84] to normalize the continuity equation (4.27), modified Ohm's law(parallel)(4.34), vorticity equation (4.36), ion parallel momentum equation(4.31)and electron energy conservative equation(4.37). Including classical perpendicular diffusion, we obtain the modified 5-field reduced 2-fluid plasma equations.

$$\begin{aligned}\frac{\partial n}{\partial t} &= -\nabla\cdot\left(n\mathbf{V}_{E\times B}+n\mathbf{V}_{mag}+n\mathbf{V}_{co-e}+n\mathbf{V}_{cf-e}\right)\\ &\quad -\nabla_{||}\left(nv_{||e}\right)+\nabla\cdot\left(D_n\nabla_\perp n\right)\end{aligned} \tag{4.38}$$

$$\begin{aligned}\frac{3}{2}\frac{\partial p_e}{\partial t} &= -\nabla\cdot\left(\frac{3}{2}p_e\mathbf{V}_{E\times B}+p_e\frac{5}{2}\mathbf{V}_{mag}+p_e\frac{5}{2}\mathbf{V}_{co-e}+p_e\frac{5}{2}\mathbf{V}_{cf-e}\right)\\ &\quad -p_e\nabla\cdot\mathbf{V}_{E\times B}-\frac{5}{2}\nabla_{||}\left(p_ev_{||e}\right)+v_{||e}\partial_{||}p_e+\nabla_{||}\left(\kappa_{e||}\partial_{||}T_e\right)\\ &\quad +0.71\nabla_{||}\left(T_ej_{||}\right)-0.71j_{||}\partial_{||}T_e+\frac{\nu}{n}j_{||}\left(j_{||}-j_{||0}\right)+\nabla\cdot\left(\frac{3}{2}D_nT_e\nabla_\perp n\right)\\ &\quad +\nabla\cdot\left(\chi n\nabla_\perp T_e\right)+\frac{m_e}{m_i}nR\nabla R\Omega_0^2\cdot\mathbf{V_{E\times B}}+\frac{m_e}{m_i}nR\Omega_0^2\nabla R\cdot\mathbf{v_{||e}}\end{aligned} \tag{4.39}$$

$$\begin{aligned}\frac{\partial\omega}{\partial t} &= -\nabla\cdot\left(\omega\mathbf{V}_{E\times B}\right)+\nabla_{||}j_{||}\\ &\quad -\nabla\cdot\left(n\mathbf{V}_{mag}-n\mathbf{V}_{co-i}-n\mathbf{V}_{cf-i}\right)+\nabla\cdot\left(\mu_i\nabla_\perp\omega\right)\end{aligned} \tag{4.40}$$

$$\begin{aligned}\frac{\partial}{\partial t}\left(nv_{||i}\right) &= -\nabla\cdot\left[nv_{||i}\left(\mathbf{V}_{E\times B}+\mathbf{V_{co-i}}+\mathbf{V_{cf-i}}\right)\right]+\nabla\cdot\left(D_nv_{||i}\nabla_\perp n\right)\\ &\quad -\partial_{||}p_e+2n\mathbf{b}\cdot\left[\left(\mathbf{V}_{E\times B}+\mathbf{V}_{co-i}+\mathbf{V}_{cf-i}\right)\times\mathbf{\Omega}_0\right]+nR\Omega_0^2\mathbf{b}\cdot\nabla R\end{aligned} \tag{4.41}$$

$$\begin{aligned}\frac{\partial}{\partial t}\left[\frac{m_e}{m_i}\left(v_{||e}-v_{||i}\right)+\frac{1}{2}\beta_e\psi\right] &= \nu j_{||}/n_e+\partial_{||}\phi-\frac{1}{n_e}\partial_{||}p_e-0.71\partial_{||}T_e\\ &\quad +\frac{m_e}{m_i}\left(\mathbf{V}_{E\times B}+\mathbf{b}v_{||i}+\mathbf{V}_{co-i}+\mathbf{V}_{cf-i}\right)\cdot\nabla\left(v_{||i}-v_{||e}\right)\end{aligned} \tag{4.42}$$

A Clebsch coordinate system is used for asymmetric simulations[165]. In terms of orthogonal toroidal coordinates (ψ,θ,ζ) these are

$$x=\psi, y=\theta, z=\zeta-\int_{\theta_0}^{\theta}\frac{B_\psi h_\theta}{B_0R}d\theta \tag{4.43}$$

In the simulations, we neglect the electron inertial effects in corrective terms in Eq.(4.38), Eq.(4.39) , Eq.(4.40) and electron rotation potential energy in Eq.(4.39) as the minor effects. All the inner boundary conditions of variables are Neumann, and the outer boundaries have Dirichlet boundary conditions. The same shifted circular equilibrium is used as it in section 3.4, evolving only toroidal number $n=0$. Fig.4.5 shows the equilibrium we used for simulation. The grid resolution is $n_\Psi=260$, $n_y=64$.

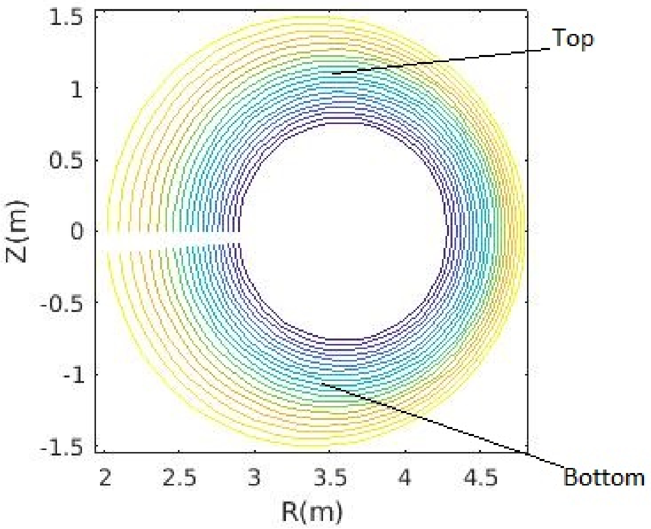

FIGURE 4.5: Sketch of shifted-circular equilibrium cbm18. The top and bottom points are locations where Fig.4.6 data is taken.

Plasma potential, vorticity, density and ion parallel velocity are obtained from the simulation. Using a new axisymmetric field solver, the resulting evolution of the parallel velocity (located at normalized $\psi = 0.6\psi_0$) is shown for two poloidal locations(top and bottom) on the same flux surface in Fig.4.6. Oscillations at the top and bottom of the plasma are out of phase, they damp with time to a quasi-steady state around 3 to 4 ms, then keep increasing slowly. The major reason for the increasing of the electrostatic potential mainly is that electric field is related to rotation in the non-inertial system(Eq.(4.19). In the later physical analysis section, an interactive relationship between parallel velocity and electrostatic potential can be seen from Eq.(4.61). Because the toroidal rotation rate is a constant number, rotation plays a role as a kind of source, contributing to the growth of velocity and potential.

From the results of simulation, we also find ZF and GAMs like structure appears in the presence of uniform toroidal rotation. As it shown in Fig.4.7, at the quasi-steady state, the parallel velocity changes from a ’frozen’ state into an alternative structure under the effects of non-inertial force and drift. The amplitude of the velocity also increase significantly compared to non-rotating simulation. In the following figures, the velocity is normalized by ion acoustic velocity

$$V_{cs} = \sqrt{\frac{\gamma_B k_B (T_i + T_e)}{m_i}} \tag{4.44}$$

where k_B is the Boltzmann constant, $\gamma_B = \frac{5}{3}$ is the ratio of specific heat capacities.

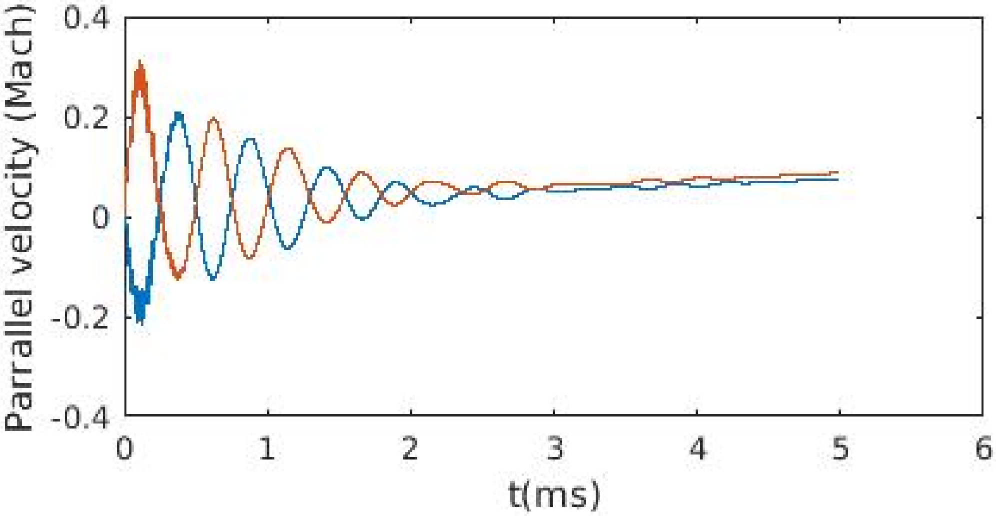

FIGURE 4.6: Evolution of the parallel velocity (located at normalized $\psi = 0.6\psi_0$) with axis toroidal rotation velocity $R_0\Omega_0 = 0.8$ *Mach*. The red line is the velocity at the top of poloidal plane, whilst the blue one is bottom

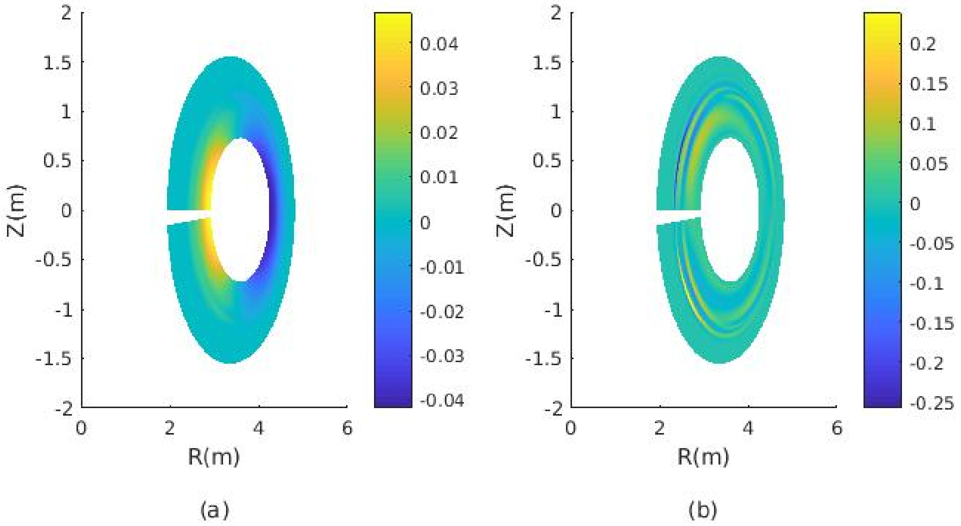

FIGURE 4.7: Parallel velocity (Units: Mach Number) on quasi-steady state without(a)and with(b) uniform rotation, the rotation velocity at axis $R_0\Omega_0 = 0.8 Mach$

In addition, the results of simulations reveal parallel flow' evolution with time. Radial spatial structure is obtained and the GAM like structure propagate across flux surfaces, shown in Fig.4.8. The harmonic oscillations grow from the core area of the equilibrium and propagate to the boundary regions.This kind of feature is quite similar to GAMs.

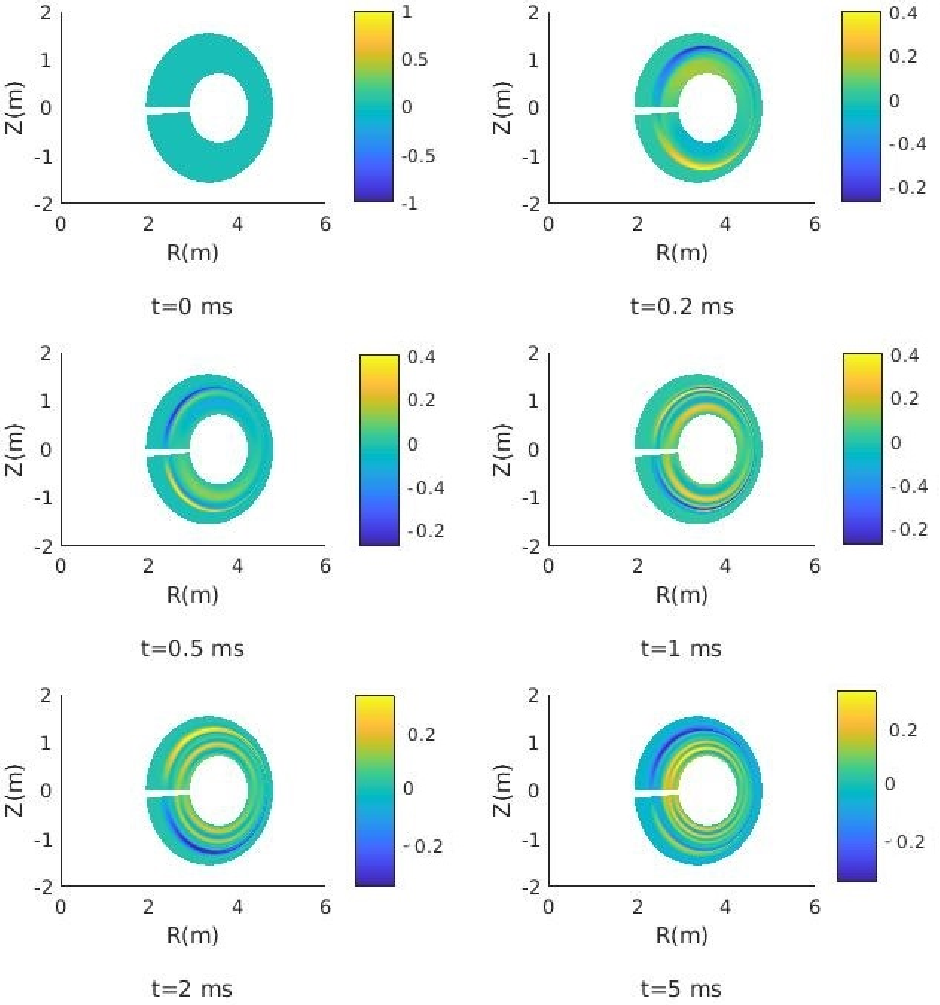

FIGURE 4.8: Time evolution of parallel flow, the rotation velocity at axis $R_0\Omega_0 = 0.8Mach$, units of velocity are Mach number

Comparing the results for different rotation rate, it is obtained that toroidal rotation rate has influence on the poloidal velocity structure, as it shown in Fig.4.9. Combined with the velocity spatial spectrum in Fig.4.10 we can also conclude that higher rotation rate decrease the poloidal mode number of parallel flow.

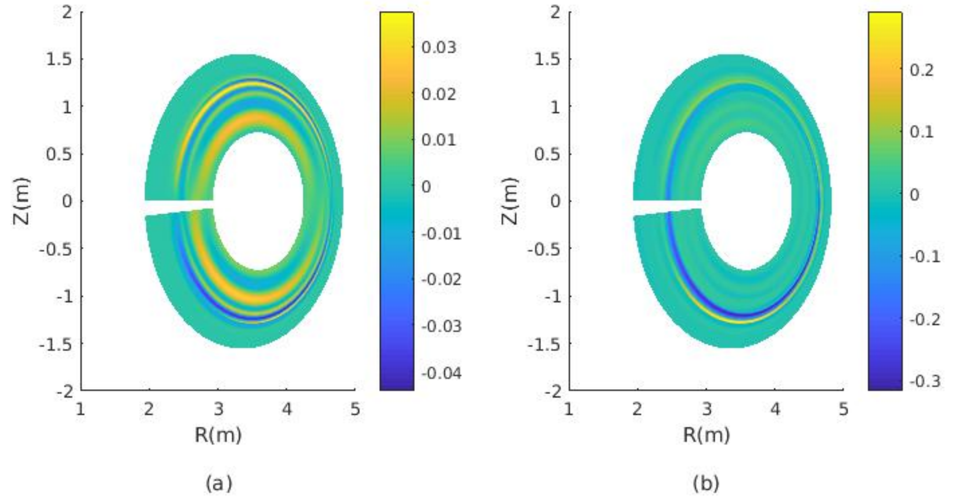

FIGURE 4.9: Parallel velocity at 5ms, with the axis toroidal rotation velocity $\Omega_0 = 0.1$ $Mach$(a) and $R_0\Omega_0 = 0.8$ $Mach$(b)

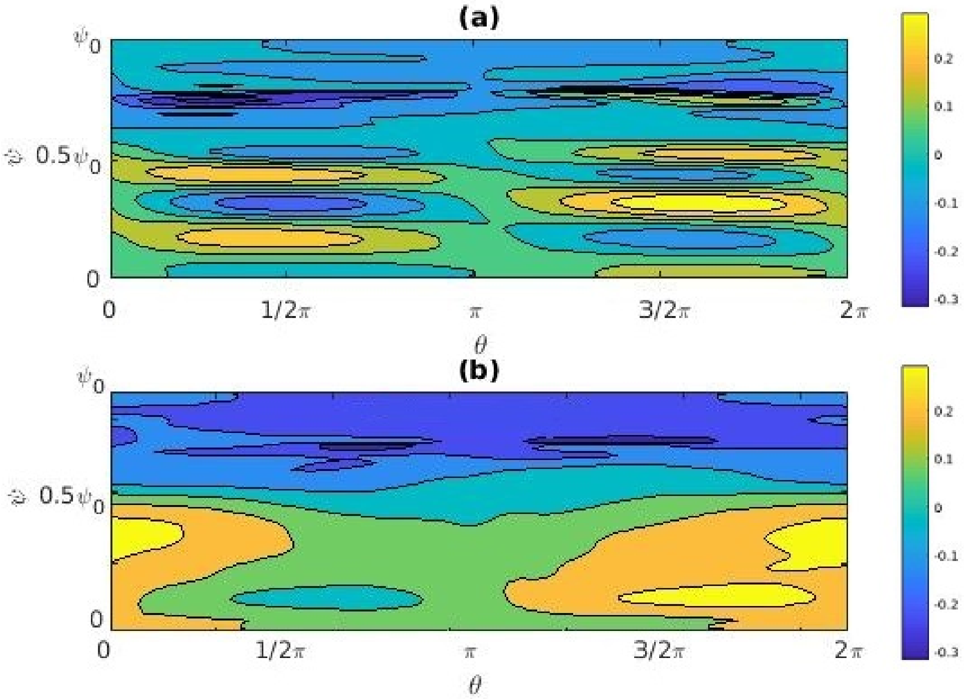

FIGURE 4.10: Spatial structure of parallel velocity at t=3ms with low and high toroidal rotation rates, figure (a) is the spectrum with axis toroidal rotation velocity $R_0\Omega_0 = 0.1$ $Mach$, and figure (b) indicates the velocity spectrum with axis toroidal rotation velocity $R_0\Omega_0 = 0.8$ $Mach$. x and y axis represents poloidal angle and normalized poloidal flux surface grids respectively. The 0 and ψ_0 indexes are inner and outer boundary.

Besides, the mean Mach numbers of parallel velocity grow continuously with the increase of toroidal rotation(Fig.4.11).

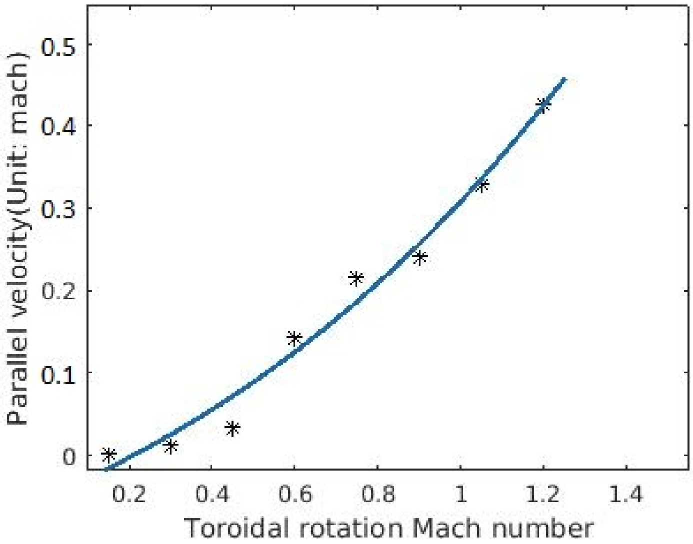

FIGURE 4.11: The growth of flux average parallel with toroidal rotation in radial position $\psi = 0.6\psi_0$

However, it is still unknown whether this kind of structure is ZF or GAMs. Here, we assume these $m \approx 0$ and $m \approx 1$ modes obtained as zonal-flow and GAM. Since both of them depend on radial electrostatic fields, we then operate spatial Fourier transform on electrostatic fields and obtain the $m \approx 0$ and $m \approx 1$ components, results are shown in Fig.4.12. From the figure, it can be concluded that the amplitude of the $m = 0$ mode is excited but its frequency is damped influenced by toroidal rotation. On the other hand, for the $m = 1$ mode, the frequency of the electrostatic field increases with the influence of non-inertial effects. Therefore, this shows that ZF and GAMs are triggered in this rotating frame. By doing a further Fourier transform in time on the above two components, we then further get the GAM frequency and ZF's amplitude (Fig.4.13), from the figure, we can conclude that the velocity of zonal flow and GAMs' frequency increase with rotation rates, but GAM damps with time.

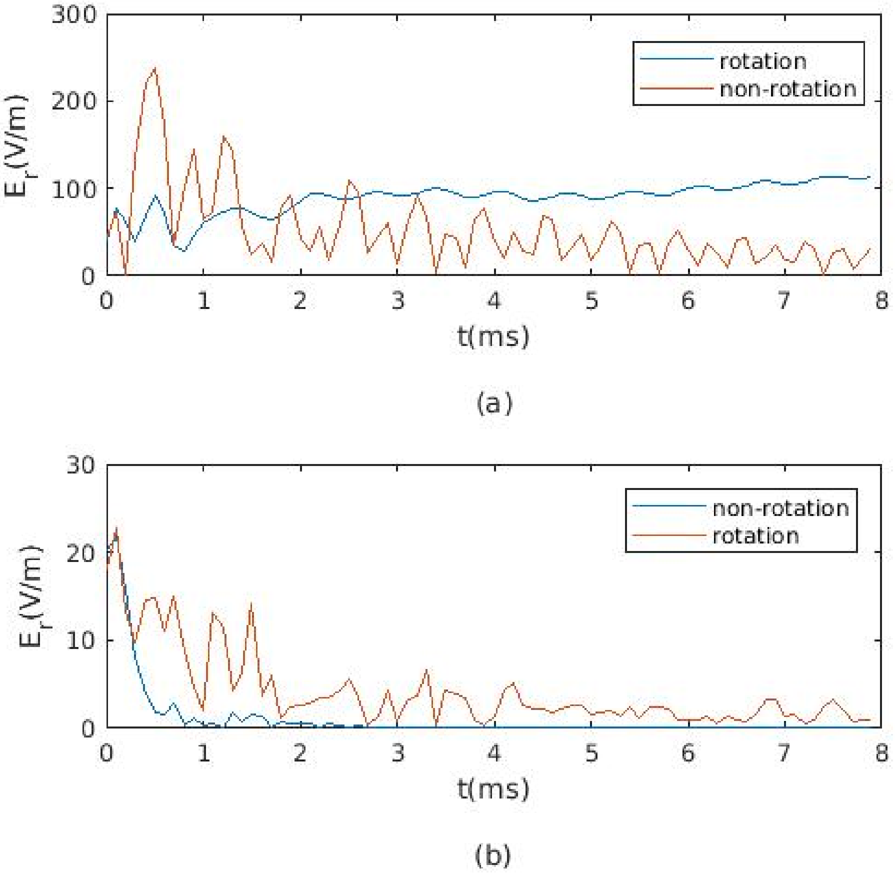

FIGURE 4.12: Time evolution of ZF m=0(a) and GAM m=1(b) radial electrostatic field

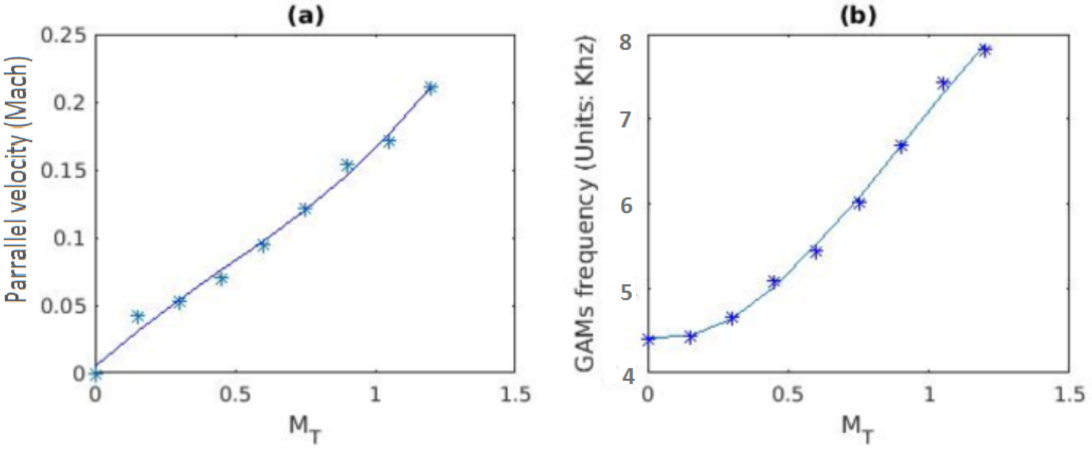

FIGURE 4.13: Velocity of $m = 0$ mean flow (a) and the frequency of (b) $m = 1$ oscillating flow for different rotation rates, M_T is the mach number of axis toroidal rotation velocity.

Since the formation of GAMs is considered as the phase difference between density and electrostatic potential[62]. Some experimental methods such as ECRH and NBI are believed to have effects on ZF and GAMs, which cause the asymmetry of poloidal density[139]. In appendix A, we developed a simple mode and verified that ECRH can trigger plasma density in-out asymmetry poloidally. In the following simulation, we run the cases with the injection of an in-out asymmetric density source (cosine), shown in Fig.4.14. It is found that asymmetric source can enhance the amplitude of oscillation but contribute to the mean of parallel flow only with the existence of toroidal rotation. As discussed in section 4.1, the injections of NBI and ECRH can induce poloidal asymmetry. Here we suggest that the influence of NBI and ECRH on ZF and GAMs are not only caused by density asymmetry but on the change of toroidal velocity profile[137].

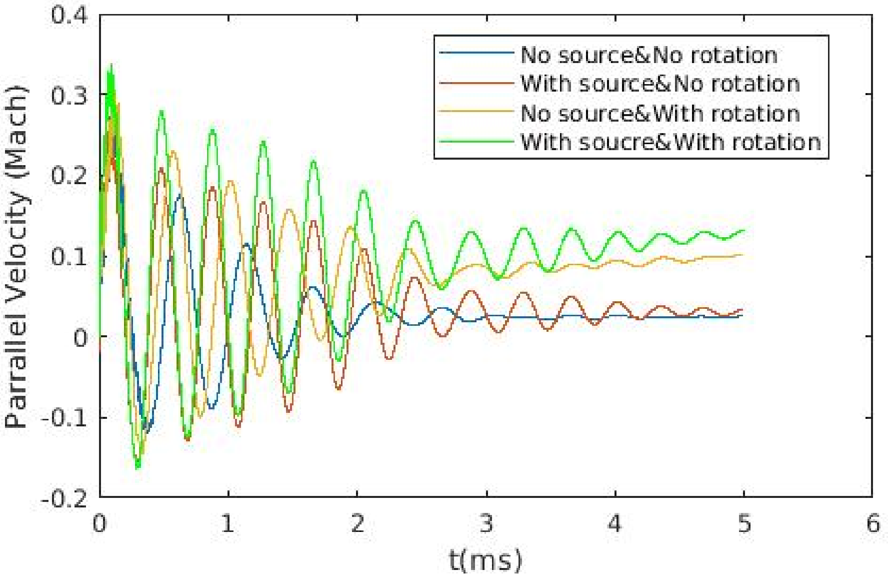

FIGURE 4.14: Parallel velocities (located at normalized $\psi = 0.6\psi_0$) with axis toroidal rotation velocity $R_0\Omega_0 = 0.8Mach$ with and without asymmetric source injection. The blue line is the velocity evolution without neither source and rotation, red line and orange line is the case of source injection and rotation separately. The green line is the result with both density source injection and toroidal rotation.

4.6 Physical explanation

To understand the mechanism of simulation results further, we use simple MHD equations to study non-inertial's effects analytically. From equations (4.27), (4.31),(4.36), we can obtain a simplified reduced MHD mode by eliminating electron momentum and diffusion terms:

$$\frac{\partial n}{\partial t} = -\nabla \cdot [n\frac{\mathbf{b}\times\nabla\phi}{B}] \tag{4.45}$$

$$\frac{\partial \Omega}{\partial t} = \nabla \cdot [p\nabla \times (\frac{\mathbf{b}}{B})] + \nabla_{||}j_{||} + \nabla \cdot (en\mathbf{V}_{co-i} + en\mathbf{V}_{cf-i}) \tag{4.46}$$

$$\begin{aligned}\frac{\partial n v_{||}}{\partial t} &= -\nabla \cdot [nv_{||}(\mathbf{V}_{E\times B} + \mathbf{V}_{co-i} + \mathbf{V}_{cf-i})] + \partial_{||}p_e \\ &+2n\mathbf{b}\cdot(\frac{\mathbf{b}\times\nabla\phi}{B} \times \mathbf{\Omega_0}) + nR\Omega_0^2\mathbf{b}\cdot\nabla R\end{aligned} \tag{4.47}$$

A common approach to solving the continuity is to use[89]:

$$\nabla \times \frac{\mathbf{b}}{B} \approx \frac{2}{B}\mathbf{b}\times\kappa \tag{4.48}$$

where κ is curvature term,and to split the $E \times B$ advection term into a divergence-free advection term, and a divergence term:

$$\frac{\partial n}{\partial t} = -\frac{1}{B}\mathbf{b}\times\nabla\phi\cdot\nabla n - n\nabla\cdot(\frac{1}{B}\mathbf{b}\times\nabla\phi) \tag{4.49}$$

then approximate

$$\nabla\cdot(\frac{1}{B}\mathbf{b}\times\nabla\phi) \approx \frac{2}{B}\mathbf{b}\times\boldsymbol{\kappa}\cdot\nabla\phi \tag{4.50}$$

In Clebsch coordinates the $E \times B$ advection term appears like[89]

$$\begin{aligned}\frac{1}{B}\mathbf{b}\times\nabla\phi\cdot\nabla n &= \frac{\partial\phi}{\partial x}\frac{\partial n}{\partial z} - \frac{\partial\phi}{\partial z}\frac{\partial n}{\partial x} \\ \frac{B_t IR}{B}(-\frac{\partial\phi}{\partial y}\frac{\partial n}{\partial z} + \frac{\partial\phi}{\partial z}\frac{\partial n}{\partial y}) &+ \frac{RB_pB_t}{B^2h_\theta}(\frac{\partial\phi}{\partial x}\frac{\partial n}{\partial y} - \frac{\partial\phi}{\partial y}\frac{\partial n}{\partial x})\end{aligned} \tag{4.51}$$

For axisymmetric flows the z derivatives(toroidal angle) are zero, so this term vanishes, leaving only the compression term. This leaves

$$\frac{\partial n}{\partial t} = -n\frac{2}{B}\mathbf{b}\times\kappa\cdot\nabla\phi \tag{4.52}$$

Starting with the density equation, we look for solutions of the form

$$
\begin{aligned}
n &= n_0 + n_1 = n_0 + n_{1,0}e^{ik_\perp x + ik_{||2}y - i\omega t} \\
\phi &= \phi_0 + \phi_1 = \phi_0 + \phi_{1,0}e^{ik_\perp x + ik_{||1}y - iwt} \\
v_{||} &= v_{||0} + v_{||1} = v_{||0} + v_{||1,0}e^{ik_\perp x + ik_{||2}y - i\gamma t}
\end{aligned}
\tag{4.53}
$$

Linearising equation (4.52), assuming a simple circular cross-section, large aspect-ratio, and keeping only the poloidal flow

$$\mathbf{b} \times \boldsymbol{\kappa} \cdot \nabla \rightarrow \frac{1}{R} sin\theta \frac{\partial}{\partial x} \tag{4.54}$$

we get

$$n_{1,0} = n_0 \frac{2k_\perp}{BR\omega} sin\theta \phi_{1,0} \tag{4.55}$$

Then the linearised form of Eq.(4.47) becomes

$$
\begin{aligned}
-i\gamma v_{||1} = {} & \frac{m_i R^2 \Omega_0^2 B_p B_t}{eB^2 h_\theta}\left(\frac{Bh_\theta}{B_p} ik_\perp v_{||1} sin\theta - \frac{B}{RB_p^2} ik_{||2} v_{||1} cos\theta\right) \\
& + \frac{2m_i v_{||0} k_\perp R \Omega_0^2 B_p B_t \phi_1}{e\omega B^3 h_\theta}\left(\frac{Bh_\theta}{B_p} ik_\perp sin^2\theta - \frac{B}{RB_p^2} ik_{||1} sin\theta cos\theta\right) \\
& - \frac{2im_i \Omega_0 k_\perp v_{||0}}{eB} v_{||1} sin\theta - \frac{v_{||1} m_i \Omega_0^2}{e} sin\theta cos\theta + eT_0 \frac{2ik_\perp k_{||1}}{rBR} \phi_1 sin\theta \\
& - \frac{2in_0 v_{||0} k_\perp}{BR\omega} \phi_1 sin\theta + 2i\Omega_0 \phi_1 k_\perp \sin\theta - \frac{2\phi_1 \Omega_0^2 k_\perp}{B_p \omega} sin^2\theta
\end{aligned}
\tag{4.56}
$$

The first two terms of Eq.(4.56) apply Eq.(4.51)'s rule

$$n\frac{m_i R \Omega_0^2}{eB} \mathbf{b} \times \nabla R \cdot \nabla V_{||} = n \frac{m_i R \Omega_0^2}{eB} \frac{RB_p B_t}{Bh_\theta}\left(\frac{\partial R}{\partial x}\frac{\partial V_{||}}{\partial y} - \frac{\partial V_{||}}{\partial x}\frac{\partial R}{\partial y}\right) \tag{4.57}$$

Where

$$\frac{\partial R}{\partial x} = -\frac{BR}{R^2 B_p^2}\frac{dZ}{ds}, \frac{\partial R}{\partial y} = \frac{Bh_\theta}{B_p}\frac{dR}{ds} \tag{4.58}$$

s is the distance along the field line. Since vorticity is approximately:

$$\Omega = \frac{m_i n_0}{B_0^2} \nabla_\perp^2 \phi \tag{4.59}$$

Then we can rewrite the vorticity equation into a linearized form:

$$\begin{aligned} i\omega k_\perp^2 \frac{m_i}{B^2}\phi_1 = 4\frac{ik_\perp^2 eT_0}{\omega B^2 R^2}\phi_1 sin^2\theta + \frac{2k_\perp h_\theta m_i \Omega_0^2}{\omega R B^2}\phi_1 sin\theta cos\theta \\ + \frac{2m_i k_\perp R\Omega_0^2 B_t \phi_1}{\omega B^2 h_\theta}(-ih_\theta k_\perp sin^2\theta + \frac{1}{RB_p} ik_{||1} sin\theta cos\theta) \\ -2\frac{i\Omega_0 m_i k_\perp h_\theta}{B} v_{||1}(BRk_\perp sin\theta + k_{||2} cos\theta) + \nabla_{||} j_{||} \end{aligned} \tag{4.60}$$

To remove the parallel current term from the vorticity equation, average over a flux surface by defining $<\cdot>=\oint \cdot d\theta$ for large aspect ratio. When $k_1 \approx 0, k_2 \approx 0$, we obtain a simple equation operating on Eq.(4.56) and Eq.(4.60):

$$i\gamma v_{||1} = \frac{h_\theta \Omega_0^2 k_\perp}{B_p \omega}\phi_1 \tag{4.61}$$

Eq.(4.61) gives the expression of ZF's ($k_1 \approx 0, k_2 \approx 0$) growth rate. When the perturbation frequencies damps (ω=imaginary values), the parallel velocity can rise with the electrostatic potential. On the other hand, parallel velocity also contribute to the potential. That helps to explain why the potentials keep increasing at the end of the simulation instead of becoming horizontal in Fig.4.7. When $k_1 \approx 0, k_2 \approx 1$, we obtain GAM component of Eq.(4.60):

$$\omega k_\perp^2 < \phi_1 > \frac{m_i}{B^2} = \frac{2eT_0 k_\perp^2}{\omega B^2 R^2} < \phi_1 > - \frac{m_i R\Omega_0^2 B_t k_\perp^2}{\omega B^2} < \phi_1 > \tag{4.62}$$

Most terms cancel, leaving

$$\omega^2 = \frac{eT_0}{m_i}\frac{2}{R^2} - R\Omega_0^2 B_t \tag{4.63}$$

Using the same method, we obtain the equations from Eq.(4.56) and Eq.(4.60)

$$\frac{m_i R^2 \Omega_0^2 B_p B_t}{eB^2 h_\theta}\frac{Bh_\theta}{B_p} ik_\perp v_{||1,0} \exp(-i\gamma t) = -\frac{2\phi_{1,0}\Omega_0^2 k_\perp}{B_p \omega}\exp(-i\omega t) \tag{4.64}$$

$$i\omega k_\perp^2 \frac{m_i}{B^2}\phi_{1,0}\exp(-i\omega t) = 2\frac{ik_\perp^2 eT_0}{\omega B^2 R^2}\phi_{1,0}\exp(-i\omega t) + m_i R\Omega_0 B k_\perp^2 v_{1,0}\exp(-i\gamma t) \tag{4.65}$$

Applying Eq.(4.64) into Eq.(4.65),we obtain

$$v_{1,0}exp(-i\gamma t) = \frac{2ieB}{m_i \omega B_p B_t R^2}\phi_{1,0}\exp(-i\omega t) \tag{4.66}$$

$$\omega^2 = \frac{eT_0}{m_i}\frac{2}{R^2} + \frac{2e\Omega_0 B^4}{m_i B_p B_t R} \tag{4.67}$$

From the equations, we find that centrifugal force and drift contribute to the growth of parallel velocity and damping of the GAM, this result is qualitatively similar to Casson's work[166]. On the other hand, the synergistic effect of centrifugal drift and Coriolis drift increase the frequency of GAM and make this kind of $m = 1$ structure propagate in the radial direction. This agree qualitatively with the results seen in Fig.4.13.

Due to the gradient of the potential perturbation, the density perturbation is surrounded by an $\mathbf{E} \times \mathbf{B}$ drift vortex. Since the density is not homogeneous, the component of the corresponding particle flux parallel to the density gradient has a divergence leading to an increase of the initial perturbation where $\mathbf{V_E}$ is antiparallel to n and to a decrease where $\mathbf{V_E}$ and ∇n are parallel. Consequently, the divergence of the $\mathbf{E} \times \mathbf{B}$ flow leads to a motion of the initial perturbation perpendicular to the magnetic field and the density gradient. In the absence of ion pressure gradient, Coriolis drift plays a similar role as ion diamagnetic drift, which contributes to the radial propagation of GAM[125].

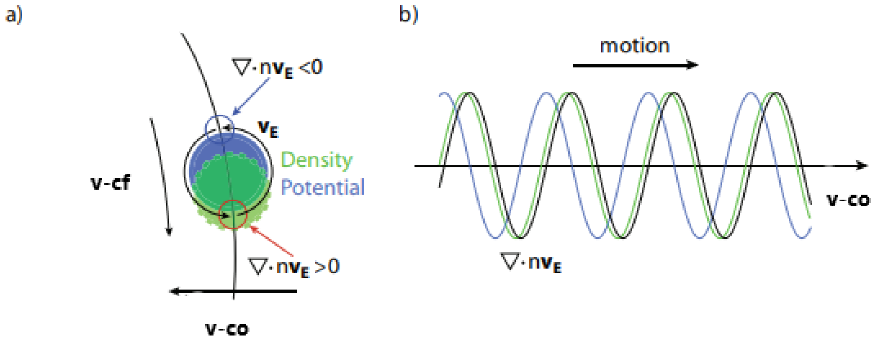

FIGURE 4.15: a) Density and potential perturbations are phase shifted such that the maximum of the density perturbation is close to the maximum of the divergence of the $\mathbf{E} \times \mathbf{B}$ particle flux. Therefore, the initial perturbation is continuously fed by the $\mathbf{E} \times \mathbf{B}$ flow, centrifugal drift can reduce this phase flow and Coriolis drift makes perturbations to propagate in radial direction. b) One-dimensional picture. Density and potential are in phase. The divergence of the $\mathbf{E} \times \mathbf{B}$ particle flux along with Coriolis velocity causes the potential and density fluctuations to move.

4.7 Further discussion and preliminary experiment results

Based on Hsu's[140] model, the injection of ECW can induce the growth of electrostatic potential, which cause the density perturbation. We obtain permission to use the data and design experiments on HL-2A. In the shot 31193, the radial and poloidal potential are measured with the injection of Electron cyclotron waves (ECW). The deposition point of ECW locates in the 0.6 normalized flux surface; the data is collected from 0.95 normalized surface. Basic parameters of shot 31193 (Fig.4.16) are as follows: plasma current is about $150MA$, line-average electron density is about $2 \times 10^{19} m^{-3}$, the toroidal magnetic field on axis is about $1.3T$.

The injections of RCRH and neutral beam are shown in Fig.4.16(b) where the curves demonstrate the powers of NBI and ECRH versus time. The power of NBI and ECW wave are around $800KW$ and $600KW$ respectively. The injection time of NBI exists from $500ms$ to $1100ms$ and the $68GHz$ ECRH is from $700ms$ to about $900ms$.

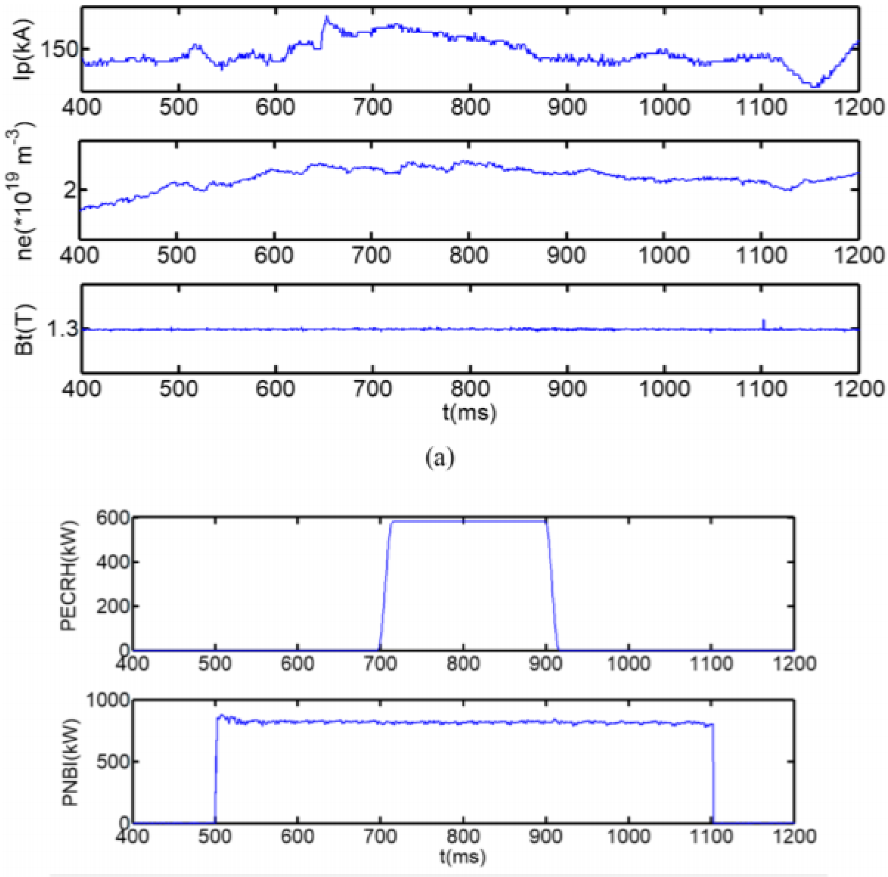

(a)

(b)

FIGURE 4.16: (a)The experiment parameters and (b)the injection of eletron cyclotron resonance wave and neutral beam in shot 31193 of HL-2A [167]

Langmuir probe is used to detected the poloidal and radial potential on 0.95 normalized flux surface (midplane of LFS). The structure of Langmuir probe is as illustrated in Fig.4.17.

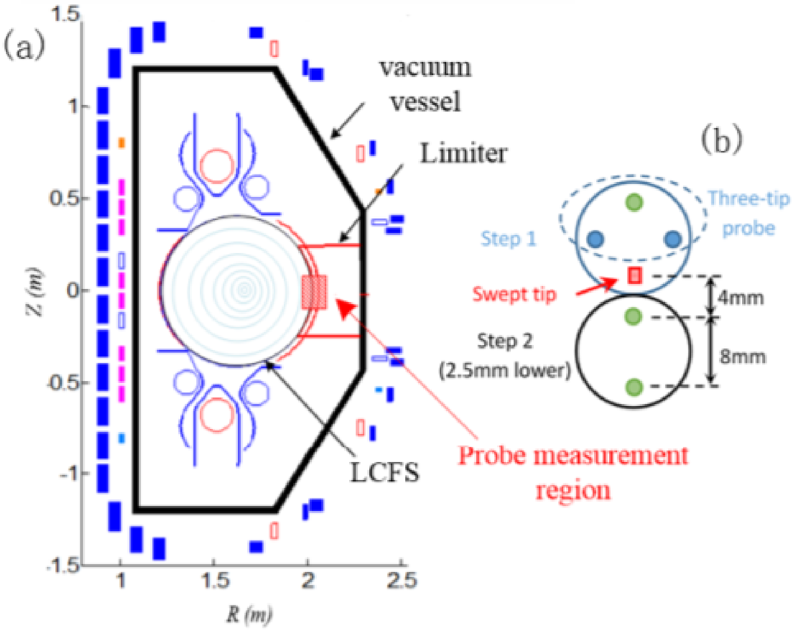

FIGURE 4.17: (a) The configurations of HL-2A in this shot (b) multi-functional probe array arrangement, which contains: voltage swept probe tip (red), double probe (blue) and floating potential tips (green).

[168]

In the experiment, we use the blue probes to evaluate the poloidal Electric field, while the potential difference of green ones is used to calculate radial field[167]. Then the time evolution of poloidal and radial electric field in mid plane is obtained.

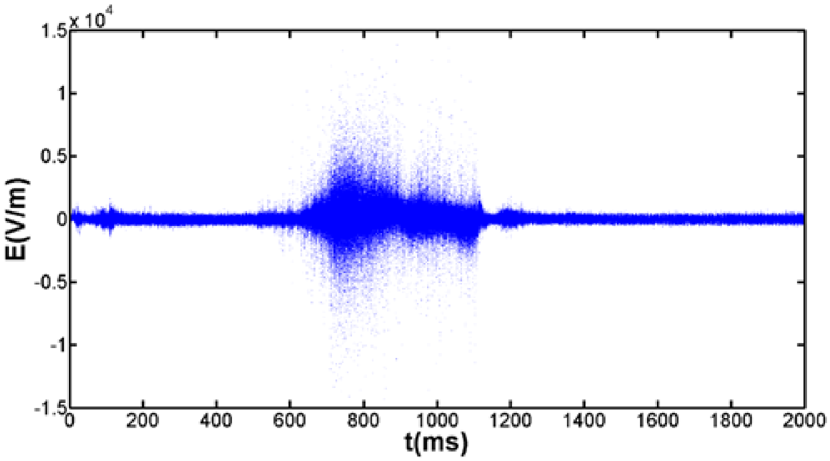

FIGURE 4.18: The change of poloidal potential during the process of ECW injection (shot 31193)

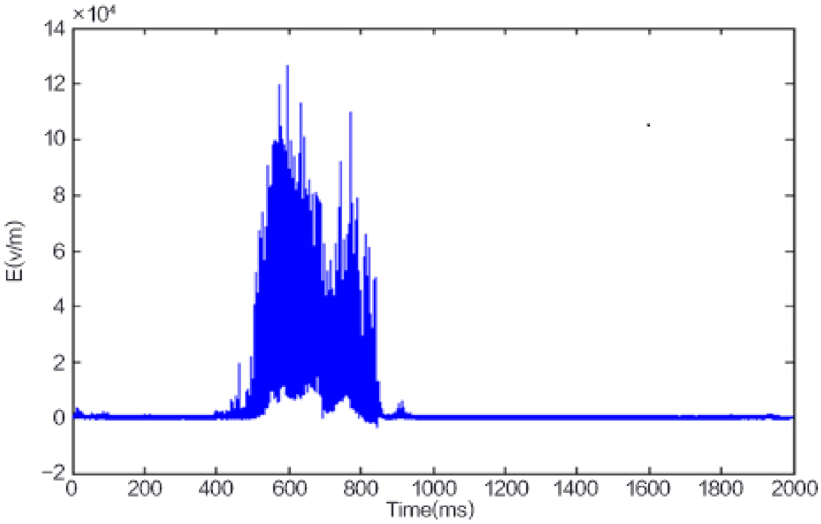

FIGURE 4.19: The change of radial electric field during the process of ECW injection (shot 31193)

From the data of Fig.4.18 and Fig.4.19, it is obvious that during the injection process of ECW, both the poloidal and radial potential increase severely during the process and decrease after the injection of ECW. To obtain the major components of the oscillations, we do Fourier transform on radial and poloidal electric field, in the periods of time $500ms - 700ms$ (before ECRH) and $700ms - 900ms$ (with ECRH) respectively. The spectra of electric oscillations are shown in Fig.4.20.

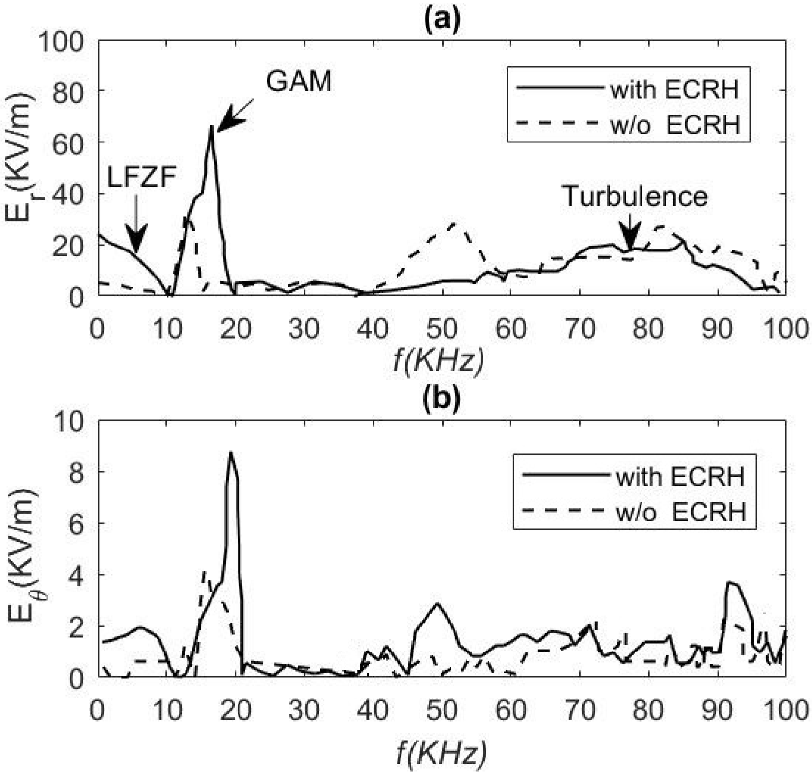

FIGURE 4.20: Amplitude frequency diagrams of (a)radial and (b)poloidal electric oscillations with(solid lines) and without(dashed lines) the injections of ECRH.

Obtaining from Fig.4.20(a), low frequency components of the radial electric field, with the frequencies of $< 10KHz$ and $\approx 17KHz$, are enhanced significantly by ECRH. In HL-2A, the typical frequency of LFZF(low frequency zonal flow) is $< 4KHz$, and GAM frequency is about $7KHz - 20KHZ$[169, 170]. At the same time, turbulence components (identified as $20KHz - 100KHz$ parts[170]) are mitigated slightly. It can be also seen from Fig.4.20(a) that ECRH can increase the GAM frequency ($13KHz$ without ECRH). Similar results are also reported in Previous work of other scholars[169, 171]. From Fig.4.20(b), similar effects on poloidal electric field are obtained: ECRH can cultivate low frequency electric fields effectively.

Those mentioned above observations in the experimental analysis have agreements with our simulation results qualitatively. From simulations, we find that the amplitude of ZF and electrostatic potential rise with the toroidal rotation rate. While ECRH is proved to have great relevance with toroidal rotation rates[129, 137]. Therefore, the non-inertial effects can be one of the possible reasons in the explanations of GAMs and ZFs excited by ECRH.

The limitation is that only one probe was applied during the experiment, the next stop of the experiments evolve more probe in different positions with the injection of ECW, which could obtain the data of plasma velocity and potential difference in different positions.

From the preliminary experimental results, it may be possible to explore ECRH's effect's on GAM, ZF and rotation in the next step.

4.8 Summary and discussion

To summarize, in this chapter, drift-ordered 2-fluid equations have been developed from the collisional Vlasov equation in a non-inertial rotating frame, under the cold ion assumption. Implementing this model into the Hermes code, we performed simulations with setting toroidal mode number $n = 0$. GAMs and ZF flow structures are then obtained from the results, under the centrifugal and Coriolis effects. The harmonic oscillations of momentum are found to grow from the core area of the equilibrium and propagate to the boundary regions. The results also indicate that amplitude of ZF and GAM frequency grows with toroidal rotation, the result is in agreement with Wangs work[13].

We also develop a simple analytic modes to verify the simulation results and explore the physics of ZF and GAMs in a non-inertial system. It is found that centrifugal force and drift contribute to the growth of parallel velocity and damping of the GAM . On the other hand, the synergistic effect of centrifugal drift and Coriolis drift increase the frequency of GAM and make this kind of $m = 1$ structure propagate in the radial direction. In most studies of rotation's effects on ZF and GAM[130, 157], the effects of toroidal rotation are regarded as convection flow or centrifugal drift flow. However, all non-inertial terms, including Coriolis effects, need to be considered when applying centrifugal drift. This work suggests that the phase difference between parallel momentum and electrostatic potential can also trigger GAMs. In the absence of ion magnetic drift (cold ion mode), the Coriolis convection plays a vital role in GAM radial propagation ZF's global structure.

In most previous studies, the ITG is considered as an important role of exciting ZF, especially under the situation of arbitrary heating[62, 172]. But the experiments on ASDEX-U prove that ion temperature profile change a bit during the process of ECRH[137], which has little effects on ITG. Therefore, it is reasonable to use cold ion model to simulate the physics of this flows. Then we guess that the changes of rotation profile and parallel plasma distribution may be one of the reasons influencing ZF and GAMs during the heating process. From the results in Fig.4.14, asymmetric density sources are proved to have effects on amplitude and phase of GAMs or ZFs, which can be induced by ECRH[129, 139]. Combined with the previous theories and preliminary experimental results, it is possible to explore ECRH's effects on GAM and ZF.

However, there are some limitations of those cold ion simulations. The ion magnetic drift, which is considered as the one of the main contributions of GAMs and ZFs, is vanished in cold ion model. The ion viscosity and heat flux terms are not concluded in this model since the ion temperature is set to zero. In the future work, hot ion model will be applied to study rotation's effects.

Chapter 5

Plasma rotation and flows effects on ELMs

Previous work on plasma rotation's effects on ELMs mostly focuses on the advection terms in the inertial system. Some results of BOUT++ simulations show that only shear $\mathbf{E} \times \mathbf{B}$ flow has a clear influence on ELM [19, 123]. These studies reveal that shear flow can reduce ELM growth rate and suppress ELM size. On the other hand, Kelvin-Helmholtz instability caused by shear flow destabilizes low n P-B mode. However, equilibrium $\mathbf{E} \times \mathbf{B}$ flow in those work is treated as an additional term rather than self-consistent with equilibria. And it is still interesting to study flow and plasma rotation's effects on ELM. In this chapter, 4-field reduced-MHD equations are derived from collision-less Vlasov equation in a non-inertial rotating frame, new terms include both centrifugal and Coriolis effects. Based on this model, simulation results show rigid rotation can also mitigate P-B instabilities with consideration non-inertial terms. Our results indicate that non-inertial effects should be taken into consideration in ELM studies. In the previous studies, the P-B instability studies generally focus on the radial characteristics of pressure profiles, the results of this chapter suggest that poloidal structure or parallel structure of pressure is also important.

5.1 A brief review of studies of plasma rotation effects on ELMs

As was reviewed in chapter 1 and chapter 4, shear flows at the plasma edge are believed to play an essential role in L-H transitions and the H-mode pedestal. In the experiments, toroidal rotation is believed to lead to poloidal rotation and cause its shear at the edge to increase significantly[173]. At the same time, many experiments support the hypothesis that ELMs are stongly influenced by shear flows[34, 174]. In experiments on JT-60, toroidal rotation was found to have effects on both ELM size and frequency[34], shown in Figure.5.1. Experimental work on KSTAR also suggests stabilization of pedestal instabilities due to toroidal rotation[33]. In addition, the energy losses of ELMs have been shown to be reduced by counter current direction NBI heating in JT-60U[34] and DIII-D [35].

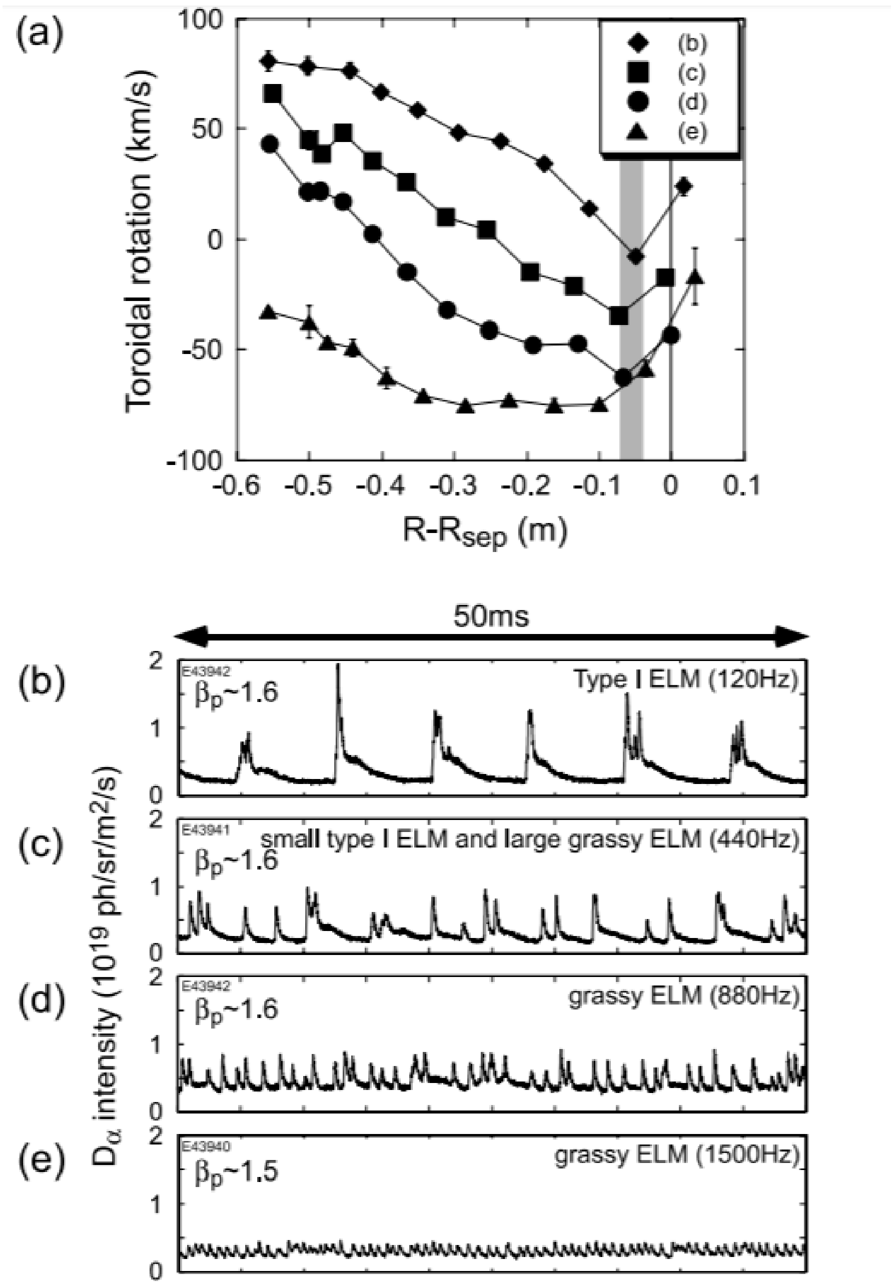

FIGURE 5.1: (a)Toroidal rotation profiles at the LFS of midplane, the zero point on x axis of (a) is the location of peak density. The scan regime is $q95 \approx 4.7 - 6.3$. (b-e)The identities(D_α) of ELMs frequency and energy loss with different toroidal rotation velocities on JT-60.

[34] .

From the results of Fig.5.1, we can find that larger counter toroidal rotation rates lead to smaller ELM size but higher frequency. The reason for rotation's mitigation effect can be the sign or absolute value of velocity instead of its shear. In the same experiment, no edge fluctuations were observed, which means turbulence makes little effect. However, the mechanism is still not fully understood, each theoretical model can find some support from the experiments[174]. Generally, critical flow shears at the edge are believed to mitigate ELMs. Waelbroeck[175] suggested that the flow shear has a stabilizing effect on high-n ballooning modes in a circular tokamak equilibrium. In the latter study, high-n peeling ballooning mode was addressed can also be stabilized by flow shear and toroidal rotation rotation[176]. Further simulation work using ELITE examined the effects of flow shear and toroidal rotation on ideal peeling-ballooning mode[55]. Later simulation studies using BOUT++ studied the influence of toroidal rotation shear on nonideal P-B mode, such as ion diamagnetic effects and the resistivity[19, 123]. Both linear and non-linear results demonstrate that the shear of parallel equilibrium flows can both stabilize P-B mode and destabilize ELM by driving Kelvin-Helmholtz instabilities.

However, the experiment results on JT-60[34] find that for grassy ELMs, the sign or the amplitude is the main cause of ELM energy suppression, rather than the shear of rotation. In addition, the supposed equilibrium shear flow or rotation in previous BOUT++ simulations was generated by imposing an electric field or velocity shear, the severe impacts of this electric or velocity shear on equilibrium and pressure profiles are neglected. In some other work, the shear flows are regarded as centrifugal drift velocities[55], which only exist in the non-inertial system. Therefore, it is needed to develop a self-consistent model for the influence of rotation on ELMs. Treating previous approaches toroidal rotation as a rotation frame in the non-inertial system, problems can be avoided. In this section, we will develop a self-consistent MHD model in the rotating frame to explore the effects of toroidal rotation and flow shear on ELMs.

5.2 Reduced single MHD model in rotating frame

Neglecting the collisional operater, we can obtain the Vlasov equation in non-inertial system:

$$\frac{\partial f_a}{\partial t}+\mathbf{v}_*\cdot\nabla f_a+\frac{e_a}{m_a}\left(\mathbf{E}_*+\mathbf{v}_*\times\mathbf{B}-2\frac{m_a}{e_a}\mathbf{\Omega_0}\times\mathbf{v}_*+\frac{1}{2}\frac{m_a}{e_a}\nabla\Omega_0^2R^2\right)\cdot\frac{\partial f_a}{\partial\mathbf{v}_*}=0 \quad (5.1)$$

Taking the integration over Eq.5.1 with zero, first and second momentum. We can obtain similar fluid equations:

$$\frac{\partial n_j}{\partial t} + \nabla \cdot n_j \mathbf{V_j} = 0 \tag{5.2}$$

the momentum conservation equation,

$$\begin{aligned}\frac{\partial m_j n_j \mathbf{V_j}}{\partial t} + \nabla p_j + \nabla \cdot (\overleftrightarrow{\pi} + m_j n_j \mathbf{V_j}\mathbf{V_j}) &= Z_j e n_j (\mathbf{E} + \mathbf{V_j} \times \mathbf{B}) \\ &+ 2 m_j n_j \mathbf{V_j} \times \mathbf{\Omega_0} + m_j n_j R \Omega_0^2 \nabla R\end{aligned} \tag{5.3}$$

and the energy conservation equation,

$$\begin{aligned}&\frac{\partial}{\partial t}(\frac{3}{2}p_j + \frac{1}{2}m_j n_j V_j^2) + \nabla \cdot \mathbf{Q_j} \\ &= \mathbf{V_j} \cdot (Z_j e n_j \mathbf{E} + m_j n_j R \Omega_0^2 \nabla R)\end{aligned} \tag{5.4}$$

where the $S_j^n, \mathbf{S_j^M}, S_j^e$ are density, momentum and energy sources for species j, respectively. Followed the method in plasma textbook[4], we obtain single fluid momentum equation combining Eq.3.44 and Eq.5.3,with neglecting plasma viscosity:

$$\rho \frac{\partial \mathbf{V}}{\partial t} + \rho \mathbf{V} \cdot \nabla \mathbf{V} = \nabla P + \mathbf{J} \times \mathbf{B} + 2\rho \mathbf{V} \times \mathbf{\Omega_0} + \rho R \Omega_0^2 \nabla R \tag{5.5}$$

Then we take $\frac{e_e}{m_e} M_e + \frac{e_i}{m_i} M_i$ to get Ohm's law:

$$\begin{aligned}\mathbf{E} + \mathbf{V} \times \mathbf{B} = &-\frac{m_e m_i}{e_e e_i} \frac{\partial}{\partial t}\left(\frac{\mathbf{J}}{\rho}\right) + \frac{1}{\rho}\left(\frac{m_i}{e_i} + \frac{m_e}{e_e}\right)\mathbf{J} \times \mathbf{B} \\ &- \left(\frac{e_e}{m_e}\nabla p_e + \frac{e_i}{m_i}\nabla p_i\right)\frac{m_e m_i}{\rho e_e e_i} + 2\frac{m_e m_i}{e_e e_i \rho}\mathbf{J} \times \mathbf{\Omega_0}\end{aligned} \tag{5.6}$$

where M_e and M_i are electron and ion species of momentum equation. In the quasi-neutral assumption, the contribution of centrifugal force turns to zero. Then the parallel Ohm's law can be obtained by dotting $\mathbf{b}$ on both sides of Eq.5.6.

$$E_{||} = -\left(\frac{e_e}{m_e}\nabla_{||} p_e + \frac{e_i}{m_i}\nabla_{||} p_i\right)\frac{m_e m_i}{\rho e_e e_i} + 2\frac{m_e m_i}{e_e e_i \rho}\mathbf{J} \times \mathbf{\Omega_0} \cdot \mathbf{b} \tag{5.7}$$

Where the electron inertia term $-\frac{m_e m_i}{e_e e_i}\frac{\partial}{\partial t}\left(\frac{\mathbf{J}}{\rho}\right)$ and hall term $\frac{1}{\rho}\left(\frac{m_i}{e_i} + \frac{m_e}{e_e}\right)\mathbf{J} \times \mathbf{B}$ are neglected for low engough frequency. Following the same process, we can get the MHD version of energy conservation equation:

$$\frac{\partial}{\partial t}\left(\frac{3}{2}+\frac{1}{2}\rho V^2\right)+\frac{5}{2}\nabla\cdot(p\mathbf{V})+\frac{1}{2}\nabla\cdot(\rho V^2\mathbf{V})=\mathbf{J}\cdot\mathbf{E}+\rho R\Omega_0^2\mathbf{V}\cdot\nabla R \tag{5.8}$$

Combining Eq.5.2 and Eq.5.3, we can find that:

$$\frac{\partial}{\partial t}\left(\frac{1}{2}\rho V^2\right)+\nabla\cdot\left(\frac{1}{2}\rho V^2\mathbf{V}\right)+\mathbf{V}\cdot\nabla p=\mathbf{V}\cdot\mathbf{J}\times\mathbf{B}+\rho R\Omega_0^2\mathbf{V}\cdot\nabla R \tag{5.9}$$

where in the view of Ohm's law with neglecting electron inertia term, hall term and diamagnetic contribution:

$$\mathbf{V}\cdot\mathbf{J}\times\mathbf{B}=\mathbf{J}\cdot\mathbf{E} \tag{5.10}$$

Hence:

$$\frac{\partial}{\partial t}\left(\frac{1}{2}\rho V^2\right)+\nabla\cdot\left(\frac{1}{2}\rho V^2\mathbf{V}\right)+\mathbf{V}\cdot\nabla p=\mathbf{J}\cdot\mathbf{E}+\rho R\Omega_0^2\mathbf{V}\cdot\nabla R \tag{5.11}$$

Substituting this result into Eq.5.9, energy conservation equation is obtained:

$$\frac{dp}{dt}+\frac{5}{3}p\nabla\cdot\mathbf{V}=0 \tag{5.12}$$

The expression is the same as that in non-rotating system, which illustrates rotation does not contribute to internal energy. Following the same derivation process of shear-Alfven's law[89], we obtain the vorticity equation using of tensor identity and taking $\mathbf{b}\cdot\nabla\times$ and the curvature term gives:

$$b\cdot[\nabla\times\mathbf{f}-2\boldsymbol{\kappa}\times\mathbf{f}]\simeq\rho\frac{dU}{dt}$$

where U is the parallel component of vorticity:

$$U\equiv\mathbf{b}\cdot\nabla\times\mathbf{V} \tag{5.13}$$

$$\begin{aligned}\rho\frac{dU}{dt}&=B^2\mathbf{B}\cdot\nabla\left(\frac{J_{||}}{B}\right)+2\mathbf{b}\times\boldsymbol{\kappa}\cdot\nabla P\\&+2\rho\mathbf{b}\cdot\nabla\times(\mathbf{V}\times\mathbf{\Omega_0})+\rho R\Omega_0^2\mathbf{b}\cdot\nabla\times\nabla R\end{aligned} \tag{5.14}$$

Since $\nabla \times (\nabla F) = 0$ for any scalar F, the last term of RHS of the vorticity equation turns to zero. The Coriolis term can be written as:

$$\mathbf{B} \cdot \nabla \times (\mathbf{V} \times \mathbf{\Omega_0}) = \nabla \cdot [(\mathbf{V} \times \mathbf{\Omega_0}) \times \mathbf{B}] + (\mathbf{V} \times \mathbf{\Omega_0}) \cdot (\nabla \times \mathbf{B}) \tag{5.15}$$

based on the identity $\nabla \cdot (\mathbf{F} \times \mathbf{G}) = \mathbf{G} \cdot (\nabla \times \mathbf{F}) - \mathbf{F} \cdot (\nabla \times \mathbf{G})$. Note that $\nabla \times \mathbf{B} \ = \mu_0 \mathbf{J}$ and thus

$$(\mathbf{J} \times \mathbf{B}) \cdot (\nabla \times \mathbf{B}) = \frac{1}{\mu_0} (\mathbf{J} \times \mathbf{B}) \cdot \mathbf{J} = 0 \tag{5.16}$$

Thus,

$$\begin{aligned} \mathbf{B} \cdot \nabla \times (\mathbf{V} \times \mathbf{\Omega_0}) &= \nabla \cdot [(\mathbf{V} \times \mathbf{\Omega_0}) \times \mathbf{B}] \\ = \nabla \cdot [-\mathbf{B} \times (\mathbf{V} \times \mathbf{\Omega_0})] &= \nabla \cdot [-\mathbf{V} (\mathbf{B} \cdot \mathbf{\Omega_0}) + \mathbf{\Omega_0} (\mathbf{V} \cdot \mathbf{B})] \\ &= \nabla \cdot \left[-B\Omega_{0||}\mathbf{V} + BV_{||}\mathbf{\Omega_0}\right] \\ &= -\mathbf{V} \cdot \nabla(B\Omega_{0||}) + \mathbf{\Omega_0} \nabla(BV_{||}) \end{aligned} \tag{5.17}$$

The terms $-B\Omega_0 \nabla \cdot \mathbf{V}$ and $BV_{||} \nabla \cdot \mathbf{\Omega_0}$ are eliminated since

$$\begin{aligned} \nabla \cdot \mathbf{V} &= 0; \\ \nabla \cdot \mathbf{\Omega_0} &= \nabla \cdot \boldsymbol{\nabla} \times \mathbf{u} = 0 \end{aligned}$$

where u is the uniform toroidal rotation velocity. Then we can obtain the vorticity equation by substituting Eq.5.17 into Eq.5.14:

$$\begin{aligned} \rho \frac{dU}{dt} &= B^2 \mathbf{b} \cdot \nabla \left(\frac{J_{||}}{B} \right) + 2\mathbf{b} \times \boldsymbol{\kappa} \cdot \nabla P \\ &- \frac{\rho}{B_0} \mathbf{V} \cdot \nabla(B\Omega_{0||}) + \frac{\rho}{B_0} \mathbf{\Omega_0} \nabla(BV_{||}) \end{aligned} \tag{5.18}$$

In the drift ordering, the perpendicular velocity is the drift velocity[89],so:

$$\begin{aligned} \mathbf{V}_{\perp} \simeq & \frac{1}{B^2} \mathbf{B} \times \nabla \phi + \frac{1}{en} \frac{1}{B^2} \mathbf{B} \times \nabla P \\ & + \frac{2\rho V_{||}}{enB} \mathbf{\Omega_{0\perp}} - \frac{\rho \Omega_0^2 R}{enB} \mathbf{b} \times \nabla R \end{aligned} \tag{5.19}$$

Taking the curl of this gives:

$$\nabla \times \mathbf{V}_{\perp} \approx \frac{\mathbf{b}}{B} \nabla_{\perp}^{2} \phi + \frac{\mathbf{b}}{enB} \nabla_{\perp}^{2} P$$

The contributions of inertial terms are approximately zero in this equation. Combined with the definition of vorticity, electrostatic potential and pressure can therefore be related to vorticity by:

$$U = \frac{1}{B} \nabla_{\perp}^{2} \phi + \frac{1}{enB} \nabla_{\perp}^{2} P \tag{5.20}$$

For perturbed magnetic field, $\mathbf{B}$ can be written as $\mathbf{B} = \nabla \times \mathbf{A}$. In the flute reduction, we only consider its parallel component, so the magnetic field can be expressed as:

$$\begin{aligned} \mathbf{B} &= \mathbf{B_0} + \mathbf{B_1} \\ \mathbf{B_1} = \nabla \times \left(\mathbf{b_0} A_{||} \right) &= A_{||} \nabla \times \mathbf{b_0} + \nabla A_{||} \times \mathbf{b_0} \qquad (5.21) \\ &\simeq \nabla A_{||} \times \mathbf{b_0} \approx \nabla \psi \times \mathbf{B_0} \qquad (5.22) \end{aligned}$$

In the Eq.5.22, we used the same definition as it in Hazeltine[89]:

$$\psi = A_{||} / B_0 \tag{5.23}$$

where ψ is also poloidal flux surface function. Based on Ampere's law, then we obtain the expression of plasma current[89]:

$$\mathbf{J} = \mathbf{J_0} + \frac{1}{\mu_0} \nabla \times \mathbf{B}_1 = \mathbf{J}_0 + \frac{1}{\mu_0} \nabla \times \nabla \psi \times \mathbf{B}_0 \tag{5.24}$$

$$\begin{aligned} \nabla \times \nabla \psi \times \mathbf{B}_0 = \nabla \psi \left(\nabla \cdot \mathbf{B}_0 \right) - \mathbf{B}_0 \nabla^2 \psi \\ + \left(\mathbf{B}_0 \cdot \nabla \right) \nabla \psi - \left(\nabla \psi \cdot \nabla \right) \mathbf{B}_0 \end{aligned}$$

The first term of the RHS is zero, and last two terms are small and to be neglected. Therefore, we only keep the second term of RHS. Then the parallel current is:

$$J_{||} = J_{||0} - \frac{1}{\mu_0} B_0 \nabla_\perp^2 \psi \tag{5.25}$$

Combined with Ohm's law, then we can get the evolution equation for ψ from Eq.5.6:

$$E_{||} = \mathbf{b}_0 \cdot \left(-\nabla\phi - \frac{\partial A_{||}}{\partial t} \right) = 2\frac{m_e m_i}{e_e e_i \rho} \mathbf{J} \times \mathbf{\Omega_0} \cdot \mathbf{b} \tag{5.26}$$

and since $A_{||} = \psi B_0$,

$$\frac{\partial \psi}{\partial t} = -\frac{1}{B}\nabla_{||}\phi - 2\frac{1}{B}\frac{m_e m_i}{e_e e_i \rho}\mathbf{J} \times \mathbf{\Omega_0} \cdot \mathbf{B} \tag{5.27}$$

with:

$$\begin{aligned} &\frac{1}{B}\mathbf{J} \times \mathbf{B} \cdot \mathbf{\Omega_0} \\ =& \frac{1}{B\mu_0}\left[B^2\boldsymbol{\kappa} - B\nabla_\perp B\right] \cdot \mathbf{\Omega_0} \end{aligned} \tag{5.28}$$

where the field-line curvature vector $\boldsymbol{\kappa}$ is[177]:

$$\begin{aligned} &\boldsymbol{\kappa} \equiv \mathbf{b} \cdot \nabla\mathbf{b} = (\nabla \times \mathbf{b}) \times \mathbf{b} \\ =& \left[\frac{1}{B}\nabla \times \mathbf{B} - \mathbf{B} \times \nabla\left(\frac{1}{B}\right)\right] \times \mathbf{b} \end{aligned} \tag{5.29}$$

Using the expresion $\nabla\left(\frac{1}{B}\right) = -\nabla(B)/B^2$[89], $\boldsymbol{\kappa}$ is rewritten as:

$$\begin{aligned}
\boldsymbol{\kappa} &= \left[\frac{1}{B}\nabla \times \mathbf{B} - \mathbf{B} \times \nabla\left(\frac{1}{B}\right)\right] \times \mathbf{b} \\
&= \left[\frac{1}{B}\nabla \times \mathbf{B} + \frac{1}{B^2}\left(\mathbf{B} \times \nabla B\right)\right] \times \mathbf{b} \\
&= \frac{1}{B}\mu_0 \mathbf{J} \times \mathbf{b} + \frac{1}{B^2}\left(\mathbf{b} \times \nabla B \times \mathbf{b}\right) \\
&= \frac{\mu_0}{B}\mathbf{J} \times \frac{\mathbf{b}}{B} + \frac{1}{B}\left(\frac{\mathbf{B}}{B} \times \nabla B \times \mathbf{b}\right) \\
&= \frac{\mu_0}{B^2}\mathbf{J} \times \mathbf{B} + \frac{1}{B}\left(\mathbf{b} \times \nabla B\right) \times \mathbf{b} \\
&= \frac{\mu_0}{B^2}\mathbf{J} \times \mathbf{B} + \frac{1}{B}\left[\nabla B\left(\mathbf{b} \cdot \mathbf{b}\right) - \mathbf{b}\left(\mathbf{b} \cdot \nabla B\right)\right] \\
&= \frac{\mu_0}{B^2}\mathbf{J} \times \mathbf{B} + \frac{1}{B}\nabla_\perp B
\end{aligned} \tag{5.30}$$

From this equation we get

$$\mathbf{J} \times \mathbf{B} = \frac{1}{\mu_0}\left[B^2\boldsymbol{\kappa} - B\nabla_\perp B\right] \tag{5.31}$$

where the expression of field line curvature $\boldsymbol{\kappa}$ in drift order[89]:

$$\begin{aligned}
\boldsymbol{\kappa} &= \boldsymbol{\kappa_0} + \boldsymbol{\kappa_1} \\
&\approx \mathbf{b_0} \cdot \nabla \mathbf{b_0} + \frac{1}{B_0^2}\nabla P_1
\end{aligned} \tag{5.32}$$

Taking the parallel component of momentum equation(5.5), we obtain the parallel velocity equation

$$\rho\frac{dV_{||}}{dt} = \mathbf{b} \cdot \nabla P + \rho R \Omega_0^2 \mathbf{b} \cdot \nabla R - 2\rho\boldsymbol{\Omega_0} \cdot \left(\frac{\nabla_\perp \phi}{B} + \frac{\nabla_\perp P}{enB}\right) \tag{5.33}$$

Subtracting Eq.5.28 into Eq.5.27, we get:

$$\frac{\partial \psi}{\partial t} = -\frac{1}{B}\nabla_{||}\phi - 2\frac{1}{B}\frac{m_e m_i}{e_e e_i \rho}\left[B\boldsymbol{\kappa} - \nabla_\perp B\right] \cdot \boldsymbol{\Omega_0} \tag{5.34}$$

And energy conservation equation does not change, we can linearize those parallel velocity, vorticity, energy conservation and ψ evolution equations with:

$$\nabla = \frac{1}{\epsilon}\nabla_f + \nabla_s,\ \nabla_f = \frac{\partial}{\partial x_f},\ x_f = \frac{x}{\epsilon}$$

$$\mathbf{B} = \mathbf{B_0} + \mathbf{B_1} = \mathbf{B_0} + \nabla\psi \times \mathbf{B_0}$$

$$P = P_0 + P_1,\ V_{||} = V_{||1},\ U = U_0 + U_1$$

$$J_{||} = J_{||0} + J_{||1} = J_{||0} - \frac{1}{\mu_0} B_0 \nabla_{\perp}^2 \psi$$

Applying those into Eq.5.12, Eq.5.18, Eq.5.27 and Eq.5.33 we obtain the linearized reduced MHD equations:

$$\rho_0 \frac{\partial U_1}{\partial t} = B_0^2 \left[\mathbf{b}_0 \cdot \nabla \left(\frac{J_{||1}}{B_0} \right) - \mathbf{b}_0 \times \nabla \psi_1 \cdot \nabla \left(\frac{J_{||0}}{B_0} \right) \right]$$

$$2\mathbf{b} \times \boldsymbol{\kappa}_{\mathbf{0}} \cdot \nabla P_1 - \frac{1}{B_0} \rho_0 \mathbf{V_1} \cdot \nabla (B\Omega_{0||}) + \frac{1}{B_0} \rho_0 \mathbf{\Omega_0} \nabla (BV_{||1})$$

$$-\frac{\rho_0}{B_0} \mathbf{b}_0 \times \nabla \phi_1 \cdot \nabla U_1 - \frac{\rho_0}{enB_0} \mathbf{b}_0 \times \nabla P_0 \cdot \nabla U_1 + \frac{\rho_0^2 \Omega_0^2 R}{enB_0} \mathbf{b}_0 \times \nabla R \cdot \nabla U_1 \quad (5.35)$$

$$\frac{\partial \psi_1}{\partial t} = -\frac{1}{B_0} \mathbf{b}_0 \cdot \nabla \phi_1 + \frac{1}{2} \frac{m_e m_i}{e^2 B_0^2 \rho_0} \mathbf{\Omega_0} \cdot \nabla P_1 \quad (5.36)$$

$$\frac{\partial P_1}{\partial t} + \frac{1}{B_0} \mathbf{b}_0 \times \nabla \phi_1 \cdot \nabla P_0 - \frac{\rho_0 R \Omega_0^2}{enB_0} \mathbf{b}_0 \times \nabla R \cdot \nabla P_1 + \frac{2\rho_0 V_{||}}{enB_0} \mathbf{\Omega_{0\perp}} \cdot \nabla P_0$$

$$= \frac{B_0^2}{\mu_0} \frac{v_s^2}{v_A^2 + v_s^2} \left[-\frac{2}{B_0} \mathbf{b}_0 \times \boldsymbol{\kappa}_0 \cdot \nabla \phi - \nabla_{||} V_{||} + \frac{V_{||}}{B_0} \mathbf{b}_0 \cdot \nabla B_0 \right] \quad (5.37)$$

$$\rho_0 \frac{\partial V_{||}}{\partial t} + \frac{\rho_0}{enB_0} \mathbf{b}_0 \times \nabla P_0 \cdot \nabla V_{||1} - \frac{\rho_0^2 R \Omega_0^2 R}{enB_0} \mathbf{b}_0 \times \nabla R \cdot \nabla V_{||1} =$$

$$-\nabla_{||} P_1 + \mathbf{b}_0 \times \nabla \psi_1 \cdot \nabla P_0 + \rho_0 R \Omega_0^2 \mathbf{b}_0 \times \nabla \psi_1 \cdot \nabla R$$

$$-2\rho_0 \mathbf{\Omega_0} \cdot \left(\frac{\nabla_\perp \phi_1}{B} + \frac{\nabla_\perp P_1}{enB} \right) \quad (5.38)$$

$$U_1 = \frac{1}{B_0} \nabla_\perp^2 \phi_1 + \frac{1}{enB_0} \nabla_\perp^2 P_1 \quad (5.39)$$

$$J_{||1} = -\frac{1}{\mu_0} B_0 \nabla_\perp^2 \psi_1 \quad (5.40)$$

where $v_A^2 = B_0^2/\rho\mu_0$ and $v_s^2 = \gamma P_0/\rho$. In these equations, we obtained several new terms due to the rotation effects in our derivation compared to original 4-field Elm-pb equations[19]. Following the same normalization units as BOUT++ that reviewed in chapter 3, we obtain the normalized equations:

$$\begin{aligned}&\frac{\partial \hat{U}}{\partial \hat{t}} + \mathbf{b}_0 \times \hat{\nabla}\hat{P}_0 \cdot \hat{\nabla}\hat{U} - \Lambda\hat{\Omega}_0^2\hat{R}\mathbf{b}_0 \times \hat{\nabla}\hat{R} \cdot \hat{\nabla}\hat{U} + \hat{V}_{||}\partial_{||}\hat{U} \\ &= -\hat{B}_0^2\mathbf{b} \cdot \hat{\nabla}\hat{J}_{||} + 2\mathbf{b} \times \hat{\boldsymbol{\kappa}_\mathbf{0}} \cdot \hat{\nabla}\hat{P} - \hat{V}_{||}\mathbf{b} \cdot \hat{\nabla}(\hat{B}_0\widehat{\Omega_{0||}}) + \hat{\boldsymbol{\Omega}}_\mathbf{0} \cdot \hat{\nabla}(\hat{B}_0\hat{V}_{||})\end{aligned} \tag{5.41}$$

$$\frac{\partial \hat{\psi}}{\partial \hat{t}} = -\mathbf{b}_0 \cdot \hat{\nabla}\hat{\phi} + \frac{1}{2}\frac{m_e}{m_i}\hat{\boldsymbol{\Omega}}_\mathbf{0} \cdot \hat{\nabla}\hat{P} \tag{5.42}$$

$$\begin{aligned}&\frac{\partial \hat{P}}{\partial \hat{t}} + \mathbf{b}_0 \times \hat{\nabla}\hat{\phi} \cdot \hat{\nabla}\hat{P}_0 - \Lambda\hat{R}\widehat{\Omega_0^2}\mathbf{b}_0 \times \hat{\nabla}\hat{R} \cdot \hat{\nabla}\hat{P} + 2\Lambda\hat{V}_{||}\widehat{\boldsymbol{\Omega}_{\mathbf{0}\perp}} \cdot \hat{\nabla}\hat{P}_0 \\ &= -\hat{V}_{||}\partial_{||}\hat{P}_0 + 2\hat{B}_0^2\frac{v_s^2}{v_A^2 + v_s^2}\left[-2\mathbf{b}_0 \times \hat{\kappa}_0 \cdot \hat{\nabla}\hat{\phi} - \hat{\nabla}_{||}\hat{V}_{||} + \frac{\hat{V}_{||}}{\hat{B}_0}\mathbf{b}_0 \cdot \hat{\nabla}\hat{B}_0\right]\end{aligned} \tag{5.43}$$

$$\begin{aligned}&\frac{\partial \hat{V}_{||}}{\partial \hat{t}} + \mathbf{b}_0 \times \hat{\nabla}\hat{P}_0 \cdot \hat{\nabla}\hat{V}_{||} - \Lambda\hat{R}\widehat{\Omega_0^2}\mathbf{b}_0 \times \hat{\nabla}\hat{R} \cdot \hat{\nabla}\hat{V}_{||} \\ &= -\hat{\nabla}_{||}\hat{P} + \mathbf{b}_0 \times \hat{\nabla}\hat{\psi} \cdot \hat{\nabla}\hat{P}_0 + \hat{R}\widehat{\Omega_0^2}\mathbf{b}_0 \times \hat{\nabla}\hat{\psi} \cdot \hat{\nabla}\hat{R}\end{aligned} \tag{5.44}$$

$$\hat{U} = \widehat{\nabla_\perp^2}\left[\hat{\phi} + \left(\frac{m_i}{2e\overline{TB}}\right)\hat{P}/\hat{B}_0\right] \tag{5.45}$$

$$\hat{J}_{||} = \widehat{\nabla_\perp^2}\hat{\psi} \tag{5.46}$$

where R and Ω_0 are normalized with:

$$\hat{R} = \frac{R}{\overline{L}},\ \hat{\Omega}_0 = \overline{T}\Omega_0,\ \hat{V_{||}} = \frac{V_{||}}{\overline{V_A}}. \tag{5.47}$$

Λ is a dimensionless constant equals to $\frac{m_i}{e\overline{BT}}$. Those equations are the models we will use in the further linear simulations. For non-linear cases, the normalized equations become:

$$\begin{aligned}
\frac{\partial\hat{U}}{\partial\hat{t}} + \mathbf{b}_0 \times \hat{\nabla}\hat{\phi}\cdot\hat{\nabla}\hat{U} + V_{||}\partial_{||}\hat{U} \\
+\mathbf{b}_0 \times \hat{\nabla}(\hat{P}_0 + \hat{P})\cdot\hat{\nabla}\hat{U} - \Lambda\hat{\Omega}_0^2\hat{R}\mathbf{b}_0 \times \hat{\nabla}\hat{R}\cdot\hat{\nabla}\hat{U} \\
= -\hat{B}_0^2\mathbf{b}\cdot\hat{\nabla}\hat{J}_{||} + 2\mathbf{b}\times\hat{\boldsymbol{\kappa}}_{\mathbf{0}}\cdot\hat{\nabla}\hat{P} - \hat{V}_{||}\mathbf{b}\cdot\hat{\nabla}(\hat{B}_0\widehat{\Omega_{0||}}) + \hat{\boldsymbol{\Omega}}_{\mathbf{0}}\cdot\hat{\nabla}(\hat{B}_0\hat{V}_{||})
\end{aligned} \tag{5.48}$$

$$\frac{\partial\hat{\psi}}{\partial\hat{t}} - = -\mathbf{b}_0\cdot\hat{\nabla}\hat{\phi} + \frac{1}{2}\frac{m_e}{m_i}\hat{\boldsymbol{\Omega}}_{\mathbf{0}}\cdot\hat{\nabla}\hat{P} \tag{5.49}$$

$$\begin{aligned}
\frac{\partial\hat{P}}{\partial\hat{t}} + \mathbf{b}_0 \times \hat{\nabla}\hat{\phi}\cdot\hat{\nabla}(\hat{P}_0 + \hat{P}) + V_{||}\partial_{||}(\hat{P}_0 + \hat{P}) \\
-\Lambda\hat{R}\widehat{\Omega_0^2}\mathbf{b}_0 \times \hat{\nabla}\hat{R}\cdot\hat{\nabla}\hat{P} + 2\Lambda\hat{V}_{||}\widehat{\boldsymbol{\Omega}_{\mathbf{0}\perp}}\cdot\hat{\nabla}(\hat{P}_0 + \hat{P}) \\
= 2\hat{B}_0^2\frac{v_s^2}{v_A^2 + v_s^2}\left[-2\mathbf{b}_0 \times \hat{\kappa}_0\cdot\hat{\nabla}\hat{\phi} - \hat{\nabla}_{||}\hat{V}_{||} + \frac{\hat{V}_{||}}{\hat{B}_0}\mathbf{b}_0\cdot\hat{\nabla}\hat{B}_0\right]
\end{aligned} \tag{5.50}$$

$$\begin{aligned}
\frac{\partial\hat{V}_{||}}{\partial\hat{t}} + \mathbf{b}_0 \times \hat{\nabla}\hat{P}_0\cdot\hat{\nabla}\hat{V}_{||} - \Lambda\hat{R}\widehat{\Omega_0^2}\mathbf{b}_0 \times \hat{\nabla}\hat{R}\cdot\hat{\nabla}\hat{V}_{||} + 2\Lambda\hat{V}_{||}\widehat{\boldsymbol{\Omega}_{\mathbf{0}\perp}}\cdot\hat{\nabla}\hat{V}_{||} \\
= -\hat{\nabla}_{||}\hat{P} + \mathbf{b}_0 \times \hat{\nabla}\hat{\psi}\cdot\hat{\nabla}\hat{P}_0 + \hat{R}\widehat{\Omega_0^2}\mathbf{b}_0 \times \hat{\nabla}\hat{\psi}\cdot\hat{\nabla}\hat{R} \\
-\hat{V}_{||}\partial_{||}\hat{V}_{||} - \mathbf{b}_0 \times \hat{\nabla}\hat{\phi}\cdot\hat{\nabla}\hat{V}_{||}
\end{aligned} \tag{5.51}$$

$$\hat{U} = \widehat{\nabla_\perp^2}\left[\hat{\phi} + \left(\frac{m_i}{2e\overline{TB}}\right)\hat{P}/\hat{B}_0\right] \tag{5.52}$$

$$\hat{J}_{||} = \widehat{\nabla_\perp^2}\hat{\psi} \tag{5.53}$$

using the new derived equations to update BOUT++ elm-pd code, we then can carry out linear and non-linear simulations. Compared to linear model, the main nonlinear terms from non-inertial terms comes from Coriolis advections.

5.3 Simulations

Using the normalized equations we derived in the previous section, we modified the BOUT++ ELM-pb model to simulate the toroidal rotation effect on ELMs. All involving variables have the same boundary conditions: Neumann for inner boundary and Dirichlet for outer boundary. We use the same shifted circular equilibrium as section 3.4 and section 4.5. For normal 3-field ELM-pb linear simulations, $n_\Psi = 68$, $n_y = 64$ is enough to obtain reasonable results. However, it seems that this resolution is insufficient when concluding non-inertial effects in simulations. We run some linear cases to test the convergence of resolutions. The time evolutions of growth rates under different resolutions are shown in Fig.5.2(a). The growth rates suffer a numerical resonance at first then find the dominant instabilities of ELM, growth rates come to finite values. From Fig.5.2 we can find that $n_\Psi 68 \times n_y 64$ resolution is insufficient to get finite growth rate(Fig.5.2(a)), also numerical instabilities of perturbed pressure on HFS are also distinct(Fig.5.2(b)). However, $n_\Psi 260 \times n_y 64$ resolution seems sufficient in simulation, both finite growth rate and radial perturbed structure on HFS converge to the results of $n_\Psi 516 \times n_y 128$ one. Therefore, we choose $n_\Psi 260 \times n_y 64$ grid resolution in linear simulation.

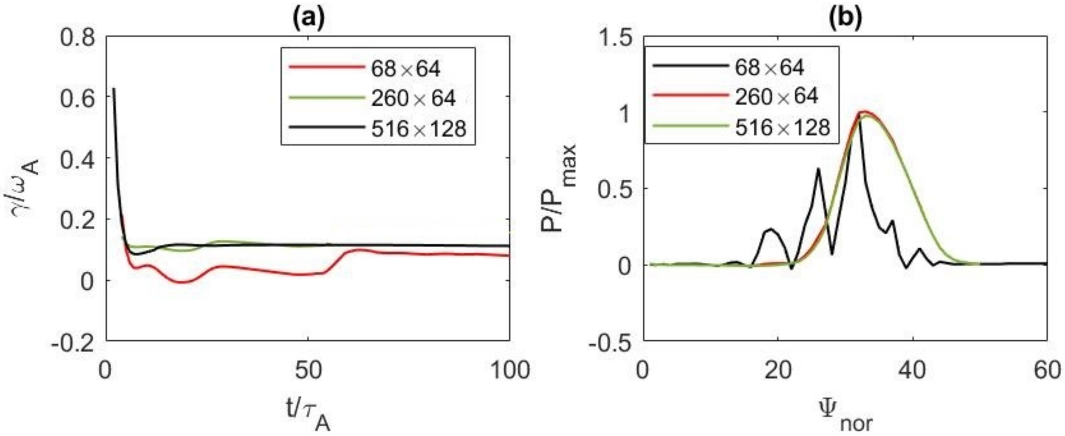

FIGURE 5.2: (a)Linear Growth rates vs. time (b)radial structure of perturbed pressure at $t = 50\tau_A$ on HFS. Where toroidal number n=5, rotation velocity on axis $R_0\Omega_0 = 0.4Mach$, P_{max} is the peak amplitude value of perturbed pressure.

5.3.1 Linear results

Using the Eq.5.41 to Eq.5.46, we perform linear simulations of ELM crash. By changing the toroidal mode numbers in BOUT.inp files, we get the linear growth rates with different rotation rates, shown in Fig.5.3.

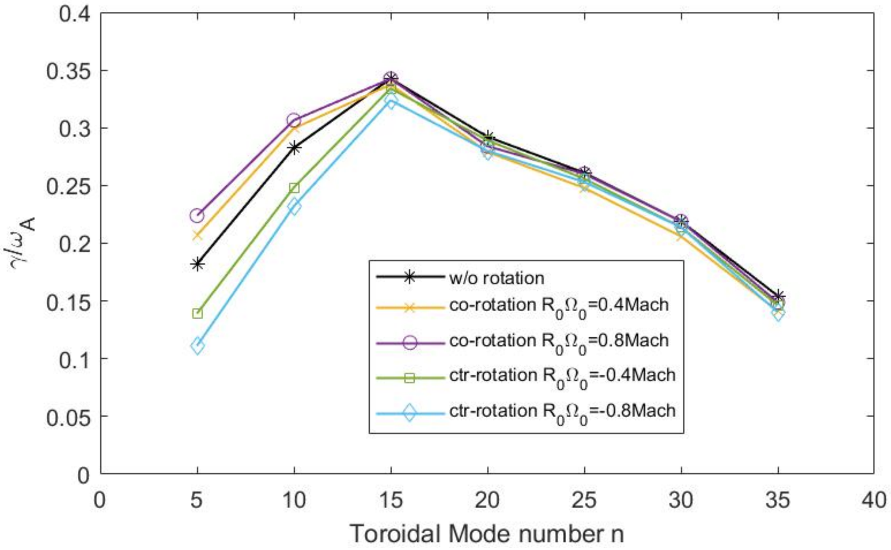

FIGURE 5.3: Growth rate of P-B modes versus toroidal mode number n with different toroidal rotation rates, ctr-rotation indicates counter-current rotation.

From Fig.5.3, it is found that the major impacts of rotation locate on low-n mode peeling-ballooning instabilities. Rotation's effects on high n modes are little. Rotation on counter-current direction can decrease ELM growth rates, and larger growth rate better mitigation effects. On the contrary, the co-current direction's rotation rises the low n mode growth rates, higher rotation rate cause larger instabilities. (Noting that current and magnetic field have negative values on cbm18, but we still define co-current direction rotation as positive to avoiding confusing in the thesis, but change signs on simulations.)

Previous simulation work in inertial system[19] indicates that only shear flow play a role in ELM mitigation. Our results show that rigid toroidal rotation also has mitigation effects on the linear growth of Peeling-Ballooning mode. The impact of rotation locates on low n, little effects on high n modes are obtained.

To understand the reasons, we also checked the terms induced by rotation in Eq.5.41 to Eq.5.46. It was found that the main reason of growth rate suppression or increase of low-n mode is caused by the terms $-\hat{V}_{||}\mathbf{b}\cdot\hat{\nabla}(\hat{B}_0\hat{\Omega}_{0||})+\hat{\mathbf{\Omega}}_{\mathbf{0}}\cdot\hat{\nabla}(\hat{B}_0\hat{V}_{||})$ in the vorticity equation. Those terms have impacts on current-gradient driven instability. As shown in Fig.5.4, parallel flow shear can be obtained on HFS, the two terms play stabilizing or destabilizing roles for counter-current or co-current rotations. Because the current-driven modes (low n instability) can also localized on the HFS, it can explain why rotation has a greater effect on the growth rate of low-n modes.

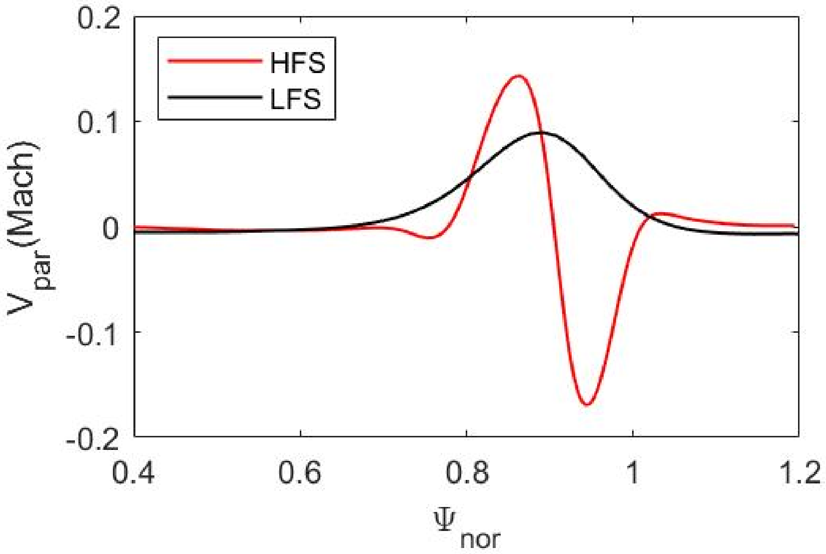

FIGURE 5.4: Radial structures of plasma velocity of HFS (red line) and LFS (black line). Data is collected at $70\tau_A$, toroidal number $n = 5$, rotation velocity at axis $R_0\Omega_0$ is 0.8 Mach.

In addition, we looked into the ploidal structure of perturbed pressure. A little phase shift along the poloidal direction is observed with rotational effect (Fig.5.5). The pressure structure becomes not symmetric about midplane poloidally compared to the non-rotation case. It can be also seen that the perturbed pressure is reduced in LFS, resulting lower growth rate. Noticing that as even the no rotation case perturbed pressure is not symmetric poloidally. This is caused by $\mathbf{E_r} \times \mathbf{B_\Phi}$ drift from a radial electric field. The poloidal rotation would appear as an asymmetry about the midplane. Then perturbed pressure are not up-down symmetric.

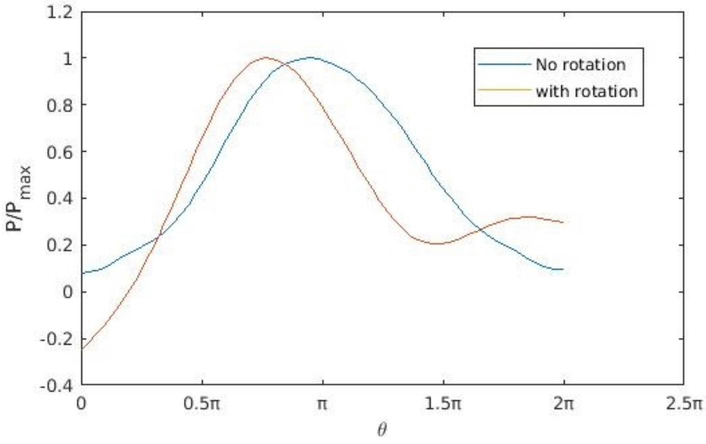

FIGURE 5.5: Comparison of poloidal structure of perturbed pressure between the cases with (red line) and without (blue line) rotation . Data is collected at $70\tau_A$, toroidal number $n = 5$, rotation velocity at axis $R_0\Omega_0$ is 0.8 Mach, the radial location is $0.8\Psi_{nor}$, the $\pi = 0$ index locates in HFS of midplane. P_{max} is the peak amplitude value of perturbed pressure.

In summary, counter-current and co-current direction plasma toroidal rotation can stabilize or destabilize low n P-B mode respectively, in our linear simulation. In addition, higher rotation rates have greater stabilizing and destabilizing effects. Some experiments on grassy-ELM and QH-mode also suggest both the rotation rates and directions matters.

5.3.2 Non-linear Simulations

In our nonlinear simulations, we retain ion diamagnetic effects, resistivity and viscosity. We take same equilibrium as linear cases, but use $n_\Psi 516 \times n_y 128$ resolution, since non-linear simulations require higher resolutions[178]. Compared to linear simulations, high order advection terms were included in equations, specifically, Coriolis advection in vorticity (Eq.5.48), pressure (Eq.5.50) and parallel momentum equation (Eq.5.48). We then look into the time evolution of perturbed pressure at first, shown in Fig.5.6. Unlike ELMs dominated by single toroidal mode n in linear simulations, instabilities often have multi-toroidal modes in non-linear cases. We then set the limits of maximum toroidal mode number $n = 30$ in non-linear simulations.

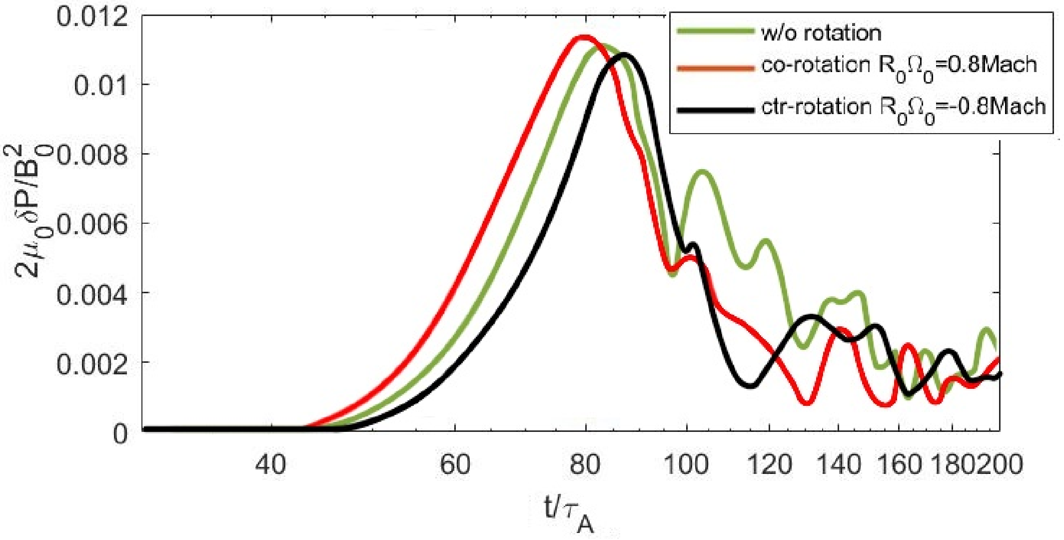

FIGURE 5.6: The perturbed pressure on peak gradient location, the green, red and black lines are the cases without, with co-current and conter-current direction rotations. Rotation velocity at axis is $0.8Mach$.

It is recognized that the ELM crash has three evolution stages from the view of pressure fluctuation. The first one is the phase that all kinds of modes start to evolve. In the next crash phase, the dominant mode rapidly increases until the energy loss amplitude reaches a peak, the ELM begins to crash at this stage. The third one is the turbulence/saturated phase in which turbulent transport is the dominant process[19].

Comparing green, red and black lines in Fig.5.6, we find that in the linear case, plasma with co-current rotation has higher growth than no rotation one. The perturbed pressure reaches a greater amplitude with co-current rotation. On the contrary, the perturbed pressure with counter-current rotation has a smaller amplitude and growth rate in linear growth stage. This result agrees with linear simulation results. In the turbulence phase, both co-current and counter-current rotations mitigate ELMs.

In turbulence phase, a primary quantity of interest to evaluate ELM is the ELM size, defined as

$$\Delta ELM(t) = \frac{\int_{\psi_{out}}^{\psi_{in}} d\psi \oint d\theta P(t)/B_p}{\int_{\psi_{out}}^{\psi_{in}} d\psi \oint d\theta P_0/B_p} \tag{5.54}$$

where P is perturbed pressure, ψ_{in} is the inner boundary of our simulation domain and ψ_{out} is the location of the peak pressure gradient. To further study how rotation saturate ELM in turbulence phase, we plots the data of pressure profiles (Fig.5.7(a)) at $t = 122\tau_A$ and the time averages of ELM sizes($\Delta ELM(t)$) in turbulence phase ($100\tau_A - 200\tau_A$) (Fig.5.7(b)) with different rotation rates.

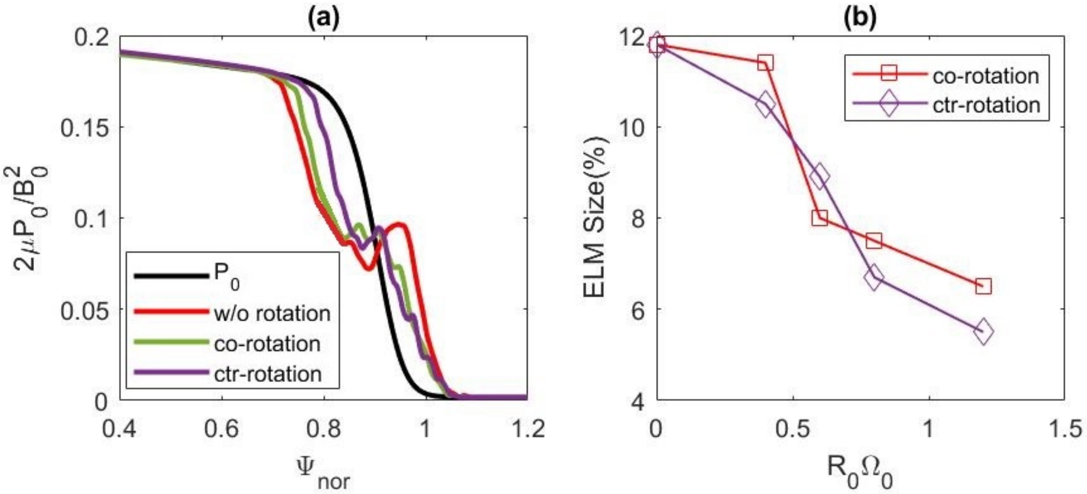

FIGURE 5.7: (a)Pressure profiles in turbulence phase, the black, red, green, purple lines denote the equilibrium pressure profiles, pressure profiles without rotation, with co-current rotation and counter-current rotation. Rotation velocities on axis are $R_0\Omega_0 = 0.4Mach$(co) and $R_0\Omega_0 = -0.4Mach$(counter). (b) Time averaged ELM size vs. different co-current (red square line) and counter-current (diamond purple line) rotation rate.

Fig.5.7(a) can be interpreted as that the growth of the perturbation is suppressed by the rotation in the turbulence phase. It is also found that the pressure without shear penetrates deeper. This means that the radial extent of the pressure perturbation is reduced by both co-current and counter-current rotation. Fig.5.7(b) shows that ELM sizes decrease with toroidal rotation rates, for both directions of toroidal rotation.

Further, we look into the influences of rotations on ELMs sizes through spatial Fourier transform on perturbed pressure in toroidal direction(Fig.5.13). The n (toroidal mode) structures of averaged ELM sizes ($t = 100\tau_A - 200\tau_A$) shows rotations on both directions can mitigate high n components ELM size. The difference is that co-current rotation destabilizes low n mode ELM size and leads to the dominant mode cascade to low n mode (from $n = 15$ to $n = 10$). While counter-current rotation suppresses ELM sizes of both low and high n modes. The reason of these differences may be the terms $-\hat{V}_{||}\mathbf{b} \cdot \hat{\nabla}(\hat{B}_0\hat{\Omega_{0||}}) + \hat{\mathbf{\Omega}}_\mathbf{0} \cdot \hat{\nabla}(\hat{B}_0\hat{V}_{||})$

discussed in linear simulations, which make the destabilization and stabilization of low n modes with co-current and counter-current rotations. The non-linear effects of Coriolis and Centrifugal advection suppress the ELM sizes of both low n and high n mode. Then only counter-direction rotation involves in the latter mechanism study.

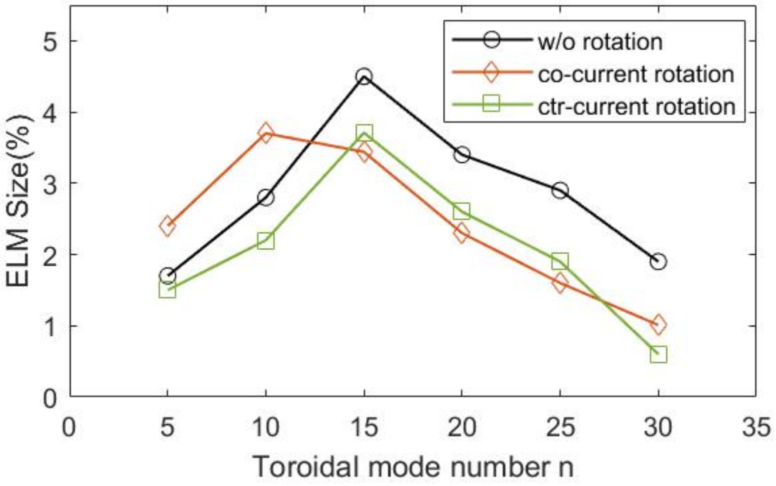

FIGURE 5.8: Time averaged ELMs sizes of each n components without rotation (black circle lines), with co-current (red diamond lines) and counter-current rotation (green square lines). Rotation velocity at axis are $R_0\Omega_0 = 0.8Mach$, $R_0\Omega_0 = -0.8Mach$ separately.

To study the mechanisms of rotation's stabilization effect with non-inertial terms. We look into 2D-poloidal and radial structures of perturbed pressure, shown in Fig.5.9. It is found that the structure pressure perturbations differs poloidally and radially with rotation.

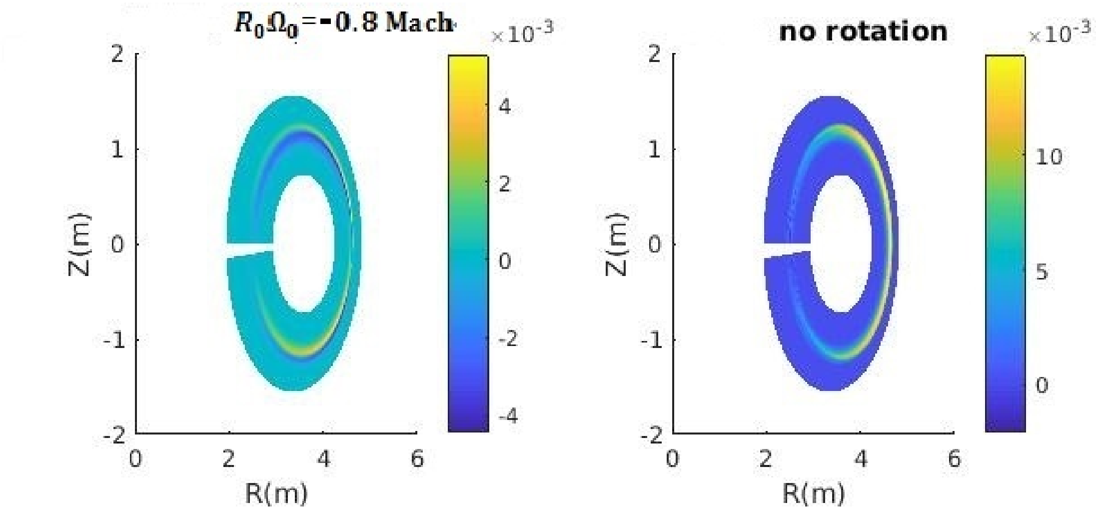

FIGURE 5.9: The 2D structure (poloidal plane) of perturbed pressure with counter-current (left) and without(right) rotation in non-linear simulations. Data is collected at their crash stage respectively, rotation velocity at axis $R_0\Omega_0$ is 0.8 Mach.

Then we look into poloidal and toroidal structure of perturbed pressure separately. Fixing the radial location at $0.8\Psi_{nor}$, the perturbed pressure shifts in poloidal direction at ELM crash stage ($t = 96\tau_A$), shown in Fig.5.10. The index 0 and 2π is the poloidal location of LFS on midplane. Fig.5.10 tells the peak of pressure perturbation shift to $+-0.5\pi$ (top and down) poloidally. Then we operate flux surface average on perturbed pressure to investigate radial structures, the averaged pressure perturbation is defined as[9]:

$$<P>=\frac{\int_0^{2\pi} d\zeta \oint d\theta P/B_p}{\int_0^{2\pi} d\zeta \oint d\theta/B_p} \tag{5.55}$$

where ζ is the toroidal angle. The radial structure of averaged pressure at ELM crash stage ($t = 96\tau_A$) is plotted in Fig.5.11.

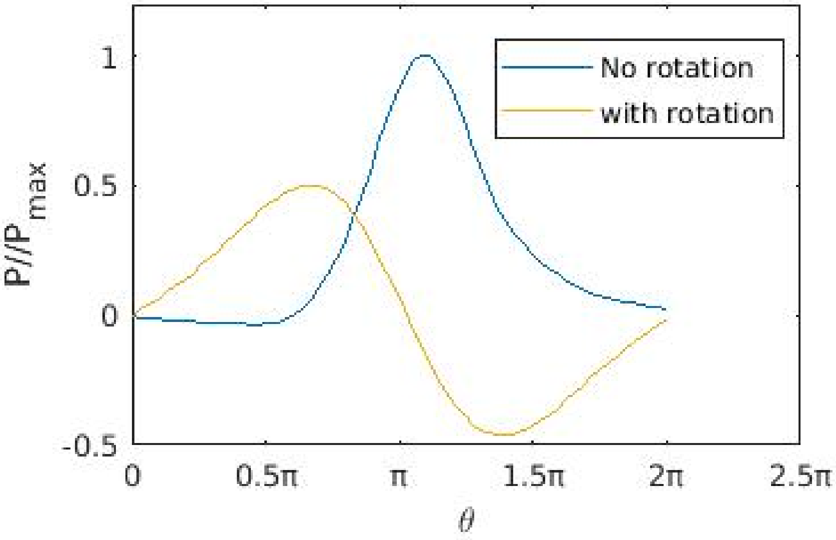

FIGURE 5.10: Comparison of poloidal structure of perturbed pressure between the cases with(red) and without(blue) rotation. Data is collected at their crash stage respectively, counter-current rotation velocity at axis $R_0\Omega_0 = -0.8Mach$, the radial location of two profiles is $0.8\Psi_{nor}$, the $\pi = 0$ index locates in HFS of midplane. P_{max} is the peak amplitude value of perturbed pressure.

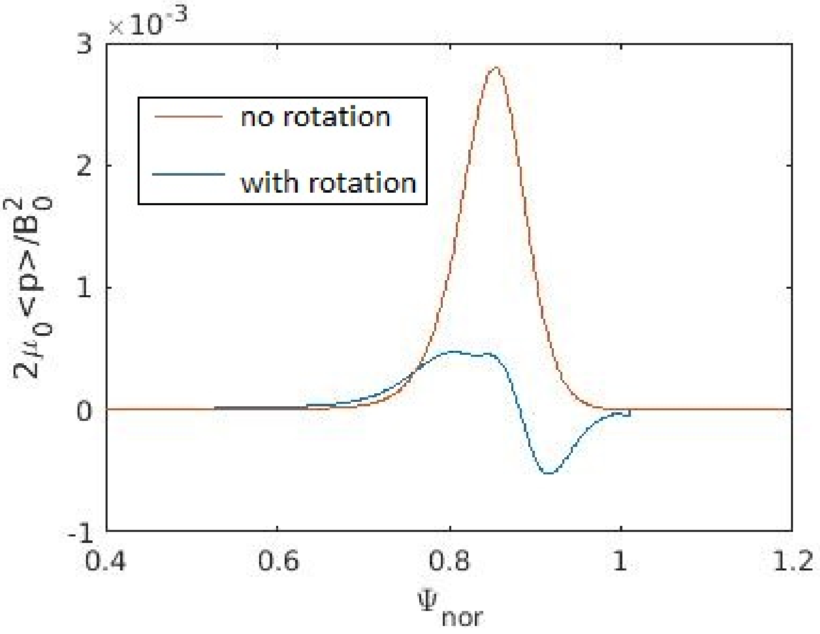

FIGURE 5.11: Radial structures of flux-averaged perturbed pressure with and without rotation. Data is is collected at their crash stage respectively, counter-current rotation velocity at axis $R_0\Omega_0 = -0.8Mach$, the radial location of two profiles is $0.8\Psi_{nor}$.

From the results in Fig.5.9 and Fig.5.10, we find that different from the linear simulation, a strong phase shift of perturbed pressure occurs. The perturbed pressure peaks at the top of the poloidal plane instead of the outboard mid-plane poloidally. That makes the reduction of the pressure gradient in bad curvature region (normally outer mid-plane). The peeling-ballooning instabilities are therefore mitigated owing to the non-inertial effects. This is because ELM crash mainly happens at the LFS of outer mid-plane[31](because of bad curvature). Similarly, Dickinson and Abddoul [179, 180] reported that the poloidal pressure phase shift can stabilize micro-instabilities, by introducing an external poloidally asymmetry electrostatic potential. Besides, the rotation also broadens the perturbed pressure radial structures and reduce pressure amplitudes in the pedestal region (Fig.5.11). Since lower pressure perturbation in peak pressure region, this kind of pressure radial structure change may suppress ELM size.

To further study the role of Centrifugal and Coriolis effects independently. we carry out ELM nonlinear simulations with keeping the terms related to one of these two effects (centrifugal and Coriolis) separately. From the view of the perturbed pressure' 2D structure (shown in Fig.5.12) at the beginning of turbulence phase($t = 120\tau_A$), the Coriolis effects mainly contribute to the pressure poloidal phase shift (Fig.5.12(a)). On the other side, centrifugal terms have an influence on pressure's radial structure (shown in Fig.5.12(b)). Fig.5.12(c) shows both the radial and poloidal structure change under the influence of whole non-inertial effects, compared to the pressure perturbation without rotation (Fig.5.12(d)). We also notice that the perturbed pressure has boarder radial fluctuation in the absence of rotation.

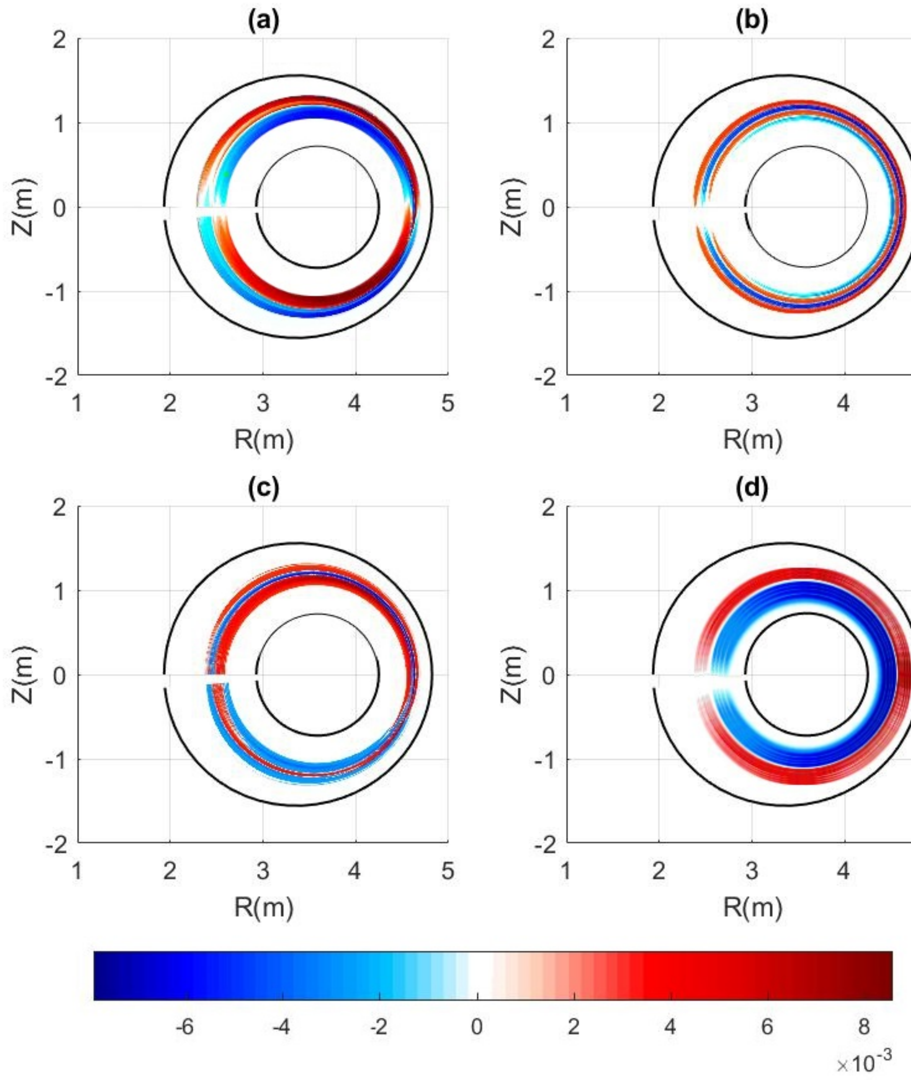

FIGURE 5.12: The 2D structure (poloidal plane) of perturbed pressure under the centrifugal(a) and Coriolis's(b) effects; (c) and (d) are the perturbed pressure with all non-inertial effects and without rotation respectively. Rotation velocity at axis $R_0\Omega_0 = -0.8Mach$, perturbed pressure is normalized by $2\mu_0 P_0/B_0^2$.

Lastly, we compare the time average ELM sizes in the turbulence phase with centrifugal and Coriolis's effects independently on Fig.5.13. It is found that both centrifugal and Coriolis terms can reduce ELM size independently. In addition, comparing the value of the black diamond, red circle and green cubic lines in Fig.5.13, it can be summarized that centrifugal and Coriolis terms have coupling effects on ELM size reductions (The ELM size with both effects is smaller than the ones with single Centrifugal or Coriolis effect).

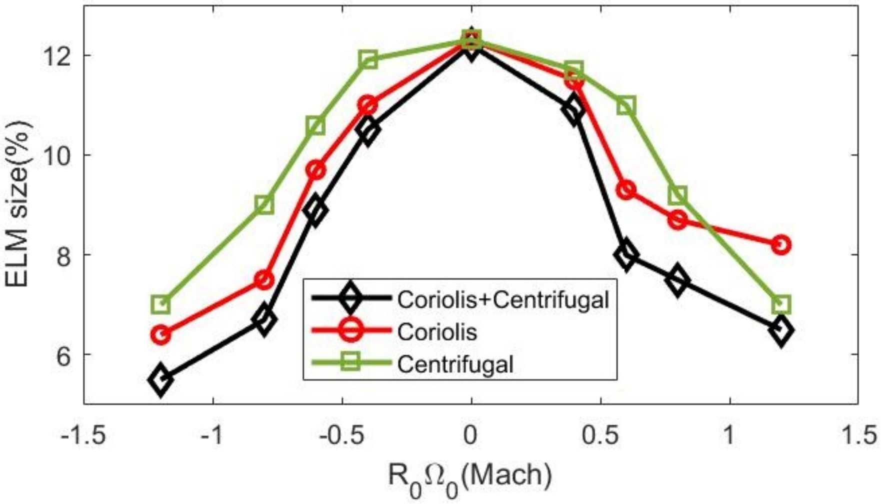

FIGURE 5.13: Time-averaged ELM sizes in turbulence phase, black diamond, red circle and green cubic lines denote both effects, Coriolis and Centrifugal effect respectively, rotation velocity on axis $R_0\Omega_0 = -0.8Mach$.

5.4 Summary and discussion

To summarize, the plasma flow's effects on ELMs are shortly reviewed at the begining of this chapter. Then 4-field reduced-MHD equations are derived from collisionless Vlasov equation in a non-inertial rotating frame, new terms concludes both centrifugal and Coriolis effects. Applying these new fixed 4-field equation into the Elm-pb code, we carried out linear and non-linear simulations. In linear simulations, it obtained that the impact of rotation on low n modes are greater than high n modes. It is also found that co-current direction rotation enhance low n instabilities, while counter-current rotation mitigate ELMs on low n modes. Mechanisms of the results are also explored, we address the terms $-\hat{V}_{||}\mathbf{b}\cdot\hat{\nabla}(\hat{B}_0\hat{\Omega_{0||}})+\hat{\mathbf{\Omega_0}}\cdot\hat{\nabla}(\hat{B}_0\hat{V}_{||})$ related to Coriolis effects play the majority roles.

From the results of non-linear simulation, we find perturbed pressure grows faster with co-current rotation that whom with counter-current rotation and without rotation. In addition, toroidal rotation on both co and counter directions can mitigate ELM size in turbulence phase. In our preliminary study, one of the mechanisms is the poloidal shift of perturbed pressure, resulting in reduced pressure gradient in LFS (bad curvature side). And Centrifugal terms have an influence on radial structure of perturbed pressure, also resulting in the suppression of ELM size. Those conclusions comes to an agreement with some previous ballooning and micro-instabilities studies[179, 180]. Abdou's([180]) work only points out the asymmetric perturbations cause the stabilization of ballooning mode, but can't explain how those asymmetricity come from. Therefore, non-inertial seems to be the a reason of this ELM size reduction. From the result of simulation, we also conclude that there exists coupling effects between centrifugal and Coriolis terms, mean the ELM size with both effects is smaller than the ones with single Centrifugal or Coriolis effect.

In conclusion, studies of flow's influence on ELMs are reviewed, it is well recognized that plasma rotation has significant effects on ELMs. In the previous BOUT++ simulation work, the effects of rotation is carried out in inertial system, centrifugal and Coriolis terms are not concluded in those studies[19, 123]. The results of previous work indicate that only $\mathbf{E} \times \mathbf{B}$ can influence ELM growth rates and size significantly, rigid rotation without shear has little impact on P-B instabilities. However, the experiments in JT-60 suggest that it is the sign or absolute value of velocity rather than its shear[34]that influence ELMs. Our results indicate that the non-inertial effects should be taken into consideration in ELM studies. In the previous studies, the P-B instability studies generally focus on the radial characteristics of pressure profiles, the results of this chapter suggest that poloidal structure or parallel structure of pressure is also important.

However, the work in this chapter still has several limitations. First, the density evolution is not fully included in the equations, which has been proved to have dominant effect in poloidal flow[62]. Second, further studies of coupling effects of centrifugal and Coriolis are still required. Lastly, the results show the low-n instabilities are important, further work are still required with updated model which has good performance in low n(n¡3) instabilities.

Chapter 6

Conclusion and Discussion

The design of a large scale magnetic confinement fusion machine presents large scale technical challenges. One such challenge involves reducing the peak energy loads to the divertor during large ELM operating scenarios. Therefore it is necessary to explore the mechanisms and methods to mitigate ELMS.

In chapter 1 of this thesis, the high performance operating mode (H-mode) in the study of tokamak was reviewed, including the advantages of H-mode and factors that influence it. Previous experiments and analytic studies were also reviewed and discussed. The issues and the conditions that trigger H-mode, including L-H transition were also listed. Finally, the Edge Localized mode (ELM), as one of most important MHD instabilities which trigger ELMs was discussed. Further, experiments and theories of ELM studies are introduced. Pedestal physics and Peeling-ballooning mode theories were highlighted in the review. The benefits and drawbacks of ELMs in tokamak confinement and H mode operation were discussed. Finally, we reviewed the effects of plasma rotation and flow shear on the mitigation of ELMs. As one of most important shear flow in plasma, Zonal Flow (ZF) and Geodesic Acoustic Modes (GAMs) need to be addressed; some experiments findings concerning ZF and GAM were discussed at the end of chapter 1.

The main simulation tools, including framework of BOUT++, elm-pb mode, Hermes cold ion model and CORSICA is introduced briefly in Chapter 2.

In chapter 3, we explored the mechanism of ELMs besides the Peeling-ballooning mode. Since previous experimental and analytically work proved that peeling modes are stable in pedestal regions. Based on previous work, we propose the kink-ballooning mode- a kind of plasma instability driven by current gradient inside of resonant surface and pressure gradient. From the energy principle, we get the kink mode criteria on plasma current and current gradient. Caltrans-Corsica is used to regenerate the equilibria . We the found that kink-ballooning mode can drive ELM in some peeling-ballooning stable regions.

Chapter 4 focused on rotation's effect on ZF and GAMs in non-inertial frame. In this part, previous work on GAMs and ZF flows were reviewed. Theories of drift wave and GAM propagation were highlighted. In this chapter, Drift-ordered 2-fluid equations were derived from collisional Vlasov equation in non-inertial rotating frame firstly, under the cold ion assumption. We then solved these equations using the Hermes cold ion code. The results of simulations revealed that ZF rate and GAM frequency grows with increasing toroidal rotation rate. Comparing to analytic work, it was found that phase differences between parallel momentum and electrostatic potential can also excite ZF and GAM. The Coriolis convection plays a similar role as ion magnetic drift in the propagation of GAMs. The effects of external density source are also studied; it turns that the asymmetric source injection can enhance the growth of GAM and ZF. We suggest that the ZF and GAMs may be able to be triggered under the condition of some arbitrary heating such as ECRH. At last of this chapter, preliminary results of some experiments are briefly addressed, aiming to validate the analytic and simulation results.

In the Chapter 5, studies of flows influence on ELMs are reviewed critically. 4-field reduced-MHD equations were derived from collision-less Vlasov equation in a non-inertial rotating frame. Linear and non-linear simulations were performed with modifying the Elm-pb code. Mechanisms of the results are explored, co-current destabilize, while counter-current stabilize the low n instablities. Then modification terms of current in non-inertial system helps to suppress current drive instabilities. The non-linear simulation results show that toroidal rotation can suppress ELM size . The poloidally phase shift of perturbed pressure on is proposed to be the reason of ELMs suppression.

One interesting outcome in chapter 3 and chapter 5 is both kink-ballooning mode and rotation play major effects on low-n modes. Coincidentally, the Q-H modes happen on low-n modes. Current simulation studies find that $\mathbf{E} \times \mathbf{B}$ shear flow plays an important role in the formation of Q-H mode, which has good agreements with experiments[56, 57]. However, the results of experiments indicate that the directions of flow matters in Q-H mode[181], previous simulation work fails to explain this. In our simulations in chapter 5, co-current and counter-current rotations play different roles in low-n instabilities due to non-inertial effects. Therefore, it is essential to study the Q-H mode in the non-inertial frame in future work.

Overall, this thesis has addressed the effect of current and rotation on tokamak edge instabilities analytically and numerically. 3-D simulations of MHD instabilities in non-inertial frame for the first time. The centrifugal and Coriolis effects have been proven important role in the generation and propagation of GAM and Zonal flow. Non-inertial effects on ELM mitigation are also proposed and verified. One of applications of this work is to the possibility of influencing ELMs using radio frequency (ECRH), either through current drive or by influencing flows. However, there are several limitations for this work. First, the ion temperature is absent in GAM and Zonal flow simulation, which may changes the characters of GAM and ZF. Second, the mechanism of non-inertial terms' ELM mitigation effects required further exploration in the . Finally, the density evolution needs to be taken into consideration in further ELM simulations.

Appendix:

A simple model for ECRH induced poloidal spin up in low collisional Plasmas

Abstract

An approach of producing the poloidal ion rotation by using electron cyclotron resonance heating (ECRH) is presented in tokamak plasmas. The rf cyclotron heating can induce a poloidal density inhomogeneity and then destabilize the anomalous Stringer spin up. A quasilinear diffusion coefficients in the presence of rf wave is given, based on that the poloidal density inhomogeneity can be obtained. The numerical results have shown that the poloidal ion rotation can be destabilized, in addition, the relationship between the rf induced poloidal rotation and the electron cyclotron wave is studied.

1. Introduction

Recent studies of the achievement of improved confinement suggest that the sheared plasma rotation (either toroidal or poloidal) can suppress the turbulences and consequently improve the plasma confinement [1, 2]. A successful example of conducting H-mode operations by rotating plasma is the imposed biased electrode experiments performed in many tokamaks.

At the same time, flow shear caused by the rotation also suppress the turbulence transport, so as to achieve the purpose of controlling edge localized mode (ELM).

In the previous papers, mostly, only the toroidal rotation is considered, while the poloidal one is neglected[3, 4]. For the poloidal rotation is strongly damped without any momentum sources, based on neo-classical transport theory. Thus, it is essential to look for a way to drive the poloidal rotation in looking for new ways to mitigate ELMs.

Exploration of the mechanisms of the plasma rotation is also an attractive subject. Some research works on plasma rotation mechanisms are reported: for example, ion orbit, Reynolds stress, the Stringer spin up[5-7]; etc. Hassam suggested a poloidal plasma rotation mechanism by developing the Stringer spin-up theory. He pointed out that, those approaches that can produce an in–out asymmetric density distribution on a magnetic surface may induce a poloidal plasma rotation. Later, C. G. Liu[9] develop Hassam's mode based on Hsu's[10] theory, in his theory, the magnitude of the poloidal density asymmetry would be significantly enhanced by the RF wave cyclotron heating because of the resonance localization. This kind of asymmetry can induce a poloidal electric field, ion will redistribute and form a poloidally inhomogeneous ion profile acted by this field, which has the same effects as the in-out asymmetric density source in Hassam's mode. Combining the poloidal density asymmetry produced by the resonance localization in the rf wave cyclotron heating with the poloidal plasma spin-up destabilized by the in–out density asymmetry, the poloidal plasma rotation can be actively produced by means of the Electron Cyclotron waves.

However, the fundament of Liu's mode is Hsu's works, who assume that the electric field has already existed in his drift-kinetic equation; this seems not self-consistent. So, this electric field should be calculated correctly via rigid quasi-linear equation to figure out whether the Electron Cyclotron Heating can induce the poloidal rotation.

The rest of the paper is organized as follows. In next section the exact guiding center variables are derived with Hamiltonian transformation, a new spatial variable is introduced into the diffusion function. The expression of the poloidal rotation speed is derived base on Hassam's work[8] in section 3. In section 4, via numerical calculation, the relationship between the poloidal rotation and the rf waves are given. A brief summary is presented in the last section.

2. QuasiLinear Equation

In tokamak configuration, the relativistic Hamiltonian of a charged particle can be expressed as [11]

$$H = \frac{1}{2M}\left[\left(P_R - qA_R\right)^2 + \left(P_Z - qA_Z\right)^2 + \left(P_j - qRA_j\right)^2 \big/ R^2 \right] + q\Phi \tag{1}$$

A_R, A_z, andA_φ are the vector potential components of the magnetic field, and Φ is the electrical potential and assumed to be a function of Ψ. Here, Ψ is the poloidal flux of the magnetic field. A_R,A_z and A_φ are the canonical momenta conjugate to the cylindrical coordinates R, φ and Z, respectively.

Introducing a generating function for changing to the guiding center variables

$$F_1 = -\frac{\Omega_0 R_0^2}{2}\exp\left(\frac{X}{\Omega_0 R_0}\right)\left(\ln\frac{R}{R_0} - \frac{X}{\Omega_0 R_0}\right)^2 tg\,a - ZX \tag{2}$$

Where

$$X = \Omega_0 R_0 \ln\left(\frac{R_C}{R_0}\right) \tag{3}$$

and $\Omega_0$is the gyrofrequency in the toroidal field, ρ is the Larmor radius, α is the gyrophase, and subscripts 0 and c refer to the values at the magnetic axis and the guiding center position, respectively. *X* andα are the new coordinates conjugate to the momenta

$$Z = P_X - r\sin a - \frac{r^2}{4R_C}\sin 2a \tag{4}$$

$$P_\alpha = \frac{1}{2} m_0 \Omega_c \rho^2 \tag{5}$$

The other two canonical variables P_φ and φ do not change in the new coordinates.

The old coordinates are connected with the new ones through four equations:

$$P_R = m_0 \Omega_c \rho e^{(\rho/R)\cos\alpha} \sin\alpha \tag{6}$$

$$P_Z = -X = -m_0 \Omega_0 R_0 \ln\frac{R_C}{R_0} \tag{7}$$

$$R = R_C \exp\left(-\frac{r\cos a}{R_C}\right) \tag{8}$$

$$Z = P_X - r\sin a - \frac{r^2}{4R_C}\sin 2a \tag{9}$$

where P_X is actually the *Z* coordinate of the guiding center. Such fact that a momentum is turned to be a coordinate often occurs during area-conserved canonical transformation.

Hence, we form a new invariant:

$$\Pi_\alpha = \frac{1}{2\pi}\oint P_X dX \tag{10}$$

The action invariant is the toroidal flux enclosed by a particle orbit which actually is an implicit Hamiltonian from which the bounce frequency and precession frequency can be calculated. For trapped particles in a large aspect ratio configuration, that is,$\varepsilon = r/R_0 \ll 1$, we get

$$\Pi_t = \frac{8qR_0 m_0 \overline{\varepsilon\Omega_0 P_\alpha/m_0}}{\pi}[E\ k_1\ -\ 1 - k_1{}^2\ K\ k_1\ ] \tag{11}$$

The bounce frequency and the precession frequency are obtained from (11) as in []:

$$\omega_{bt} = \frac{\pi\ \overline{\varepsilon\Omega_0 P_\alpha/m_0}}{2qR_0K\ k_1} \tag{12}$$

$$\omega_{\xi t} = \frac{2\Omega_0 P_\alpha}{\Omega_p m_0 R_0^2}\ \frac{E\ k_1}{K\ k_1} - \frac{1}{2} + \frac{4\Omega_0 P_\alpha s}{\Omega_p m_0 R_0^2}\left[\frac{E\ k_1}{K\ k_1} - \ 1 - {k_1}^2\ \right] \tag{13}$$

Ω_p is the poloidal gyro-frequency,$k_1^2 = u_{\varphi0}^2/(4\varepsilon\Omega_0 P_\alpha)$, $E\ k_1$ and $K\ k_1$ are complete elliptic function of the first and second kinds. The bounce-averaged gyro-frequency of the trapped particles is

$$\Omega = \Omega_0 * [1 - 2\varepsilon(\frac{E\ k_1}{K\ k_1} - \frac{1}{2})] \tag{14}$$

where Ω is a nonlocal gyro-frequency.
In the extended phase space the Hamiltonian is written as follows []:

$$H\ \bar{p},\bar{q}\ = H\ p,q,t\ - H \tag{15}$$

According to Liouville's theorem, the distribution function, *f*, satisfies Vlasov's equation:

$$\frac{\partial f}{\partial t} + \eta\frac{\partial f}{\partial \eta} + \alpha\frac{\partial f}{\partial \alpha} + \zeta\frac{\partial f}{\partial \zeta} + \Pi\frac{\partial f}{\partial \Pi_t} + P_\alpha\frac{\partial f}{\partial P_\alpha} + P_\zeta\frac{\partial f}{\partial P_\zeta} + H\frac{\partial f}{\partial H} = 0 \tag{16}$$

where *f* can be divided in two parts, the averaged part and oscillatory part:

$$f = f_0 + f_1 \tag{17}$$

The linear solution of (16) is []:

$$f_1 = \frac{\omega H_1\frac{\partial f_0}{\partial H} + nH_1\frac{\partial f_0}{\partial P_\zeta} + mH_1\frac{\partial f_0}{\partial \Pi_t} + lH_1\frac{\partial f_0}{\partial P_\alpha}}{\omega - n\omega_\zeta - m\omega_\eta - l\Omega} \tag{18}$$

and f_0 is a function of H, *Pα*, and *Pζ* only, independent of *η, σ, α* and If H1 is a slow function of *Pσ, Pα,* and H, we get the quasi-linear equation:

$$\frac{\partial f_0}{\partial \tau} + \mathrm{LDL}f_0 = C(f_0) \tag{19}$$

where $D = \sqrt{\pi}H_1^2\frac{1}{\Delta\omega}exp\ -\frac{\hat{\omega}-l\hat{\Omega}-m\hat{\omega}_{bt}\ ^2}{\Delta\omega\ ^2}\ /\upsilon$, $\tau = t\upsilon$, υ is collision frequency.

$$L = \frac{m}{\omega}\frac{\partial}{\partial \Pi_t} + \frac{n}{\omega}\frac{\partial}{\partial P_\zeta} + \frac{l}{\omega}\frac{\partial}{\partial P_\alpha}\ .$$

For LD is very small, hence the equation (19) can be rewritten as:

$$\frac{\partial f_0}{\partial t} + \hat{D}[m^2\frac{1}{(\frac{\partial\Pi}{\partial k_1})^2}\frac{\partial^2 f_0}{\partial {k_1}^2} - m^2\frac{1}{(\frac{\partial\Pi}{\partial k_1})^3}\frac{\partial^2\Pi}{\partial {k_1}^2}\frac{\partial f_0}{\partial k_1} + n^2\frac{\partial}{\partial\hat{\Psi}^{\bullet 2}} + l^2\frac{\partial}{\partial {\hat{P}_a}^2}] = C(\bar{f}) \tag{20}$$

From [] we know the turning point θ_t satisfy the following term.

$$q_t = \left(\frac{2u_{j\,o}^2}{eu_\perp^2}\right)^{1/2} = \left(\frac{u_{j\,o}^2}{e\Omega_c P_a}\right)^{1/2}$$

It is easy to find that θ_t is related to k_1 So, we can get $f(\theta_t)$ after solving equation (20), and then the potential of poloidal electric field can be obtained.

3. Poloidal electric potential and poloidal rotation

Following Hsu's work[10], the potential of poloidal electric field can be calculated. Firstly, the electron density satisfied the term:

$$n_e = \iint f d^3 v = \iint f \frac{2\pi dH d\mu B}{m^2 v_\parallel} \quad . \tag{21}$$

In this paper's coordination, term (21) becomes:

$$\iint f \frac{2\pi dH d\mu B}{m^2 v_\parallel} = \iint f \frac{4\pi v_\parallel dv_\parallel d\mu B}{m^2 v_\parallel} = \iint f \frac{4\pi dv_\parallel d\mu B}{m^2} = \iint f \frac{4\sqrt{2}\pi d\theta_t dP_\alpha B}{m^2} \quad \frac{\overline{\Omega P_\alpha \varepsilon}}{\Omega_0}. \tag{22}$$

The next step, supposing the ion density followed Boltzmann's distribution.

$$n_i = n_0 exp \quad - \frac{e(\phi-\phi_0)}{T_i} \quad \approx n_0(1 - \frac{e(\phi-\phi_0)}{T_i}) \quad , \tag{23}$$

where T_i is ion temperature , n_0 and ϕ_0 are initial ion density and potential.

Also with Electrically neutral conditions, $n_e = n_i$. Using the following terms, the potential of poloidal electric field can be obtained.

Therefore, the density asymmetric density is as follows:

$$\frac{n_1}{n_0} = - \frac{e(\phi-\phi_0)}{T_i} \tag{24}$$

This asymmetry can be regarded as a density source:

$$S = n < - \frac{e(\phi-\phi_0)}{T_i} > \tag{25}$$

Take the source into MHD equations and ohm's law[8]:

$$\mathbf{B} \cdot \quad n\mathbf{B} \cdot \frac{\mathbf{u}}{\mathrm{B}^2} \quad = -nm\mathbf{u}u_\perp - \frac{\partial n}{\partial t} + S \tag{26}$$

$$T\mathbf{B} \cdot \quad n = -\mathbf{B} \quad \cdot \quad nm\mathbf{uu} \quad - \mathbf{B} \quad \cdot \chi - \frac{\partial \; nm\mathbf{B}\cdot\mathbf{u}}{\partial t} + \mathbf{B} \cdot \mathbf{P} \tag{27}$$

$$\mathbf{J}_\perp = \frac{\mathbf{B}}{B} \times \; [T \quad n + \quad \cdot \chi + \frac{\partial}{\partial t} nm\mathbf{u} + \quad \cdot nm\mathbf{uu} - \mathbf{P} \tag{28}$$

$$\mathbf{B} \cdot \quad \frac{\mathbf{J}_\parallel}{\mathbf{B}} \quad = \quad \cdot \mathbf{J}_\perp \tag{29}$$

$$\mathbf{B} \cdot \quad \phi = 0 \tag{30}$$

$$u_\perp = \frac{\mathbf{B}\nabla\times\phi}{\mathrm{B}^2} \tag{31}$$

We can get an evolution equation of the poloidal rotation speed induced by strong rf cyclotron heating as

$$\frac{\partial}{\partial t}K = -\Gamma K + \hat{S}_K \tag{32}$$

In the equation, $K = \langle B_p \cdot u/B_p \rangle$ is proportional to the local poloidal velocity.

$$\Gamma = \frac{\langle S \rangle}{n} + \frac{\langle S\Delta_B \rangle}{n} + \frac{\eta}{nm}\frac{\langle(\mathbf{b}\cdot\nabla\mathbf{B})^2\rangle}{\langle\mathbf{B}^2\rangle}. \tag{33}$$

It is not hard to find that only if $\Gamma < 0$, the poloidal rotation could be driven.

4. Numerical study

From the discussion of the previous texts, the rotation velocity induced by the ECRH can be obtained from equation (20), (22) and (32). In our numerical calculation, the following parameters are used: the major radius R=1.45 m; the minor radius a=0.45 m, the toroidal magnetic field Bt= 2.8 T; at r the initial ion and electron temperature T_i= T_e=4.14 keV; the electron density $n_e = 1.7\times10^{19}\text{m}^{-3}$, the trapped electron density n_t/n_e=10%.

For the equation (20) is similar to the transport equation, we can use BOUT++ to do calculations. Before calculating the electric potential and rotation velocity, we verify the feasibility of this method via calculate the distributions in phase space (Figure 1- Figure 5). The results seem right compared to some verified works, hence, we can use this method to calculate the potential and rotation velocity.

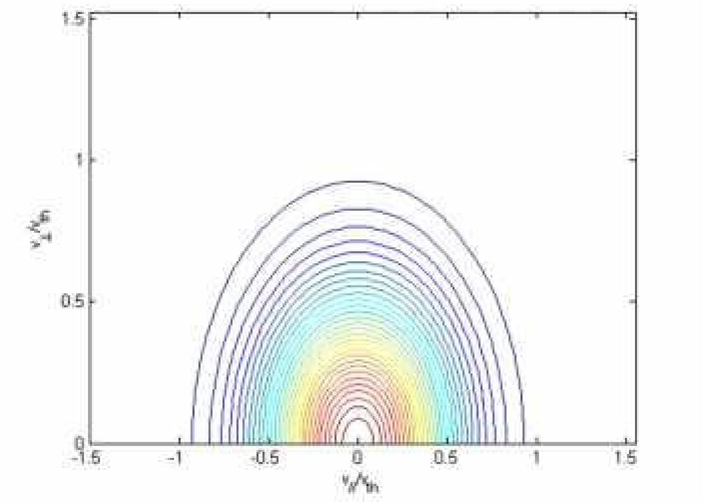

Figure 1: The initial distributions in phase space, v_{th} is thermal velocity

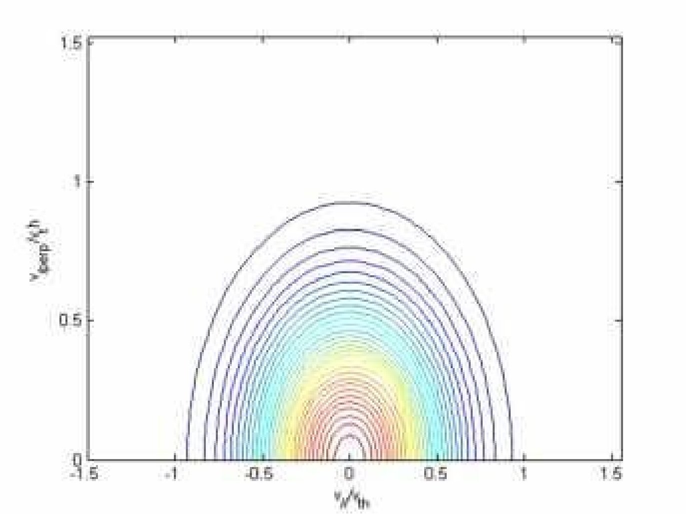

Figure 2: Distributions in phase space at t=5 ms

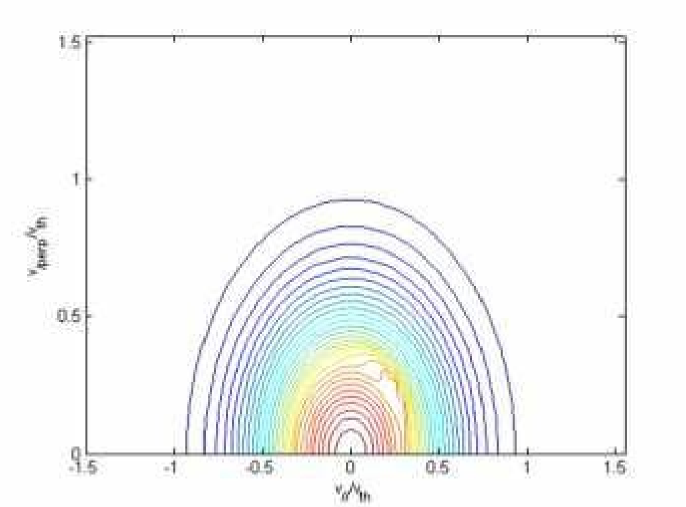

Figure 3: Distributions in phase space at t=10 ms

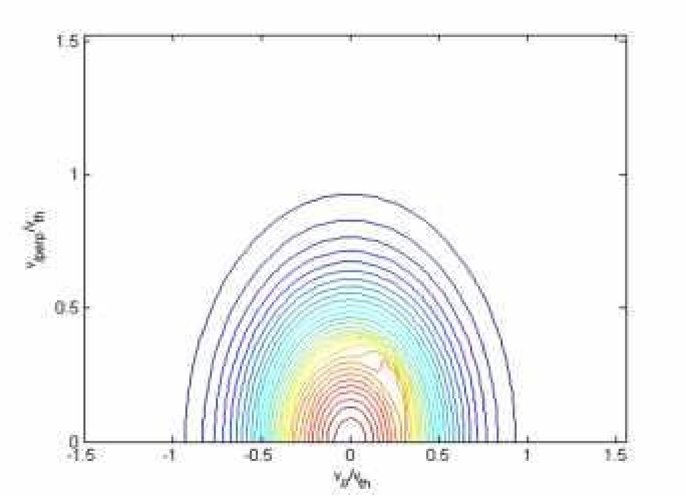

Figure 4: Distributions in phase space at t=20 ms

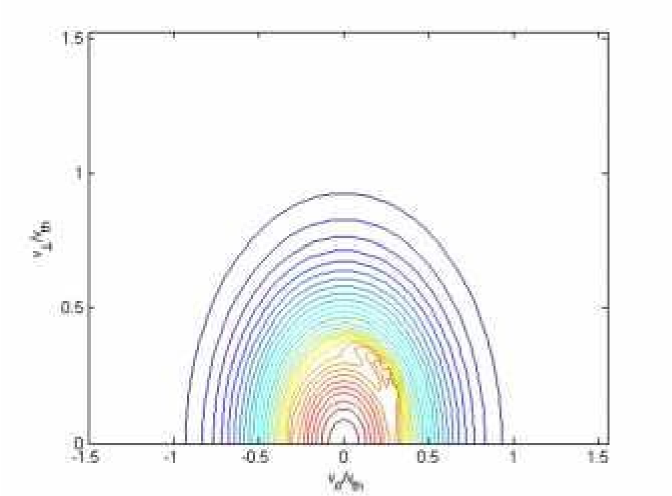

Figure 5: Distributions in phase space at t=40 ms

Via solving the equation (20), we can get the poloidal electric potential and rotation velocities in the conditions of different rf parameters.

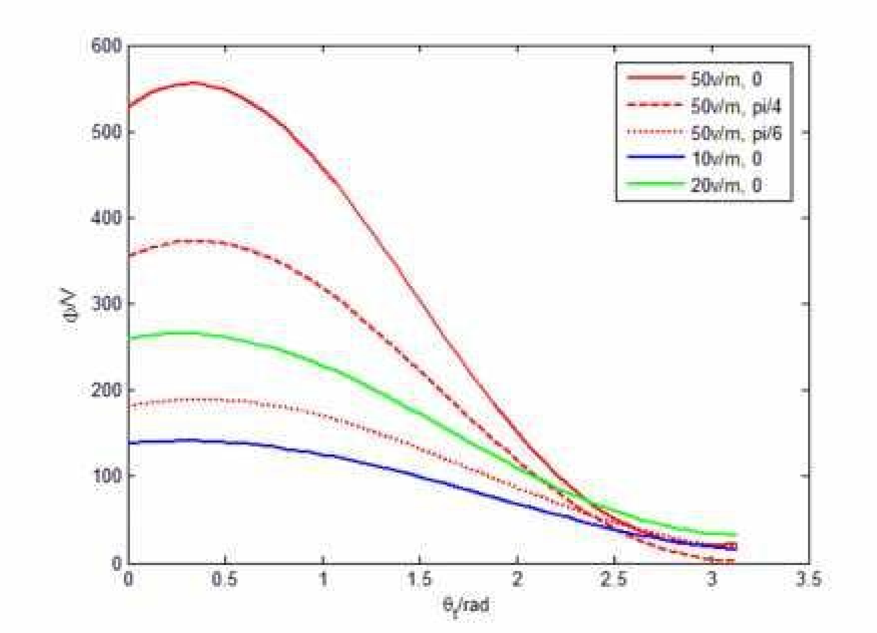

Figure 6: The poloidal electric potential in different rf power and injection angles.

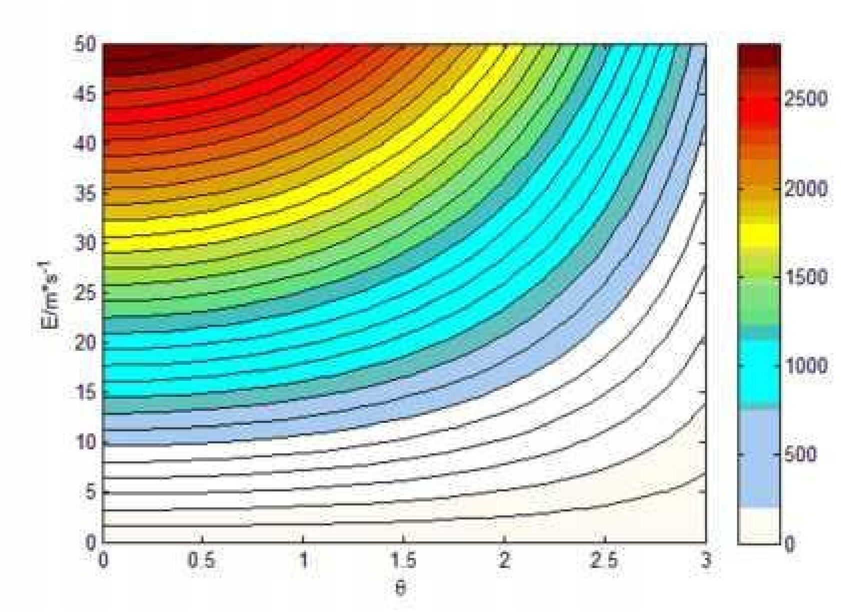

Figure 7: The rotation velocities' relation with rf power and injection angles. The white parts represent the conditions that ECRH cannot drive poloidal rotation

From figure 7, it is found that the higher rf power and smaller angle is need to get the high rotation velocity.

5. Summary

In conclusion, the contest between the ion accumulation rate and the magnetic pump damping results in plasma spin up. The study shows that the poloidal rotation of the ion species interacting with RF wave can be destabilized by the particle resonance localization during ECRH heating. When the disability condition is satisfied, the poloidal rotation speed will grow up exponentially. The rotation speed would be saturated in the level of the poloidal ion sound speed. This will produce an additional contribution to the plasma rotation. Also, the velocity of rotation is related to the rf parameters.

Reference：

1. N. Oyama et al., Nucl. Fusion 45, 871–881 (2005).
2. P. W. Xi, X. Q. Xu, X. G. Wang, and T. Y. Xia, Phys. Plasmas 19, 092503 (2012).
3. R. L. Miller, F. L. Waelbroeck, A. B. Hassam, and R. E. Waltz, Phys. Plasmas 2, 3676 (1995).
4. M. V. Medvedev and P. H. Diamond, Phys. Plasmas 2, 727 (1995).
5. K. H. Burrell., et al Rhodes, and D. M. Thomas, Phys. Plasmas 1, 1536 (1994).
6. W. M. Stacey, Jr., Phys. Fluids B 4, 3302 (1992).
7. F. L. Hinton, Phys. Fluids B 3, (1991).

8. A. B. Hassam, T. M. Antonson, Jr., J. F. Drake, and C. S. Liu, Phys. Rev. Lett. 66, 309 (1991).
9. C. G. Liu, M. Yamagiwa, and S. J. Qian, Physics of Plasmas 4, 2788 (1997).
10. J. Y. Hsu, V. S. Chan, R. W. Harvey, R. Prater, and S. K. Wong, Phys. Rev. Lett. 53, 564 (1984).
11. Wang Z T, Long Y X and Dong J Q, SRX Phys. 640826 (2010).
12. Maget P et al., Nucl. Fusion 46,979 (2006).

Bibliography

[1] Myla FJ Aronson, Frank A La Sorte, Charles H Nilon, Madhusudan Katti, Mark A Goddard, Christopher A Lepczyk, Paige S Warren, Nicholas SG Williams, Sarel Cilliers, Bruce Clarkson, et al. A global analysis of the impacts of urbanization on bird and plant diversity reveals key anthropogenic drivers. *Proc. R. Soc. B*, 281(1780):20133330, 2014.

[2] British Petroleum. Bp energy outlook 2035. *BP stats, Jan*, 2014.

[3] JPHE Ongena and G Van Oost. Energy for future centuries: prospects for fusion power as a future energy source. *Fusion science and technology*, 61(2T):3–16, 2012.

[4] Francis F Chen. *Introduction to plasma physics*. Springer Science & Business Media, 2012.

[5] D Reiter. Recycling and transport of neutrals. *Fusion Science and Technology*, 57(2T):303–312, 2010.

[6] Cornelis Marius Braams and Peter E Stott. *Nuclear fusion: half a century of magnetic confinement fusion research*. CRC Press, 2002.

[7] W Horton. Drift waves and transport. *Reviews of Modern Physics*, 71(3):735, 1999.

[8] Ulrich Samm. Controlled thermonuclear fusion at the beginning of a new era. *Contemporary Physics*, 44(3):203–217, 2003.

[9] Francis F Chen. Plasma ionization by helicon waves. *Plasma Physics and Controlled Fusion*, 33(4):339, 1991.

[10] John Wesson and David J Campbell. *Tokamaks*, volume 149. Oxford University Press, 2011.

[11] Asdex Team et al. The h-mode of asdex. *Nuclear Fusion*, 29(11):1959, 1989.

[12] ITER Physics Expert Group on Confinement and Transport. Chapter 2: Plasma confinement and transport. *Nucl. Fusion*, 39(12):2175, 1999.

[13] J Freidberg. Plasma physics and fusion energy cambridge university press. *New York*, 2007.

[14] F Wagner. The physics basis of iter confinement. In *AIP Conference Proceedings*, volume 1095, pages 31–53. AIP, 2009.

[15] Y Andrew, NC Hawkes, T Biewer, Kristel Crombe, D Keeling, E De La Luna, C Giroud, A Korotkov, A Meigs, A Murari, et al. Evolution of the radial electric field in a jet h-mode plasma. *EPL (Europhysics Letters)*, 83(1):15003, 2008.

[16] TN Carlstrom, KH Burrell, RJ Groebner, AW Leonard, TH Osborne, and DM Thomas. Comparison of lh transition measurements with physics models. *Nuclear Fusion*, 39(11Y):1941, 1999.

[17] JET Team et al. Overview of high performance h-modes in jet. *Plasma physics and controlled fusion*, 36(7A):A23, 1994.

[18] RJ Groebner, , et al. Overview of h-mode studies in diii-d. *Plasma physics and controlled fusion*, 36(7A):A13, 1994.

[19] PW Xi, XQ Xu, XG Wang, and TY Xia. Influence of equilibrium shear flow on peeling-ballooning instability and edge localized mode crash. *Physics of Plasmas*, 19(9):092503, 2012.

[20] Amanda E Hubbard. Physics and scaling of the h-mode pedestal. *Plasma Physics and Controlled Fusion*, 42(5A):A15, 2000.

[21] A Loarte, G Saibene, R Sartori, D Campbell, M Becoulet, L Horton, T Eich, A Herrmann, G Matthews, and N Asakura. Characteristics of type i elm energy and particle losses in existing devices and their extrapolation to iter. *Plasma Physics and Controlled Fusion*, 45(9):1549, 2003.

[22] A Kirk, IT Chapman, Yueqiang Liu, P Cahyna, P Denner, G Fishpool, CJ Ham, JR Harrison, Yunfeng Liang, E Nardon, et al. Understanding edge-localized mode mitigation by resonant magnetic perturbations on mast. *Nuclear Fusion*, 53(4):043007, 2013.

[23] Hartmut Zohm. Edge localized modes (elms). *Plasma Physics and Controlled Fusion*, 38(2):105, 1996.

[24] P Gohil, M Ali Mahdavi, L Lao, KH Burrell, MS Chu, JC DeBoo, CL Hsieh, N Ohyabu, RT Snider, RD Stambaugh, et al. Study of giant edge-localized modes in diii-d and comparison with ballooning theory. *Physical review letters*, 61(14):1603, 1988.

[25] GTA Huysmans. External kink (peeling) modes in x-point geometry. *Plasma physics and controlled fusion*, 47(12):2107, 2005.

[26] Shih-Tung Tsai and Liu Chen. Theory of kinetic ballooning modes excited by energetic particles in tokamaks. *Physics of Fluids B: Plasma Physics*, 5(9):3284–3290, 1993.

[27] Hartmut Zohm, F Wagner, M Endler, J Gernhardt, E Holzhauer, W Kerner, and V Mertens. Studies of edge localized modes on asdex. *Nuclear fusion*, 32(3):489, 1992.

[28] PB Snyder, HR Wilson, JR Ferron, LL Lao, AW Leonard, TH Osborne, AD Turnbull, D Mossessian, M Murakami, and XQ Xu. Edge localized modes and the pedestal: A model based on coupled peeling–ballooning modes. *Physics of Plasmas*, 9(5):2037–2043, 2002.

[29] AJ Webster and CG Gimblett. Magnetohydrodynamic stability at a separatrix. i. toroidal peeling modes and the energy principle. *Physics of Plasmas*, 16(8):082502, 2009.

[30] Valentin Igochine et al. *Active control of magneto-hydrodynamic instabilities in hot plasmas.* Springer, 2015.

[31] JW Connor, RJ Hastie, and JB Taylor. Stability of toroidal plasmas: the influence of magnetic shear, periodicity and rotation. *Plasma physics and controlled fusion*, 46(12B):B1, 2004.

[32] M Furukawa and S Tokuda. Stabilization mechanism of ballooning modes by toroidal rotation shear in tokamaks. *Nuclear fusion*, 45(5):377, 2005.

[33] Jayhyun Kim, Y-M Jeon, WW Xiao, S-W Yoon, J-K Park, GS Yun, J-W Ahn, HS Kim, H-L Yang, HK Kim, et al. Elm control experiments in the kstar device. *Nuclear Fusion*, 52(11):114011, 2012.

[34] N Oyama, Y Sakamoto, A Isayama, M Takechi, P Gohil, LL Lao, PB Snyder, T Fujita, S Ide, Y Kamada, et al. Energy loss for grassy elms and effects of plasma rotation on the elm characteristics in jt-60u. *Nuclear fusion*, 45(8):871, 2005.

[35] MR Wade, R Nazikian, JS Degrassie, TE Evans, NM Ferraro, RA Moyer, DM Orlov, RJ Buttery, ME Fenstermacher, AM Garofalo, et al. Advances in the physics understanding of elm suppression using resonant magnetic perturbations in diii-d. *Nuclear Fusion*, 55(2):023002.

[36] Todd E Evans, Richard A Moyer, Keith H Burrell, Max E Fenstermacher, Ilon Joseph, Anthony W Leonard, Thomas H Osborne, Gary D Porter, Michael J Schaffer, Philip B Snyder, et al. Edge stability and transport control with resonant magnetic perturbations in collisionless tokamak plasmas. *nature physics*, 2(6):419–423, 2006.

[37] Y Liang, HR Koslowski, PR Thomas, E Nardon, B Alper, P Andrew, Y Andrew, G Arnoux, Y Baranov, M Bécoulet, et al. Active control of type-i edge-localized modes with n= 1 perturbation fields in the jet tokamak. *Physical review letters*, 98(26):265004, 2007.

[38] Larry R Baylor, Stephen Kirk Combs, Charles R Foust, Thomas C Jernigan, SJ Meitner, PB Parks, John B Caughman, DT Fehling, S Maruyama, AL Qualls, et al. Pellet fuelling, elm pacing and disruption mitigation technology development for iter. *Nuclear Fusion*, 49(8):085013, 2009.

[39] PT Lang, B Alper, R Buttery, K Gal, J Hobirk, J Neuhauser, M Stamp, JET-EFDA contributors, et al. Elm triggering by local pellet perturbations in type-i elmy h-mode plasma at jet. *Nuclear Fusion*, 47(8):754, 2007.

[40] JX Rossel, J-M Moret, S Coda, O Sauter, TP Goodman, F Felici, D Testa, Y Martin, TCV Team, et al. Edge-localized mode control by electron cyclotron waves in a tokamak plasma. *Nuclear Fusion*, 52(3):032004, 2012.

[41] A Burckhart, M Dunne, E Wolfrum, R Fischer, R McDermott, E Viezzer, M Willensdorfer, et al. Elm behaviour and linear mhd stability of edge ecrh heated asdex upgrade plasmas. *Nuclear Fusion*, 56(5):056011, 2016.

[42] A Loarte, G Huijsmans, S Futatani, LR Baylor, TE Evans, DM Orlov, O Schmitz, M Becoulet, P Cahyna, Y Gribov, et al. Progress on the application of elm control schemes to iter scenarios from the non-active phase to dt operation. *Nuclear Fusion*, 54(3):033007, 2014.

[43] Brian A Grierson, Keith H Burrell, Raffi M Nazikian, Wayne M Solomon, Andrea M Garofalo, Emily A Belli, Gary M Staebler, Max E Fenstermacher, George R McKee, Todd E Evans, et al. Impurity confinement and transport in high confinement regimes without edge localized modes on diii-d. *Physics of Plasmas*, 22(5):055901, 2015.

[44] DG Whyte, AE Hubbard, JW Hughes, B Lipschultz, JE Rice, ES Marmar, M Greenwald, I Cziegler, A Dominguez, T Golfinopoulos, et al. I-mode: an h-mode energy confinement regime with l-mode particle transport in alcator c-mod. *Nuclear Fusion*, 50(10):105005, 2010.

[45] WM Solomon, KH Burrell, ME Fenstermacher, AM Garofalo, BA Grierson, A Loarte, GR McKee, R Nazikian, TH Osborne, and PB Snyder. Extending the physics basis of quiescent h-mode toward iter relevant parameters. *Nuclear Fusion*, 55(7):073031, 2015.

[46] M Murakami, GR McKee, GL Jackson, GM Staebler, DR Baker, A Boedo, NH Brooks, KH Burrell, D Ernst, TE Evans, et al. Transport studies of lmode edge radiating mantle discharges with confinement improvement in diiid. *Bull. Am. Phys. Soc*, 44:127, 1999.

[47] W Suttrop, GD Conway, L Fattorini, LD Horton, T Kurki-Suonio, CF Maggi, M Maraschek, H Meister, R Neu, Th Pütterich, et al. Study of quiescent h-mode plasmas in asdex upgrade. *Plasma physics and controlled fusion*, 46(5A):A151, 2004.

[48] Y Sakamoto, H Shirai, T Fujita, S Ide, T Takizuka, N Oyama, and Y Kamada. Impact of toroidal rotation on elm behaviour in the h-mode on jt-60u. *Plasma physics and controlled fusion*, 46(5A):A299, 2004.

[49] W Suttrop, V Hynönen, T Kurki-Suonio, PT Lang, M Maraschek, R Neu, A Stäbler, GD Conway, S Hacquin, M Kempenaars, et al. Studies of the quiescent h-moderegime in asdex upgrade and jet. *Nuclear fusion*, 45(7):721, 2005.

[50] WP West, CJ Lasnier, TA Casper, TH Osborne, KH Burrell, PB Snyder, DM Thomas, EJ Doyle, and AW Leonard. Pedestal profiles during qh-mode operation on diii-d. *Plasma physics and controlled fusion*, 46(5A):A179, 2004.

[51] KH Burrell, ME Austin, DP Brennan, JC DeBoo, EJ Doyle, C Fenzi, C Fuchs, P Gohil, CM Greenfield, RJ Groebner, et al. Quiescent double barrier high-confinement mode plasmas in the diii-d tokamak. *Physics of Plasmas*, 8(5):2153–2162, 2001.

[52] KH Burrell, WP West, EJ Doyle, ME Austin, TA Casper, P Gohil, CM Greenfield, RJ Groebner, AW Hyatt, RJ Jayakumar, et al. Advances in understanding quiescent h-mode plasmas in diii-d. *Physics of plasmas*, 12(5):056121, 2005.

[53] AM Garofalo, KH Burrell, JC DeBoo, GL Jackson, M Lanctot, H Reimerdes, MJ Schaffer, WM Solomon, EJ Strait, et al. Observation of plasma rotation driven by static nonaxisymmetric magnetic fields in a tokamak. *Physical review letters*, 101(19):195005, 2008.

[54] KH Burrell, AM Garofalo, WM Solomon, ME Fenstermacher, DM Orlov, TH Osborne, J-K Park, and PB Snyder. Quiescent h-mode operation using torque from non-axisymmetric, non-resonant magnetic fields. *Nuclear Fusion*, 53(7):073038, 2013.

[55] PB Snyder, KH Burrell, HR Wilson, MS Chu, ME Fenstermacher, AW Leonard, RA Moyer, TH Osborne, M Umansky, WP West, et al. Stability and dynamics of the edge pedestal in the low collisionality regime: physics mechanisms for steady-state elm-free operation. *Nuclear Fusion*, 47(8):961, 2007.

[56] Xi Chen, Keith H Burrell, Nathaniel M Ferraro, Thomas H Osborne, Max E Austin, Andrea M Garofalo, Richard J Groebner, Gerrit J Kramer, Neville C Luhmann Jr, George R McKee, et al. Rotational shear effects on edge harmonic oscillations in diii-d quiescent h-mode discharges. *Nuclear Fusion*, 56(7):076011, 2016.

[57] JG Chen, XQ Xu, CH Ma, PW Xi, DF Kong, and YA Lei. Impact of e× b shear flow on low-n mhd instabilities. *Physics of plasmas*, 24(5):050704, 2017.

[58] Ulrich R Christensen. Zonal flow driven by deep convection in the major planets. *Geophysical research letters*, 28(13):2553–2556, 2001.

[59] Akira Hasegawa, Carol G Maclennan, and Yuji Kodama. Nonlinear behavior and turbulence spectra of drift waves and rossby waves. *The Physics of Fluids*, 22(11):2122–2129, 1979.

[60] A Fujisawa, K Itoh, H Iguchi, K Matsuoka, S Okamura, A Shimizu, T Minami, Y Yoshimura, K Nagaoka, C Takahashi, et al. Identification of zonal flows in a toroidal plasma. *Physical review letters*, 93(16):165002, 2004.

[61] Zhihong Lin, Taik Soo Hahm, WW Lee, William M Tang, and Roscoe B White. Turbulent transport reduction by zonal flows: Massively parallel simulations. *Science*, 281(5384):1835–1837, 1998.

[62] Patrick H Diamond, SI Itoh, K Itoh, and TS Hahm. Zonal flows in plasmaa review. *Plasma Physics and Controlled Fusion*, 47(5):R35, 2005.

[63] Zhihong Lin, TS Hahm, WW Lee, WM Tang, and PH Diamond. Effects of collisional zonal flow damping on turbulent transport. *Physical review letters*, 83(18):3645, 1999.

[64] Liu Chen, Zhihong Lin, and Roscoe White. Excitation of zonal flow by drift waves in toroidal plasmas. *Physics of Plasmas*, 7(8):3129–3132, 2000.

[65] AI Smolyakov, PH Diamond, and VI Shevchenko. Zonal flow generation by parametric instability in magnetized plasmas and geostrophic fluids. *Physics of Plasmas*, 7(5):1349–1351, 2000.

[66] Niels Winsor, John L Johnson, and John M Dawson. Geodesic acoustic waves in hydromagnetic systems. *The Physics of Fluids*, 11(11):2448–2450, 1968.

[67] HYW Tsui, K Rypdal, Ch P Ritz, and AJ Wootton. Coherent nonlinear coupling between a long-wavelength mode and small-scale turbulence in the text tokamak. *Physical review letters*, 70(17):2565, 1993.

[68] GD Conway, B Scott, J Schirmer, M Reich, A Kendl, et al. Direct measurement of zonal flows and geodesic acoustic mode oscillations in asdex upgrade using doppler reflectometry. *Plasma Physics and Controlled Fusion*, 47(8):1165, 2005.

[69] Y Hamada, A Nishizawa, T Ido, T Watari, M Kojima, Y Kawasumi, K Narihara, K Toi, et al. Zonal flows in the geodesic acoustic mode frequency range in the jipp t-iiu tokamak plasmas. *Nuclear Fusion*, 45(2):81, 2005.

[70] Zhe Gao. Collisional damping of the geodesic acoustic mode. *Physics of Plasmas*, 20(3):032501, 2013.

[71] Yang Li and Zhe Gao. Comparison of collision operators for the geodesic acoustic mode. *Nuclear Fusion*, 55(4):043001, 2015.

[72] AG Peeters, D Strintzi, Y Camenen, C Angioni, FJ Casson, WA Hornsby, and AP Snodin. Influence of the centrifugal force and parallel dynamics on the toroidal momentum transport due to small scale turbulence in a tokamak. *Physics of Plasmas*, 16(4):042310, 2009.

[73] UR Christensen. Zonal flow driven by strongly supercritical convection in rotating spherical shells. *Journal of Fluid Mechanics*, 470:115–133, 2002.

[74] T Gastine, J Wicht, and JM Aurnou. Zonal flow regimes in rotating anelastic spherical shells: An application to giant planets. *Icarus*, 225(1):156–172, 2013.

[75] BD Dudson, MV Umansky, XQ Xu, PB Snyder, and HR Wilson. Bout++: A framework for parallel plasma fluid simulations. *Computer Physics Communications*, 180(9):1467–1480, 2009.

[76] Andrew R Allen. *Plasma Response to Magnetic Perturbations Relevant to Edge Localised Modes.* PhD thesis, University of York, 2013.

[77] P Ricci, FD Halpern, S Jolliet, J Loizu, A Mosetto, A Fasoli, I Furno, and C Theiler. Simulation of plasma turbulence in scrape-off layer conditions: the gbs code, simulation results and code validation. *Plasma Physics and Controlled Fusion*, 54(12):124047, 2012.

[78] William D D'haeseleer, William NG Hitchon, James D Callen, and J Leon Shohet. *Flux coordinates and magnetic field structure: a guide to a fundamental tool of plasma theory.* Springer Science & Business Media, 2012.

[79] Peter Hill, Brendan Shanahan, and Ben Dudson. Dirichlet boundary conditions for arbitrary-shaped boundaries in stellarator-like magnetic fields for the flux-coordinate independent method. *Computer Physics Communications*, 213:9–18, 2017.

[80] Brendan Shanahan, Peter Hill, and Ben Dudson. Towards nonaxisymmetry; initial results using the flux coordinate independent method in bout++. *arXiv preprint arXiv:1609.06603*, 2016.

[81] LL Lao, SP Hirshman, and RM Wieland. Variational moment solutions to the grad–shafranov equation. *The Physics of Fluids*, 24(8):1431–1440, 1981.

[82] Michael Barnes. Trinity: A unified treatment of turbulence, transport, and heating in magnetized plasmas.

[83] James A Crotinger, L LoDestro, L Don Pearlstein, A Tarditi, TA Casper, and E Bickford Hooper. Corsica: A comprehensive simulation of toroidal magnetic-fusion devices. final report to the ldrd program. Technical report, Lawrence Livermore National Lab., CA (United States), 1997.

[84] Benjamin Daniel Dudson and Jarrod Leddy. Hermes: global plasma edge fluid turbulence simulations. *Plasma Physics and Controlled Fusion*, 59(5):054010, 2017.

[85] Andrei N Simakov and Peter J Catto. Drift-ordered fluid equations for field-aligned modes in low-β collisional plasma with equilibrium pressure pedestals. *Physics of Plasmas*, 10(12):4744–4757, 2003.

[86] Fabio Riva, Fulvio Militello, Sarah Elmore, John T Omotani, Ben Dudson, Nick R Walkden, et al. Three-dimensional plasma edge turbulence simulations of the mega ampere spherical tokamak and comparison with experimental measurements. *Plasma Physics and Controlled Fusion*, 61(9):095013, 2019.

[87] L Easy, F Militello, J Omotani, B Dudson, E Havlíčková, P Tamain, Volker Naulin, and Anders Henry Nielsen. Three dimensional simulations of plasma filaments in the scrape off layer: A comparison with models of reduced dimensionality. *Physics of Plasmas*, 21(12):122515, 2014.

[88] OE Garcia, V Naulin, AH Nielsen, and J Juul Rasmussen. Turbulence and intermittent transport at the boundary of magnetized plasmas. *Physics of plasmas*, 12(6):062309, 2005.

[89] Richard D Hazeltine and James D Meiss. *Plasma confinement*. Courier Corporation, 2003.

[90] B Dudson. Bout++ users manual, 2007.

[91] JW Connor, RJ Hastie, HR Wilson, and RL Miller. Magnetohydrodynamic stability of tokamak edge plasmas. *Physics of Plasmas*, 5(7):2687–2700, 1998.

[92] ZT Wang, ZX He, JQ Dong, ZH Wang, M Xu, XL Xu, ML Mou, TT Sun, J Huang, and SY Chen. Kink modes in pedestal. *Physics of Plasmas*, 21(3):032505, 2014.

[93] JW Connor, RJ Hastie, and JB Taylor. Shear, periodicity, and plasma ballooning modes. *Physical Review Letters*, 40(6):396, 1978.

[94] Janardhan Manickam. The role of edge current density on kink mode stability and its implication for magnetohydrodynamic activity associated with edge localized modes. *Physics of Fluids B: Plasma Physics*, 4(7):1901–1908, 1992.

[95] TH Osborne, PB Snyder, KH Burrell, TE Evans, ME Fenstermacher, AW Leonard, RA Moyer, MJ Schaffer, and WP West. Edge stability of stationary elm-suppressed regimes on diii-d. In *Journal of Physics: Conference Series*, volume 123, page 012014. IOP Publishing, 2008.

[96] TJ Boyd, TJM Boyd, and JJ Sanderson. *The physics of plasmas*. Cambridge University Press, 2003.

[97] JW Connor, CJ Ham, and RJ Hastie. The effect of plasma beta on high-n ballooning stability at low magnetic shear. *Plasma Physics and Controlled Fusion*, 58(8):085002, 2016.

[98] KHAN Riaz et al. Simulation study on nonlinear dynamics of ballooning modes in a spherical tokamak. 2006.

[99] RL Miller, YR Lin-Liu, TH Osborne, and TS Taylor. Ballooning mode stability for self-consistent pressure and current profiles at the h-mode edge. *Plasma physics and controlled fusion*, 40(5):753, 1998.

[100] P áB Snyder, TH Osborne, KH Burrell, RJ Groebner, AW Leonard, R Nazikian, DM Orlov, O Schmitz, MR Wade, and HR Wilson. The eped

pedestal model and edge localized mode-suppressed regimes: Studies of quiescent h-mode and development of a model for edge localized mode suppression via resonant magnetic perturbations. *Physics of plasmas*, 19(5):056115, 2012.

[101] JW Hughes, PB Snyder, ML Reinke, B LaBombard, S Mordijck, S Scott, E Tolman, SG Baek, T Golfinopoulos, RS Granetz, et al. Access to pedestal pressure relevant to burning plasmas on the high magnetic field tokamak alcator c-mod. *Nuclear Fusion*, 58(11):112003, 2018.

[102] PB Snyder, RJ Groebner, JW Hughes, TH Osborne, M Beurskens, AW Leonard, HR Wilson, and XQ Xu. A first-principles predictive model of the pedestal height and width: development, testing and iter optimization with the eped model. *Nuclear Fusion*, 51(10):103016, 2011.

[103] PB Snyder, JW Hughes, TH Osborne, C Paz-Soldan, WM Solomon, M Knolker, D Eldon, T Evans, T Golfinopoulos, BA Grierson, et al. High fusion performance in super h-mode experiments on alcator c-mod and diii-d. *Nuclear Fusion*, 59(8):086017, 2019.

[104] HAB Bodin and AA Newton. Reversed-field-pinch research. *Nuclear fusion*, 20(10):1255, 1980.

[105] Martin David Kruskal and Martin Schwarzschild. Some instabilities of a completely ionized plasma. *Proc. R. Soc. Lond. A*, 223(1154):348–360, 1954.

[106] Vitaly D Shafranov. Hydromagnetic stability of a current-carrying pinch in a strong longitudinal magnetic field. *Soviet Physics Technical Physics*, 15:175, 1970.

[107] Marshall N Rosenbluth, RY Dagazian, and PH Rutherford. Nonlinear properties of the internal m= 1 kink instability in the cylindrical tokamak. *The Physics of Fluids*, 16(11):1894–1902, 1973.

[108] D Edery, G Laval, R Pellat, and JL Soulé. Current-driven internal kink modes in cylindrical and helicoidal discharges. *The Physics of Fluids*, 19(2):260–265, 1976.

[109] MN Bussac, R Pellat, D Edery, and JL Soule. Internal kink modes in toroidal plasmas with circular cross sections. *Physical Review Letters*, 35(24):1638, 1975.

[110] RJ Hastie, TC Hender, BA Carreras, LA Charlton, and JA Holmes. Stability of ideal and resistive internal kink modes in toroidal geometry. *The Physics of fluids*, 30(6):1756–1766, 1987.

[111] B Coppi, R Galvao, R Pellat, M Rosenbluth, and P Rutherford. Resistive internal kink modes. *Fizika Plazmy*, 2:961–966, 1976.

[112] EA Frieman, JM Greene, JL Johnson, and KE Weimer. Toroidal effects on magnetohydrodynamic modes in tokamaks. *The Physics of Fluids*, 16(7):1108–1125, 1973.

[113] CG Gimblett. On free boundary instabilities induced by a resistive wall. *Nuclear fusion*, 26(5):617, 1986.

[114] F Troyon, R Gruber, H Saurenmann, S Semenzato, and S Succi. Mhd-limits to plasma confinement. *Plasma physics and controlled fusion*, 26(1A):209, 1984.

[115] S Ishida, Y Koide, T Ozeki, M Kikuchi, S Tsuji, H Shirai, O Naito, and M Azumi. Observation of a fast beta collapse during high poloidal-beta discharges in jt-60. *Physical review letters*, 68(10):1531, 1992.

[116] M Gryaznevich, R Akers, PG Carolan, NJ Conway, D Gates, AR Field, TC Hender, I Jenkins, R Martin, MPS Nightingale, et al. Achievement of record β in the start spherical tokamak. *Physical review letters*, 80(18):3972, 1998.

[117] Anthony J Webster. Techniques for studying the separatrix of tokamak plasmas. *Physics of Plasmas*, 16(1):012501, 2009.

[118] Davide Galassi, Guido Ciraolo, Patrick Tamain, Hugo Bufferand, Philippe Ghendrih, Nicolas Nace, and Eric Serre. Tokamak edge plasma turbulence interaction with magnetic x-point in 3d global simulations. *Fluids*, 4(1):50, 2019.

[119] S Saarelma, OJ Kwon, A Kirk, MAST Team, et al. X-point effect on edge stability. *Plasma Physics and Controlled Fusion*, 53(2):025011, 2011.

[120] Robert J Goldston and Paul Harding Rutherford. *Introduction to plasma physics*. CRC Press, 1995.

[121] SI Braginskii and MA Leontovich. Reviews of plasma physics, 1965.

[122] GQ Li, ZX Liu, XQ Xu, TY Xia, X Gao, PB Snyder, SY Ding, JG Li, SC Liu, and CH Ma. Studies of impact of edge current profiles, plasma shaping, nonlinearity on edge localized modes with bout++ code.

[123] Y Luo, SY Chen, J Huang, YY Xiong, and CJ Tang. Influence of equilibrium shear flow in the parallel magnetic direction on edge localized mode crash. *Physics of Plasmas*, 23(4):042302, 2016.

[124] BD Dudson, XQ Xu, MV Umansky, HR Wilson, and PB Snyder. Simulation of edge localized modes using bout++. *Plasma Physics and Controlled Fusion*, 53(5):054005, 2011.

[125] Robert Hager and Klaus Hallatschek. Radial propagation of geodesic acoustic modes. *Physics of Plasmas*, 16(7):072503, 2009.

[126] B Shanahan, B Dudson, and P Hill. Fluid simulations of plasma filaments in stellarator geometries with bsting. *Plasma Physics and Controlled Fusion*, 61(2):025007, 2018.

[127] MJ May, M Finkenthal, HW Moos, KB Fournier, WH Goldstein, M Mattioli, D Pacella, G Mazzitelli, M Leigheb, and L Gabellieri. Improved confinement regime in the current ramp down phase of frascati tokamak upgrade plasmas. *Nuclear fusion*, 42(11):1299, 2002.

[128] F Imbeaux, J Citrin, J Hobirk, GMD Hogeweij, F Köchl, VM Leonov, S Miyamoto, Y Nakamura, V Parail, G Pereverzev, et al. Current ramps in tokamaks: from present experiments to iter scenarios. *Nuclear Fusion*, 51(8):083026, 2011.

[129] CG Liu, M Yamagiwa, and SJ Qian. Production of sheared flow during ion cyclotron resonance heating in tokamak plasmas. *Physics of Plasmas*, 4(8):2788–2790, 1997.

[130] Shaojie Wang. Zonal flows in tokamak plasmas with toroidal rotation. *Physical review letters*, 97(8):085002, 2006.

[131] A Thyagaraja and KG McClements. Plasma physics in noninertial frames. *Physics of Plasmas*, 16(9):092506, 2009.

[132] Chengkang Pan, Shaojie Wang, Xiaotao Xiao, Lei Ye, Yingfeng Xu, and Zongliang Dai. In-out impurity density asymmetry due to the coriolis force in a rotating tokamak plasma. *arXiv preprint arXiv:1801.08298*, 2018.

[133] Maarten De Bock. Understanding and controlling plasma rotation in tokamaks, 2007.

[134] M Kobayashi, T Tuda, K Tashiro, H Kojima, Kan Zhai, and S Takamura. Interaction of externally applied rotating helical field with tokamak plasma. *Nuclear fusion*, 40(2):181, 2000.

[135] LG Eriksson, T Hellsten, MFF Nave, J Brzozowski, Kerstin Holmström, Thomas Johnson, J Ongena, KD Zastrow, JET-EFDA Contributors, et al. Toroidal rotation in rf heated jet plasmas. *Plasma Physics and Controlled Fusion*, 51(4):044008, 2009.

[136] JE Rice, A Ince-Cushman, L-G Eriksson, Y Sakamoto, A Scarabosio, A Bortolon, KH Burrell, BP Duval, C Fenzi-Bonizec, MJ Greenwald, et al. Intermachine comparison of intrinsic toroidal rotation in tokamaks. *Nuclear Fusion*, 47(11):1618, 2007.

[137] RM McDermott, C Angioni, R Dux, A Gude, T Pütterich, F Ryter, G Tardini, et al. Effect of electron cyclotron resonance heating (ecrh) on toroidal rotation in asdex upgrade h-mode discharges. *Plasma Physics and Controlled Fusion*, 53(3):035007, 2011.

[138] B LaBombard, JE Rice, AE Hubbard, JW Hughes, M Greenwald, J Irby, Y Lin, B Lipschultz, ES Marmar, CS Pitcher, et al. Transport-driven scrape-off-layer flows and the boundary conditions imposed at the magnetic separatrix in a tokamak plasma. *Nuclear fusion*, 44(10):1047, 2004.

[139] AB Hassam, TM Antonsen Jr, JF Drake, and CS Liu. Spontaneous poloidal spin-up of tokamaks and the transition to the h mode. *Physical review letters*, 66(3):309, 1991.

[140] JY Hsu, VS Chan, RW Harvey, R Prater, and SK Wong. Resonance localization and poloidal electric field due to cyclotron wave heating in tokamak plasmas. *Physical review letters*, 53(6):564, 1984.

[141] R HOLTON James and RH Thomas. An introduction to dynamic meteorology, 2004.

[142] FL Hinton and SK Wong. Neoclassical ion transport in rotating axisymmetric plasmas. *The Physics of fluids*, 28(10):3082–3098, 1985.

[143] JA Wesson. Poloidal distribution of impurities in a rotating tokamak plasma. *Nuclear fusion*, 37(5):577, 1997.

[144] P Smeulders. Tomography of quasi-static deformations of constant-emission surfaces of high-beta plasmas in asdex. *Nuclear fusion*, 26(3):267, 1986.

[145] R Dux, A Gude Peeters, A Gude, A Kallenbach, R Neu, and ASDEX Upgrade Team. Z dependence of the core impurity transport in asdex upgrade h mode discharges. *Nuclear Fusion*, 39(11):1509, 1999.

[146] AG Peeters, C Angioni, and D Strintzi. Toroidal momentum pinch velocity due to the coriolis drift effect on small scale instabilities in a toroidal plasma. *Physical Review Letters*, 98(26):265003, 2007.

[147] Y Camenen, AG Peeters, C Angioni, Francis James Casson, WA Hornsby, AP Snodin, and D Strintzi. Transport of parallel momentum induced by current-symmetry breaking in toroidal plasmas. *Physical review letters*, 102(12):125001, 2009.

[148] A Krämer-Flecken, S Soldatov, HR Koslowski, O Zimmermann, TEXTOR team, et al. Properties of geodesic acoustic modes and the relation to density fluctuations. *Physical review letters*, 97(4):045006, 2006.

[149] GR McKee, P Gohil, DJ Schlossberg, JA Boedo, KH Burrell, RJ Groebner, RA Moyer, CC Petty, TL Rhodes, L Schmitz, et al. Dependence of the l-to h-mode power threshold on toroidal rotation and the link to edge turbulence dynamics. *Nuclear Fusion*, 49(11):115016, 2009.

[150] Akira Hasegawa and Masahiro Wakatani. Plasma edge turbulence. *Physical Review Letters*, 50(9):682, 1983.

[151] JM Dewhurst, B Hnat, and RO Dendy. Finite larmor radius effects on test particle transport in drift wave-zonal flow turbulence. *Plasma Physics and Controlled Fusion*, 52(2):025004, 2010.

[152] EJ Strait, AM Garofalo, GL Jackson, M Okabayashi, H Reimerdes, MS Chu, R Fitzpatrick, RJ Groebner, Y In, RJ LaHaye, et al. Resistive wall mode stabilization by slow plasma rotation in diii-d tokamak discharges with balanced neutral beam injection. *Physics of plasmas*, 14(5):056101, 2007.

[153] MS Chu, JM Greene, TH Jensen, RL Miller, A Bondeson, RW Johnson, and ME Mauel. Effect of toroidal plasma flow and flow shear on global magnetohydrodynamic mhd modes. *Physics of Plasmas*, 2(6):2236–2241, 1995.

[154] Nikolai N Gorelenkov and Leonid E Zakharov. Plasma equilibrium with fast ion orbit width, pressure anisotropy, and toroidal flow effects. *Nuclear Fusion*, 2018.

[155] Y Sakamoto, Y Kamada, S Ide, T Fujita, H Shirai, T Takizuka, Y Koide, T Fukuda, T Oikawa, T Suzuki, et al. Characteristics of internal transport barriers in jt-60u reversed shear plasmas. *Nuclear fusion*, 41(7):865, 2001.

[156] AV Melnikov, LG Eliseev, SV Perfilov, SE Lysenko, RV Shurygin, VN Zenin, SA Grashin, LI Krupnik, AS Kozachek, R Yu Solomatin, et al. The features of the global gam in oh and ecrh plasmas in the t-10 tokamak. *Nuclear Fusion*, 55(6):063001, 2015.

[157] Jun Yu, Xueyu Gong, and You Chen. Low frequency zonal flow excitation by drift waves in tokamak plasmas with toroidal rotation. *Nuclear Fusion*, 55(2):023015, 2015.

[158] Chandru Iyer and GM Prabhu. Lorentz transformations with arbitrary line of motion. *European journal of physics*, 28(2):183, 2007.

[159] Bernd Flemisch, Stefan Kurz, and Barbara Wohlmuth. A framework for maxwells equations in non-inertial frames based on differential forms. 2006.

[160] Robert A Nelson. Generalized lorentz transformation for an accelerated, rotating frame of reference. *Journal of mathematical physics*, 28(10):2379–2383, 1987.

[161] Peter J Catto and Andrei N Simakov. A drift ordered short mean free path description for magnetized plasma allowing strong spatial anisotropy. *Physics of Plasmas*, 11(1):90–102, 2004.

[162] AN Simakov and PJ Catto. Drift-ordered fluid equations for modelling collisional edge plasma. *Contributions to Plasma Physics*, 44(1-3):83–94, 2004.

[163] SG Tagare. Effect of ion temperature on propagation of ion-acoustic solitary waves of small amplitudes in collisionless plasma. *Plasma Physics*, 15(12):1247, 1973.

[164] DK Gartling and CE Hickox. A numerical study of the applicability of the boussinesq approximation for a fluid-saturated porous medium. *International Journal for Numerical Methods in Fluids*, 5(11):995–1013, 1985.

[165] P Martin. New system of coordinates for tokamaks. *Astrophysics and space science*, 256(1-2):411–416, 1997.

[166] Francis James Casson, AG Peeters, C Angioni, Y Camenen, WA Hornsby, AP Snodin, and G Szepesi. Gyrokinetic simulations including the centrifugal force in a rotating tokamak plasma. *Physics of Plasmas*, 17(10):102305, 2010.

[167] Qing Zhou, Xinliang Xu, Jie Wen, Lin Nie, Changjian Tang, and Yubin Gong. Poloidal rotation driven by electron cyclotron resonance wave in tokamak plasmas. *AIP Advances*, 7(10):105021, 2017.

[168] L Nie, M Xu, R Ke, BD Yuan, YF Wu, J Cheng, T Lan, Y Yu, RJ Hong, D Guo, et al. Experimental evaluation of langmuir probe sheath potential coefficient on the hl-2a tokamak. *Nuclear Fusion*, 58(3):036021, 2018.

[169] KJ Zhao, JQ Dong, LW Yan, WY Hong, A Fujisawa, CX Yu, Q Li, J Qian, J Cheng, T Lan, et al. Turbulence and zonal flows in edge plasmas of the hl-2a tokamak. *Plasma Physics and Controlled Fusion*, 52(12):124008, 2010.

[170] KN Geng, DF Kong, AD Liu, T Lan, CX Yu, HL Zhao, LW Yan, J Cheng, KJ Zhao, JQ Dong, et al. The role of geodesic acoustic mode on reducing the turbulent transport in the edge plasma of tokamak. *Physics of Plasmas*, 25(1):012317, 2018.

[171] XR Duan, XT Ding, JQ Dong, LW Yan, Yi Liu, Y Huang, XM Song, XL Zou, M Xu, QW Yang, et al. An overview of recent hl-2a experiments. *Nuclear Fusion*, 53(10):104009, 2013.

[172] P Angelino, A Bottino, R Hatzky, S Jolliet, O Sauter, TM Tran, and L Villard. Effects of plasma current on nonlinear interactions of itg turbulence, zonal flows and geodesic acoustic modes. *Plasma physics and controlled fusion*, 48(5):557, 2006.

[173] IH Hutchinson, JE Rice, RS Granetz, and JA Snipes. Self-acceleration of a tokamak plasma during ohmic h mode. *Physical review letters*, 84(15):3330, 2000.

[174] JW Connor and HR Wilson. A review of theories of the lh transition. *Plasma Physics and Controlled Fusion*, 42(1):R1, 2000.

[175] FL Waelbroeck and Liu Chen. Ballooning instabilities in tokamaks with sheared toroidal flows. *Physics of Fluids B: Plasma Physics*, 3(3):601–610, 1991.

[176] MV Medvedev and PH Diamond. Theory of ideal magnetohydrodynamic ballooning stability of a poloidally rotating plasma in a sheared electric field. *Physics of Plasmas*, 2(3):727–732, 1995.

[177] Benjamin Daniel Dudson, A Allen, George Breyiannis, Eric Brugger, James Buchanan, Luke Easy, Sean Farley, Ilon Joseph, Minwoo Kim, AD McGann, et al. Bout++: Recent and current developments. *Journal of Plasma Physics*, 81(1), 2015.

[178] XQ Xu, B Dudson, PB Snyder, MV Umansky, and H Wilson. Nonlinear simulations of peeling-ballooning modes with anomalous electron viscosity and their role in edge localized mode crashes. *Physical review letters*, 105(17):175005, 2010.

[179] D Dickinson, CM Roach, JM Skipp, and HR Wilson. Structure of micro-instabilities in tokamak plasmas: Stiff transport or plasma eruptions? *Physics of Plasmas*, 21(1):010702, 2014.

[180] PA Abdoul, David Dickinson, CM Roach, and Howard Read Wilson. Generalised ballooning theory of two-dimensional tokamak modes. *Plasma Physics and Controlled Fusion*, 60(2):025011, 2017.

[181] KH Burrell, TH Osborne, PB Snyder, WP West, ME Fenstermacher, RJ Groebner, P Gohil, AW Leonard, and WM Solomon. Quiescent h-mode plasmas with strong edge rotation in the cocurrent direction. *Physical review letters*, 102(15):155003, 2009.